Mechanics of the solid-state bonding under severe thermomechanical processes

A Dissertation Presented for the

Doctor of Philosophy

Degree

University of Tennessee, Knoxville

Xue Wang

December 2020

Copyright © 2020 by Xue Wang

All rights reserved.

Dedication

This dissertation is dedicated to my parents for their sincere love and support.

Acknowledgements

I would like to present my sincere gratitude to all those people who helped and supported me through my Ph.D study, this dissertation would not been done without them. My greatest appreciation goes first to my advisor, Dr. Yanfei Gao for his continuous academically support of my Ph.D study as well as for his guidance on my professional career development. It is an honor for me to work with him, who is knowledgeable and professional, and always providing thought-provoking discussions and suggestions to my research. I would also like to express my gratitude to my co-advisor Dr. Zhili Feng for the project support of the dissertation work and his inspiring guidance on my research. He provided me with many valuable opportunities and advices which help me in my career development.

I would like to thank my committee members, Dr. Peter K. Liaw and Dr. Claudia J. Rawn, for their kind agreement to be on my Doctoral Committee, and their insightful comments and guidance for my dissertation work from different scientific viewpoints. Their outstanding knowledge and great scientific enthusiasm impressed me and guided me in pursuing a successful academic career.

These acknowledgements would not be complete without mentioning my group members and friends who have constantly helped me and shared happiness together. They are Dr. Wei Zhang, Dr. Tingkun Liu, Mr. Liubin Xu, Ms. Di Xie, Ms. Yi Yang, Mr. Dong Han, Dr. Peijun Hou, Dr. Shuying Chen, Dr. Hui Wang, Dr. Ling Wang and many other friends who give me support and help.

Finally, I would like to acknowledge the Manufacturing and Materials Joining Innovation Center (Ma2JIC) and National Science Foundation for their funding of this work.

Abstract

Friction stir welding (FSW) has found increased applications in automotive and aerospace industries due to its advantages of solid-state bonding, no fusion and melting, and versatility in various working conditions and material combinations. The extent and quality of the solid-state bonding between workpieces in FSW is the ultimate outcome of their industrial applications. However, the relationship among processing parameters, material properties, and bonding extent and fidelity remains largely empirical, primarily because of the lack of the mechanistic understanding of (1) tool-workpiece frictional behavior, and (2) bonding formation and evolution.

In this dissertation, to study the underlying mechanism of tool-workpiece frictional behavior and bonding evolution at workpiece-workpiece interface during solid-state bonding process, firstly, a numerical model that take advantage of Coupled Eulerian Lagrangian (CEL) method is implemented to investigate the stick-slip behavior at tool-workpiece interface. An analytical model is also developed to correlate the stick-slip fraction to processing parameters such as the tool spin rate, and further to derive dimensionless functions for torque and heat generation rate predictions. These analyses provide the critical strain rate and temperature fields that are needed for the bonding analysis. Then, we note that the interfacial solid state bonding process under applied thermomechanical loading histories is a reverse process of the high temperature creep fracture of polycrystalline materials by grain boundary cavities, in this regard, a general modeling framework of bonding fraction evolution was derived, which directly depends on the stress, strain rate, and temperature fields near the interface. Finally, Based on the stick-slip contact analysis and the understanding of solid-state bonding mechanism, an approximate yet analytical solution has been developed to derive the bonding fraction field from the given processing, geometric, and material constitutive parameters, and the predicted ultimate bonding extent with respect to these parameters becomes a figure of merit for the study of processing window for industrial applications and design of the FSW process.

Table of Contents

1 Introduction 1
1.1 Background and motivation 1
1.1.1 Friction stir welding 1
1.1.2 Numerical simulation method 3
1.1.3 Tool-workpiece stick-slip conditions and heat generation rate 5
1.1.4 Solid-state bonding 7
1.2 Outline 10
2 Friction stir welding modeling and tool-workpiece stick-slip conditions 12
2.1 Introduction 12
2.2 Heat generation rate 14
2.3 Computational fluid dynamics simulation 16
2.3.1 CFD simulation by FLUENT 16
2.3.2 CFD simulation results 20
2.4 Coupled-Eulerian-Lagrangian finite element simulation 26
2.4.1 CEL simulation by ABAQUS 26
2.4.2 CEL simulation results 29
2.5 Analytical stick-slip model based on Hill-Bower similarity analysis 31
2.5.1 Hill-Bower similarity analysis for contact problems 31
2.5.2 Analytical solution for the torsional contact problem 35
2.5.3 Comparisons to numerical simulations 37
2.5.4 Comparisons to experimental measurements 41
2.6 Conclusions 43
3 Solid-state-bonding mechanism in friction stir welding 44
3.1 Introduction 44
3.2 Friction stir welding processing modeling 46
3.2.1 Friction stir welding simulation through CEL 46
3.2.2 Thermal and mechanical variables distribution 48
3.3 Cavity closure as the bonding process 51

3.4 Conclusions 55
4 Analytical and computational mechanics modeling of the solid-state bonding 57
4.1 Introduction 57
4.2 The solid-state bonding model 60
4.3 Bonding prediction from CEL-based numerical simulations 66
4.3.1 Model setup 66
4.3.2 Predicted bonding evolution in abutting workpieces 68
4.3.3 Predicted bonding evolution in cladding configuration 75
4.4 An analytical model for the prediction of bonding extent in FSW 75
4.5 Comparisons between numerical and analytical models 86
4.6 Conclusions 90
5 Micromechanical investigation of the role of percolation on ductility enhancement in metallic glass composites 94
5.1 Introduction 94
5.2 Constitutive model for BMGs 98
5.3 Numerical simulation results 101
5.4 Conclusions 115
6 Conclusions and perspectives 117
List of references 120
Vita 130

List of tables

Table 1.1 Three contact conditions. 5
Table 2.1 Constitutive parameters used in our simulations for AA2024 aluminum alloy [49] 17
Table 2.2 Constitutive parameters used in the Johnson-Cook model for AA6061-T6 [44]. 28
Table 2.3 Thermomechanical properties for AA6061-T6 [44, 56]. 28
Table 4.1 Constitutive parameters used in our CEL simulations of AA6061-T6 [88, 89]. 65
Table 4.2 Thermomechanical properties for AA6061-T6 [44, 56]. 69
Table 5.1 Representative values for material parameters in the free volume model of the BMG phase. 102
Table 5.2 Representative values for material parameters in the conventional Mises plasticity model of the Ni phase. 102

List of figures

Figure 1.1 Schematic of FSW. 2

Figure 1.2 Schematic illustration of various solid-state-bonding models. (a) Rough surface contact between two workpieces is usually supported by isolated and widely separated asperities. (b) Bonding two workpieces is equivalent to the shrinkage and closure of interfacial cavities. 9

Figure 2.1 Three types of friction models: (a) pseudo-sticking-state model in CFD simulations[40]; (b) empirical frictional boundary condition in CFD simulations[39]; (c) Coulomb friction used in finite element simulations. 19

Figure 2.2 Temperature, velocity, strain rate, and flow stress fields as predicted by CFD simulations using different frictional boundary conditions: (a) pseudo-sticking-state model in Figure 2.1(a); (b) empirical frictional boundary condition in Figure 2.1 (b); (c) no slip boundary condition (equivalent to infinite μ_f). 21

Figure 2.3 Flow chart for the pressure iteration process, where p is the pre-specified pressure value in CFD simulations. 24

Figure 2.4 (a) Probability distribution of the computed pressure value (actually the normal stress of the workpiece at contact). (b) The average pressure at each iteration. These results correspond to the CFD simulation results in Figure 2.2(a). 25

Figure 2.5 Problem setup in the Coupled-Eulerian-Lagrangian (CEL) finite element simulation for the FSW process: (a) initial configuration, (b) during the welding process. 27

Figure 2.6 CEL simulation results showing the temperature fields in workpiece #2 during each FSW stage with three different friction coefficients. Refer to Figure for model setup. 30

Figure 2.7 CEL simulation results showing the velocity field in workpiece #2 during each FSW stage with three different friction coefficients. Refer to Figure for model setup. 30

Figure 2.8 CEL simulation results showing the material flow stress (top row) and velocity (bottom row) of the workpieces right underneath the tool for μ_f =0.5. Positive location corresponds to the advancing side (workpiece #1), and negative location to the retreating side (workpiece #2). 32
Figure 2.9 Steady-state distribution of workpiece velocity right underneath the tool, as calculated from CEL simulations in Figure , for three different friction coefficients. 32
Figure 2.10 (a) Schematic illustration of the stick-slip condition at the tool-workpiece interface. The boundary is circular when the lateral moving speed is much less than ωa. (b) Solutions of the interfacial shear stress. 33
Figure 2.11 Analytical prediction of the normalized torque in (a) and the normalized heat generate rate in (b) as a function of the contact state (i.e., $1-c/a$), together with the CFD simulation results based on the empirical friction boundary condition in Figure 2.2(b). The parameter ω_0 is 600 rpm. 39
Figure 2.12 Analytical prediction of the normalized torque in (a) and the normalized heat generate rate in (b) as a function of the contact state (i.e., $1-c/a$), together with the CEL simulation results that correspond to results in Figure 2.6-Figure 2.9. The parameter ω_0 is 1000 rpm. 40
Figure 2.13 Comparisons among our analytical model, numerical simulations, and literature experimental data on: (a) the normalized torque (with experimental data compiled from Peel et al.[63]), and (b) the normalized total heat generation rate (with experimental data compiled from Roy et al.[65]). Numerical simulations are from Figure 2.12, so that ω_0 is 600 rpm. 42
Figure 3.1 Finite element setup using the coupled Eulerian-Lagrangian (CEL) approach in the friction stir welding (FSW) process. 47
Figure 3.2 Representative results of the strain rate, temperature, and Mises stress fields are given with their corresponding tool locations, where the graininess on the workpiece surface results from plastic flow. 49

Figure 3.3 (a) Thermomechanical histories of the four reference points are plotted on top of the deformation mechanism map of Al6061-T6 alloy. These histories are located in the dislocation creep regime. (b) Contour plot of the Needleman-Rice length scale, L_{NR}, with respect to the normalized stress and the homologous temperature. The thermomechanical histories are schematically overlaid on this plot. The discrete squares indicate the occurrence of full bonding for the four reference points. 50

Figure 3.4 Schematic illustrations of bonded and unbonded regimes on the workpiece-workpiece interface. Cavities tend to be lens like because of the balance of surface tensions, but they may coalescence into meandering stripes at a low degree of bonding. 52

Figure 3.5 The evolution of f_b (i.e., the area fraction of bonding and no cavities) for the four reference points, with two initial values representing smooth and rough workpiece-workpiece interface. 54

Figure 4.1 Schematic illustration of various solid-state-bonding models. (a) Rough surface contact between two workpieces is usually supported by isolated and widely separated asperities. (b) Bonding two workpieces is equivalent to the shrinkage and closure of interfacial cavities. (c) A discrete array of cavities, which can be closed by creep-controlled or diffusive processes, is homogenized into a field of bonding fraction, $f_b\left(x_\alpha, t\right)$. 58

Figure 4.2 (a) The contour plot of the Needleman-Rice length scale, L_{NR}, with respect to the homologous temperature and normalized stress, which dictates the relative significance of diffusive and creep-controlled processes for cavity closure. (b) The corresponding contour plot of strain rates for AA6061-T6 aluminum alloy. Overlaid on these plots are the thermomechanical histories of three reference points (B, D, and E) from Figure 4.3(b). The orange markers denote the instant of tool front reaching these points, and the purple ones denote the condition of reaching full bonding for B and D and the condition of tool leaving point E. 64

Figure 4.3 Finite element setup using the Coupled Eulerian-Lagrangian (CEL) approach for the FSW process. (a) Delineation of various Eulerian and Lagrangian domains in the model. (b) Cross-sectional view of the two workpieces with the dashed box being the tracking area. (c) The cladding-substrate interface with the dashed box being the tracing area. 67

Figure 4.4 The evolution of bonding fraction, f_b, for the five reference points in Figure 4.3 (b), based on the calculated strain-rate and temperature fields from CEL simulations. Two initial values, f_b^0 =0.01 and 0.2, represent initially smooth and rough workpiece-workpiece interface.(a) Reference points A, B, and C, moving away in x direction. (b) Reference points B, C, and E, moving away in the depth direction. 71

Figure 4.5 (a) Contour plots of the final bonding fraction with respect to varying ω for the FSW process in Figure 4.3 (b), with V_t =2 mm/s and h_p =0.07 mm. (b) The corresponding bonding fraction distribution in the depth direction. (c) The bonding extent with respect to varying ω when taking the critical bonding fraction for full bonding as 0.8. 72

Figure 4.6 The final bonding extent for the FSW process in Figure 4.3 (b). (a) Varying V_t with ω =1000 rpm and h_p =0.07 mm. (b) Varying h_p with ω =1000 rpm and V_t =2 mm/s. 74

Figure 4.7 (a) Contour plots of the final bonding fraction with respect to varying ω for the cladding problem in Figure 4.3 (c), with V_t =2 mm/s and h_p =0.07 mm. (b) The corresponding bonding fraction distribution along the dashed line in Figure 4.3 (c). (c) The bonding extent with respect to varying ω when taking the critical bonding fraction for full bonding as 0.8. In these calculations, the cladding thickness is d =1 mm. 76

Figure 4.8 The final bonding extent for the FSW cladding process in Figure 4.3 (c). (a) Varying V_t with ω=1000 rpm and h_p=0.07 mm. (b) Varying h_p with ω=1000 rpm and V_t=2 mm/s. 77

Figure 4.9 Our analytical model of the interface stick-slip behavior and the shear stress distribution. There exists an annular sliding zone ($c \le r \le a$) in which the theoretical shear stress at infinite friction is larger than the Coulomb friction as determined from the normal pressure distribution. The red dashed curve represents our approximate yet analytical solution. The resulting strain rate field in the substrate provides the critical input for bonding analysis..... 77

Figure 4.10 From CEL finite element simulations Figure 4.3 (but with the lateral motion turned off), the normalized torque, $M_z/\mu_f Pa$, is plotted against the tool rotational speed, ω. 80

Figure 4.11 A dimensionless parametric group, combining ω, a, M_z, and workpiece material viscosity of η, is plotted against the stick-slip ratio of c/a. Blue diamonds are CEL simulation results with five different values of ω. Blue asterisk is the analytical solution at c/a=1. The red dashed curve represents a fitting equation, to be used to construct our flowchart in Figure 4.13. 81

Figure 4.12 Schematic illustrations of the coordinates, stick-slip behavior, and interfaces in our bonding analysis, in which (a) corresponds to Figure 4.3 (b), and (b) corresponds to Figure 4.3 (c). 84

Figure 4.13 A flowchart representing our approximate yet analytical solution from the processing, geometric, and material constitutive parameters to the bonding fraction evolution. 85

Figure 4.14 Comparisons between the CEL numerical simulation results in Figure 4.5(b) and our analytical model for the bonding fraction distribution along the depth direction in the FSW setup in Figure 4.3(b)..... 88

Figure 4.15 The dimensionless function, $E(c/a)$, in the flowchart of Figure 4.13..... 88

Figure 4.16 The final bonding fraction distribution on the cladding-substrate interface along the dashed line in Figure 4.3 (c), with respect to various choice of cladding thickness of d 89
Figure 4.17 The stick-slip ratio with respect to two processing parameters (axial pressure and tool rotational speed), obtained from the CEL numerical simulations of the FSW setup in Figure 4.3 (b) and our analytical solution based on Figure 4.13. 91
Figure 4.18 The final bonding extent on the workpiece-workpiece interface with respect to two processing parameters (axial pressure and tool rotational speed), obtained from the CEL numerical simulations of the FSW setup in Figure 4.3 (b) and our analytical solution based on Figure 4.13. 92
Figure 5.1 Schematic illustration of the dependence of tensile ductility on the volume fraction of the second phase, together with the percolation limits in which the divergence corresponds to some physical properties that rely on the connectivity of the two constituent phases..... 96
Figure 5.2 (a) Pure Ni foam was used to prepare a BMG composite, in which the Zr-based BMG phase infiltrated into the open space in the foam. (b) SEM image shows some detailed features of the open-cell structure in the Ni foam. (c) The as-cast rod of BMG-Ni composite. Note the same scale bar applies to both (a) and (c)..... 96
Figure 5.3 The engineering stress versus engineering strain curves for a Zr-based monolithic BMG and the BMG-Ni composite..... 97
Figure 5.4 Schematic illustration of the BMG-composite model with various microstructural features, in which the red regime represents the BMG phase and the gray regime represents the crystalline second-phase. (a) One inclusion model with H=2.5mm and R=0.4mm. (b) Five inclusion model with H=2.5mm and R=0.3mm. These two models will be used to investigate the shear-band nucleation behavior. (c) Particulate composite model with L=19mm and B=10mm. The volume fraction of the second phase can be tuned by varying both *l* and *r*. (d) Honeycomb composite model with L=19mm and B=10mm, to

mimic the foam-based composite in Figure 5.2. The thickness *t* can be varied to change the volume fraction. 103

Figure 5.5 From the geometric setup in Figure 5.4 (a), the shear-band nucleation site and the subsequent propagation are sensitive to the mechanical properties of the second phase: (a) with Ni being the second phase, and (b) with the second phase being rigid. In these contour plots, SDV1 represents the normalized free volume. 105

Figure 5.6 From the geometric setup in Figure 5.4 (b), the initiation and propagation of shear bands exhibit a strong dependence on the mechanical properties of the second phase: (a) with Ni being the second phase, (b) the same as Ni but with a three-times increase of the Young's modulus, (c) with a five-times increase of the Young's modulus. All these figures are plotted when the macroscopic applied strain equals to 0.1. 105

Figure 5.7 Corresponding to the simulation results in Figure 5.6, the probability distribution of Mises strain in the BMG phase is plotted when the macroscopic applied strain equals to 0.1. With the increase of the Young's modulus of the second from that of Ni to three-times and five times, it becomes less likely to find out the location in BMG phase with large shear strain, meaning that the stiff second-phase suppresses the extent of shear localization in the BMG phase. 106

Figure 5.8 Schematic illustration of the BMG-composite models and the mechanical response on the second phase. (a) For a shear force dipole applied on the circular second phase, the deformation resistance (see text for the mathematical representation) scales as $1/R^2$. Thus the lower the volume fraction of the second phase, the smaller its deformation resistance and the higher the effective shear strain of the neighboring shear band that applies this shear force dipole to the second phase. (b) In the honeycomb configuration, the bending resistance scales as $1/t^3$, so that a low volume fraction has a reduced resistance to the neighboring shear band propagation. 107

Figure 5.9 Contour plots of the maximum in-plane principal strain in BMG-composite model of Figure 5.4 (c), when the applied macroscopic strain equals to 0.13. The volume fraction of the Ni phase ranges from 10% to 90% as labeled.... 110

Figure 5.10 Contour plots of the temperature field in BMG-composite model of Figure 5.4(c). The volume fraction of the Ni phase ranges from 10% to 90% as labeled. It should be noted that these snapshots were taken at different applied strains than those in Figure 5.9. 110

Figure 5.11 Corresponding to the simulation results in Figure 5.9, the probability distribution of Mises strain in the BMG phase is plotted when the macroscopic applied strain equals to 0.04. Only the portion of the BMG phase with the Mises strain larger than 0.04 is included in these probability plots. The probability at high Mises strain reduces as the volume fraction increases, meaning the shear bands are more effectively blocked and thus have reduced shear-strain magnitude. Red-dotted curves provide a logarithmic fitting and thus gives the extent of the maximum shear-band strain. 111

Figure 5.12 Contour plots of the maximum in-plane principal strain in the honeycomb BMG-composite model of Figure 5.4 (d), when the applied macroscopic strain equals to 0.13. The volume fraction of the Ni phase ranges from 10% to 90% as labeled. 112

Figure 5.13 Contour plots of the temperature field in the honeycomb BMG-composite model of Figure 5.4 (d). The volume fraction of the Ni phase ranges from 10% to 90% as labeled. Note that these plots use different legend bounds. As the ductility is enhanced, the temperature “localization” becomes more “diffused”. 112

Figure 5.14 Corresponding to the simulation results in Figure 5.12, the probability distribution of Mises strain in the BMG phase is plotted when the macroscopic applied strain equals to 0.04. The probability at high Mises strain reduces significantly as the volume fraction increases. Comparing these results to Figure 5.11, it can be concluded that the honeycomb composite is more effectively in reducing shear band strains than the particulate composite. Again

red-dotted curves provide a logarithmic fitting and thus gives the extent of the maximum shear-band strain. 113

Figure 5.15 The maximum shear-band strain in the BMG phase as a function of the volume fraction of the second phase for the particulate and honeycomb composites when the macroscopic applied strain equals to 0.04. These datapoints are essentially the rightmost limits in Figure 5.11 and Figure 5.14, as obtained from the red-dotted logarithmic fitting curves. Again it can be concluded that the honeycomb composite is more effectively in blocking the shear-band propagation. 114

1 Introduction

1.1 Background and motivation

1.1.1 Friction stir welding

Welding, a long history metalworking technique has been developed rapidly since 19th century. Currently arc welding, gas welding and resistance welding are popular applied in industry[1]. The basic principle for these welding processes is melting the workpiece or solder to joint parts together, but during these processes high residual stress due to melting will highly decrease the mechanical property of workpiece. Along with higher quality requirement in aerospace, automobile and some other industries, more welding method were exploited. Friction stir welding (FSW) is one of these newly developed methods. As firstly invented by The Welding Institute (TWI) of UK in 1991, FSW bonds the two workpieces in butt configuration under significant heat generated from tool-workpiece frictional sliding and plastic deformation in the workpieces [2-4]. As no melting is involved, the inherent advantage of the FSW process is its immunity from solidification-induced cracking and porosity generation, Furthermore, severe thermomechanical deformation in the weldment zone is capable of refining the material microstructure and resulting into enhanced mechanical properties such as tensile strength and toughness [2, 5, 6]. Figure 1.1(a) and (b) schematically shows the FSW process and three stage of this welding technique. Along with lightweight, high-strength alloys become more and more popular used by manufacturers and the unique advantages of FSW that mentioned above, FSW found its potential applications in industry[3], at the same time, a mature FSW technique will be highly demanded in related field.

Currently, as illustrated in Figure 1.1, a critical assessment of the FSW process needs to focus on the following three issues:

1) The tool and workpiece surfaces in contact will develop into stick and slip regimes due to the finite friction condition. The sliding zone generates heat by frictional process, while additional heating is generated everywhere in the workpieces by

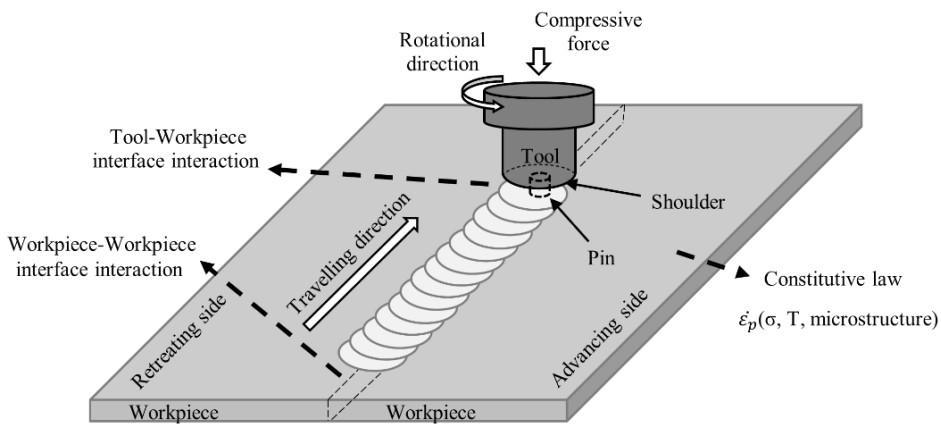

(a)

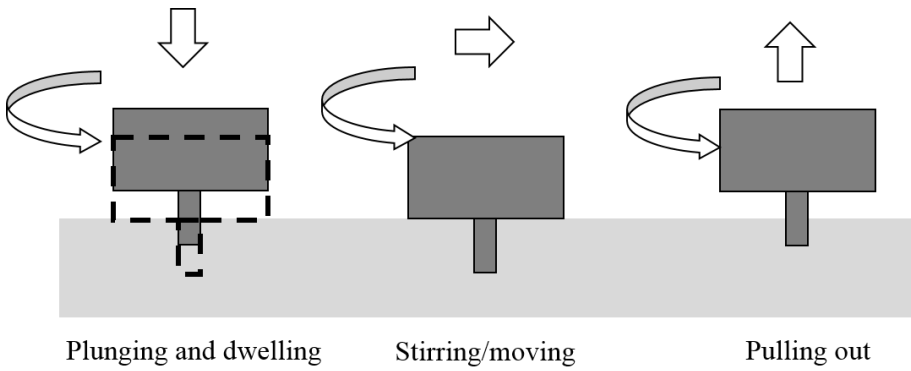

(b)

Figure 1.1 Schematic of FSW.

plastic deformation. How and to what extent the stick-slip behavior is developed dictates the heat generation rate, material flow, and mechanical responses such as the torque applied on the tool. This is the focus of Chapter 2.

2) The extent and quality of the solid-state bonding between workpieces in friction stir welding remains as the ultimate outcome of their industrial applications. Solid-state bonding models can be summarized as primarily inter-diffusional bonding and asperity crushing model [7]. Our preliminary analysis takes a different viewpoint by considering the closure of interfacial cavities, driven by the synergy of lateral diffusional flow and triaxial creep deformation [8], which opposes to almost all the conventional models reviewed by Cai et al [7]. A detailed analysis of the bonding analysis requires inputs of the strain-rate and temperature fields, both of which rely on the stick-slip analysis. Results from Chapter 2 thus provide the foundation for the bonding model in Chapter 4.
3) Any quantitative numerical prediction needs well calibration constitutive models for the workpiece material, of which the difficulties lie on the microstructural evolution associated with the severe plastic deformation. This issue will not be elaborated here, and we restrict our studies to the hyperbolic-sine creep law and the Johnson-Cook model.

1.1.2 Numerical simulation method

Currently, the whole friction stir welding process is more like an art instead of science as the underlying mechanisms are still not very clear. The researches on FSW are highly depend on experiments which take long schedule time but with low success rates. Compared to experimental method, numerical simulation is normally less expensive, more efficient and has fewer limitations which make it a promising approach to understand the mechanism of whole FSW process.

Depends on different mechanisms, numerical model for FSW process simulation could be classified into two main categories: (1) Computational fluid dynamics (CFD) based model and (2) Computational solid mechanics (CSM) based model. Both of these two kinds of numerical models are widely used by researchers in FSW study, due to the

advantages and drawbacks associated with CFD and CSM method, different models will be selected based on different requirement during investigation.

For CFD based model, as material is regarded as Non-Newtonian viscous fluid, so it could deal with complex material flow. For example, Bendzsak et al developed a 3D CFD simulation program STIR3D for FSW [5] process. In their work, material flow was successfully analyzed through this software and three quite distinct flow regimes were founded below the tool shoulder which correspond with the actual weld micrographs observation. Nandan et al derived a mathematical model for FSW process to investigate the 3D viscoplastic flow and temperature field [9], they also modeled the torque and power requirement during FSW of AA2524 [10]. By using the commercial CFD package, FLUENT, Colegrove build up both 2D and 3D CFD models to investigate the material and heat flow during FSW process[11-13], simulation results also help to assist the design of welding tool. Recently Liu implemented a coupled thermal-mechanical model into the FLUENT for dissimilar FSW process simulation, in her work, the feature of embedded steel strip in aluminum side was captured[14]. Seidel and Reynolds adopted 2D CFD based model to investigate the material flow around the tool[15]. Ulysse conducted 3D simulations through a commercial CFD software, FIDAP, the effect of tool speeds on welding temperature and reaction force [16] were studied in his work. Colegrove and Shercliff used FLUENT to study the temperature distribution and 3D material flow pattern around the tool with complex geometry, whereas the role of tool rake angle and tool speed in affecting the flow pattern were also investigated [11, 13].

For CSM based model, behavior of workpiece material is described by elastic-plastic constitutive laws. Schmitdt and Hattel developed a 3D fully coupled thermomechanical model through arbitrary Lagrangian-Eulerian (ALE) method in ABAQUS/Explicit[17], in their work the primary condition to fill cavity behind the tool is analyzed. CSM based model is also used by Zhang et al to investigate the effect of axial pressure in FSW, they found that axial pressure plays a key role in FSW by affecting the material flow, temperature distribution and influence region under shoulder[18]. Zhu developed a finite element analysis code WELDSIM for welding simulation, in this work

he studied the residual stress and transient temperature of 304L stainless steel in FSW and these simulation results show well consistent with experimental data[19].

1.1.3 Tool-workpiece stick-slip conditions and heat generation rate

In the FSW process modeling, one of the critical parts is the contact condition as the material flow at the tool-workpiece correlated with the tool velocity through the contact condition. Typically three kinds of contact states may exist at the interface, which are: sliding, sticking and partial sliding/sticking[20].

For sliding condition, it happens when the contact shear stress is smaller than the matrix material's yield stress. On contrary, when the friction shear stress at the interface exceeds the matrix's yield shear stress, the material underneath the tool surface will stick to the moving tool. In this case, matrix will initially accelerate with moving tool (finally achieve same velocity with tool) until the contact shear stress and matrix yield shear stress reach to an equilibrium state, then a fully sticking condition is fulfilled. Apart from the above conditions, there is partial sliding/sticking condition that will occur when the contact shear stress equal to the material yield stress at low strain rate, for this case, the matrix material underneath the tool will accelerate to a velocity that is lower than the tool velocity.

Schmidt, Hattel and Wert defined a contact state variable which could relates the matrix velocity at contact surface to tool velocity as follows[21]:

$$\delta = \frac{v_{matrix}}{v_{tool}} = 1 - \frac{v_{relative}}{v_{tool}} \tag{1.1}$$

in which $v_{relative} = v_{tool} - v_{matrix}$. As show in Table 1.1.

For heat generation, the most widely used analytical model was based on Schmidt and Hattel's works [20, 21], in which a dimensionless parameter δ is introduced to measure the extent of slip. When δ varies from 0 to 1, the interface transitions from fully sticking to fully sliding. Based on these works and numerous follow-up studies, Nandan

Table 1.1 Three contact conditions.

Contact condition	Matrix velocity	Tool velocity	Contact shear stress	State variable
Sticking	$v_{matrix}=v_{tool}$	$v_{tool}=\omega r$	$\tau_{contact}=\tau_{yield}\left(\uparrow \dot{\varepsilon}\right)$	$\delta=1$
Sticking/Sliding	$v_{matrix}<v_{tool}$	$v_{tool}=\omega r$	$\tau_{contact}=\tau_{yield}\left(\downarrow \dot{\varepsilon}\right)$	$0<\delta<1$
Sliding	$v_{matrix}=0$	$v_{tool}=\omega r$	$\tau_{contact}<\tau_{yield}$	$\delta=0$

et al. [3] and Yu et al. [22] concluded that the differential heating rate is given by

$$dq = \left[\delta \mu_f p + (1-\delta) \tau_{yield} \right] \omega r dA \tag{1.2}$$

where r is the radius from the tool center, ω is the tool angular velocity (in the unit of radian per second), τ_{yield} is the shear yield strength of the workpiece material, μ_f is the friction coefficient, and p is the normal contact pressure. The common statement in all the above works is that all the heat is generated by friction at the tool-workpiece contact interface when δ =1, and due to shear plastic deformation when $\delta = 0$. Nandan et al. added another term as the heating from plastic deformation away from the tool-workpiece interface[3]. The former interpretation is problematic, and the latter is incorrect. A detailed explanation of the heat generation rate and the critical issues in boundary conditions (especially p and δ) in CFD simulations will be presented in Chapter 2.

1.1.4 Solid-state bonding

Welding and joining various components into a strong, durable and cost-effective engineering structure is a critical process in many industrial applications. The conventional fusion welding may not have the stress concentration and common fatigue intolerance problem as fastening and riveting, but the related high temperature could dramatically change the microstructure of the base material and therefore lead to the weakest links for premature failure. In order to overcome these drawbacks in fusion welding, there exists a wide range of solid-state bonding techniques, such as diffusion bonding where workpieces are held by compressive force at elevated temperature [23, 24], frictional bonding where two abutting workpieces spin against each other for heat generation [7], ultrasonic welding [25, 26], impact or explosive welding [27, 28], and friction stir welding (FSW) where a spinning and traversing tool onto two workpieces in butt configuration generates significant heat and deformation field [2, 3]. Impact welding is motivated from the accidental finding during World War I that pieces of shrapnel were found to weld to the target armor plates, when these two metallic materials collided under high strain rate. In friction-based welding techniques, heat is generated from both mechanical friction and severe plastic deformation. Diffusion bonding derives its name from the belief that

interdiffusion across the two workpieces will promote the formation of atomic bonding. Because of no melting and solidification processes involved in the above solid-state bonding techniques, the resulting products could be immune from defect generation and property deterioration such as solidification cracking and unwanted microstructural evolution.

When brought into contact, any two metallic materials will not immediately bond together unless they are atomically smooth and contamination free, i.e., "crack healing" does not happen in realistic conditions. In the cold welding experiment by Lu et al.[29], two ultrathin gold nanowires were brought to contact in their ends, but the mating surfaces are at most atomistically faceted/ledged and thus essentially flat. Such successes hardly exist for large objects. Adhesive forces of the long-range nature, such as van der Waals interaction or capillary force, cannot deform roughness asperities sufficiently for contact conformity because of the high stiffness of metallic materials. Naturally, it is anticipated that the solid-state bonding will be achieved at high compressive loads and high temperatures. It is therefore often believed that the bonding mechanisms include two stages [7, 23, 30]: (1) plastic crushing of rough surface asperities under an applied load which establishes an initial contact with a high fraction of true contact area, and (2) atomic interdiffusion by which atoms transport across the workpiece interface and promote the gap closure. In Hamilton [31] and Chen et al. [32]'s works, surface roughness is regarded as a succession of extended ridges or asperities, which are deemed to be flattened by the plastic deformation under pressure. However, rough surface contacts, as schematically illustrated in Figure 1.2(a), are usually manifested microscopically by a small number of widely separated asperities per unit area. Even if a multi-affine or fractal roughness is considered (simply speaking, fine asperities on top of coarse asperities), the full plastic solutions in Gao and Bower's work [33] suggest that the lateral interactions of neighboring asperities and the additional compliance onto fine asperity contacts from the coarse asperity scale make it extremely difficult to realize a high fraction of true contact area. Besides, any theoretical model along this line suffers the same problem of illposedness of roughness

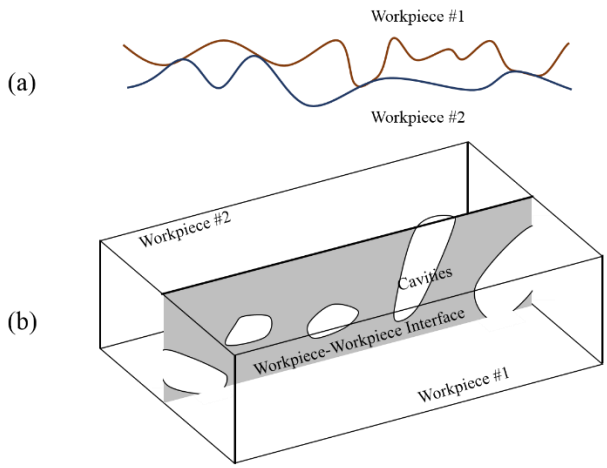

Figure 1.2 Schematic illustration of various solid-state-bonding models. (a) Rough surface contact between two workpieces is usually supported by isolated and widely separated asperities. (b) Bonding two workpieces is equivalent to the shrinkage and closure of interfacial cavities.

characterization due to the fractal nature, so the connection between the rough surface contact analysis and the bonding evolution remains largely qualitative [34]. As will be shown later in this work, we believe that it is futile to dwell on the rough surface contact, because the majority time spent in the bonding evolution is on the creep-dominated cavity closure while different degrees of surface roughness play a negligible role. Creep solutions are typically very different from fully plastic deformation fields.

The bonding evolution at a slightly later stage can be regarded as the closure of interfacial cavities, which might be long, serpentine and connected, or isolated, as schematically illustrated in Figure 1.2(b). Earlier works in the solid-state bonding suggest the removal of these cavities by volumetric inter-diffusion between the two workpieces, so that Fick's solutions for diffusion couple can be adopted. However, this cannot be the dominant mechanism unless at extremely high temperature, because the activation energy for diffusion ranks from high to low for volumetric, interface, and surface diffusion. At the moderate temperature range in most solid-state bonding techniques, cavity surface diffusion is essentially infinite and bulk diffusion is essentially zero when compared to interface diffusion. Derby and Wallach [35, 36] proposed the interface energy reduction as in the sintering process and the applied joining pressure as the driving forces for the cavity closure, and later Hill and Wallach [37] added plastic deformation in the cavity junctions to these sintering-like analyses. It should be noted that these solutions are from powder sintering, so that cavities are assumed to be closely spaced and the cavity junctions are treated as necks in their plastic deformation analysis. The actual creep deformation field in widely separated cavities will be otherwise different. Additionally, many solid-state bonding techniques are very fast, so that the contribution of diffusional processes might be limited. A new view is needed to interpret the solid-state-bonding behavior during FSW process.

1.2 Outline

This dissertation work is organized as follows. In Chapter 2, we will first conduct FSW process simulations through two CFD-based methodologies and the Coupled Eulerian Lagrangian (CEL) model to investigate the stick-slip condition at too-workpiece

interface. The dependence of interfacial stick-slip behavior on the processing, geometric, and material constitutive parameters and how stick-slip behavior will affect the torque and total heat generation ratio will be studied through both numerical and analytical method. In Chapter 3, we aim to get a quantitative understanding of the solid-state bonding in FSW. A novel view on the solid-state bonding by treating the bonding process as a reverse one to the intergranular fracture in ploycrystalline materials is developed and a quantitative prediction of the bonding fraction will be presented. In Chapter 4, based on the stick-slip contact analysis and the understanding of solid-state bonding, an approximate yet analytical solution has been developed to derive the bonding fraction field from the given processing, geometric, and material constitutive parameters. The predicted ultimate bonding extent with respect to these parameters becomes a figure of merit for the study of processing window for industrial applications and design of the FSW process. In Chapter 5. A thermo-mechanical finite element method based on the free volume model and plasticity-induced heating is developed to investigate the ductility improvement in bulk metallic glass composites (BMGCs). Numerical simulations have been conducted to investigate the role of microstructure and property mismatches on the effectiveness of the second phase in resisting the strain localization in the BMG shear bands.

2 Friction stir welding modeling and tool-workpiece stick-slip conditions

2.1 Introduction

Since the FSW technique involves highly coupled thermomechanical processes, only medium- and far-range temperature and deformation fields can be routinely measured, but short-range stick-slip properties underneath the tool are not easily amenable to experimental investigations. Clearly, numerical simulations have advantages in evaluating frictional behavior, contact condition, material flow patterns, and others during such severe thermomechanical processes. The most widely used approach is computational fluid dynamics (CFD), in which workpieces are oftentimes modeled as non-Newtonian fluids and their elastic response is neglected. For example, Seidel and Reynolds adopted two-dimensional (2D) CFD to investigate the material flow around the tool[15]. Ulysse conducted three-dimensional (3D) simulations using a commercial CFD software, FIDAP, and studied the effect of tool speeds on welding temperature and reaction force [16]. Colegrove and Shercliff used FLUENT (another commercial CFD software) to study the temperature distribution and 3D material flow pattern around the tool with complex geometry, whereas the roles of tool rake angle and tool speed in affecting the flow pattern were also investigated [11, 13]. The primary advantage of CFD simulations lies on their superior capability of dealing with complex material flow, which is otherwise difficult to handle by Computational Solid Mechanics (CSM) based simulations. However, one critical issue for these CFD simulations is their ad hoc treatments of contact boundary conditions on the tool-workpiece interface. As will be clear from this chapter, the interfacial stick-slip condition not only affects the heat generation rate during welding process, but also dictates the material flow and thus the bonding formation and evolution. It is the full coupling of interfacial frictional stick-slip, material flow, and heat transfer that governs the entire FSW process.

One difficulty in CFD simulations is the shear-stress interface condition [38-40]. Again, as opposed to CSM based models that can naturally calculate the interfacial stress fields from Coulomb friction, ad hoc models have to be introduced in CFD. For example,

Chen et al. introduced a critical relative speed [40], V_C, below which the interface is considered to be in a pseudo-sticking state and the shear stress takes the value of τ_{yield}. Liu et al. implemented an empirical friction-stress model on tool-workpiece interface to study FSW process for dissimilar materials, which led to improved predictions than simulations based on velocity boundary conditions[39]. However, the development of stick-slip conditions was not reported in this work.

Finite element analysis (FEA) can readily solve the frictional contact problem, but Lagrangian-based FEA cannot handle the severe deformation in FSW. To this end, arbitrary Lagrangian-Eulerian (ALE) formulation in ABAQUS was adopted by Xu et al. through re-meshing methodology[41, 42], which modeled the FSW process as a 2D steady state problem and predicted material flow patterns in good agreement with experimental observations. Schmidt and Hattel developed a 3D ALE model through ABAQUS/Explicit and predicted the defect formation during the welding process[17]. But it had reported that ALE method cannot handle excessive mesh distortion and may lead to premature failure in these simulations [43]. Some other works have recently employed the Coupled Eulerian-Lagrangian (CEL) method to simulate the FSW process [44, 45]. In this method, the tool is modeled in Lagrangian formulation and the workpiece in Eulerian formulation. Apart from the material flow pattern, the CEL approach is able to predict volumetric defects and mechanical responses during FSW process. In Section 2.3, we will employ the two ad hoc CFD methodologies as discussed in the preceding paragraph as benchmark examples to compare to our CEL simulation results in Section 2.4 [39, 40], with the focus on comparing the predicted interfacial stick-slip ratios from these different frictional boundary conditions.

Even with all the above simulation works, an analytical interpretation of stick-slip conditions on the tool-workpiece interface, together with their effects on torque and heat generation rate, has never been attempted. It is not even clear whether a steady state ever exists, for which the separation of stick and slip zones has a fixed ratio and is independent of time. In Section 2.5, based on the Hill-Bower model on the similarity relationship in contact analysis, we can now correlate the steady-state stick-slip ratio to processing

parameters, such as tool spinning rate and applied torque. These theoretical predictions can now provide a useful guidance and revisit to experimentally measured data of torque and heat generation rate.

2.2 Heat generation rate

In this section, we first derive the total heat generation rate from both frictional heating and plastic deformation, and then discuss the limitations of ad hoc boundary conditions oftentimes used in CFD simulations. The following theoretical analysis will pave the foundation for comparing CFD and FEA simulations in Sections 2.3 and 2.4.

There are only two sets of field equations in the FSW problem, one being the momentum transfer (or stress balance when inertia force is small) equation in the workpiece, and the other being the bulk energy transport equation, given by

$$\rho C_P \left[\frac{\partial T}{\partial t} + \mathbf{v} \cdot \nabla T \right] = k \nabla^2 T + \alpha_{TQ} \sigma_{ij} \dot{\varepsilon}_{ij}^p \tag{2.1}$$

where ρ is the material density, C_P is the heat capacity, T is the temperature, t is time, $\mathbf{v}$ is the material velocity vector, k is the thermal conductivity, σ_{ij} is the stress tensor, $\dot{\varepsilon}_{ij}^p$ is the plastic strain rate, and α_{TQ} is the Taylor-Quinney ratio that measures the fraction of plastic work converted to heat (e.g., 0.7~0.9 for most metals). Latin subscripts run from 1 to 3. Summation convention is implied for repeated indices. The heat generation rate due to plastic deformation is the integral,

$$Q_{plastic} = \alpha_{TQ} \int_{\Omega} \sigma_{ij} \dot{\varepsilon}_{ij}^p dV \tag{2.2}$$

over the volume occupied by the two workpieces. Neglecting elastic deformation leads to the approximation of $\int_{\Omega} \sigma_{ij} \dot{\varepsilon}_{ij}^p dV \approx \int_{\Omega} \sigma_{ij} \dot{\varepsilon}_{ij} dV = \int_{\Omega} \sigma_{ij} \dot{u}_{i,j} dV$, where the last step is based on the symmetric nature of stress tensor. Using Gauss theorem, we can convert the bulk integral to a surface one, $\int_{\Omega} \sigma_{ij} \dot{u}_{i,j} dV = \int_{S} \sigma_{ij} \dot{u}_i n_j dA - \int_{\Omega} \sigma_{ij,j} \dot{u}_i dV$, and the last term vanishes due to stress balance equations, $\sigma_{ij,j} = 0$. Consequently, the plastic heating rate becomes

$$Q_{plastic} \approx \alpha_{TQ} \int_S \sigma_{ij} \dot{u}_i n_j dA \approx \alpha_{TQ} \int_S \sigma_{3\theta} \dot{u}_\theta dA \tag{2.3}$$

where the subscript θ is the polar coordinate on the tool-workpiece interface, and $\dot{u}_\theta = v_\theta$ is the θ-component of the velocity vector in the workpiece. We also note that the frictional heating only occurs in the sliding zone, given by

$$Q_{friction} = \int_{slip} \mu_f \, p\left(\omega r - \dot{u}_\theta\right) dA \tag{2.4}$$

Consequently, the total heat generation rate is

$$\begin{aligned} Q_{total} &= Q_{plastic} + Q_{friction} \\ &= \alpha_{TQ} \left\{ \int_{stick} \tau_{yield} \omega r dA + \int_{slip} \mu_f \, p \dot{u}_\theta dA \right\} + \int_{slip} \mu_f \, p\left(\omega r - \dot{u}_\theta\right) dA \\ &\xrightarrow{\alpha_{TQ}=1} \int_{stick} \tau_{yield} \omega r dA + \int_{slip} \mu_f \, p \omega r dA \end{aligned} \tag{2.5}$$

Referring back to Eq.(2.1) and assuming α_{TQ}=1, it can be clearly seen that all the heat generation due to plastic deformation can be written as a surface integral inside the stick zone, and all the frictional heating as another surface integral inside the slip zone. Adding another bulk integral for plastic heating is thus not needed.

Most CFD simulations assume a given contact pressure of p and/or prescribe a value of δ a priori as the boundary/interface condition, instead of computing such pressure and stick-slip distributions as CSM can do for the Coulomb friction. Therefore, some of the CFD simulation results need ad hoc adjustments of p and δ when comparing to experimental measurements such as medium- and far-field temperature distribution [22], while some works predict dubious behavior. For example, a fully stick condition was assumed in Colegrove and Shercliff's work [13], which clearly over predicted temperature and material deformation zone size. Atharifar et al. modified the velocity boundary conditions that applied on the tool-workpiece interface to achieve a sliding state, in which the velocity of interface material was assumed to be 65% of the tool velocity [46]. However, they also stated that in order to obtain accurate computational results in various

FSW conditions, velocity boundary needs to be adjusted for different welding parameters. Nandan et al. and Arora et al. introduced an empirical parameter to describe the slipping state at tool-workpiece interface through applying velocity boundary condition at interface, which again needs to be adjusted to achieve a good agreement of temperature and deformation zone in the weld [10, 47].

2.3 Computational fluid dynamics simulation

2.3.1 CFD simulation by FLUENT

In CFD simulations, the workpiece can be assumed to be an incompressible non-Newtonian fluid, with the viscosity given by

$$\mu = \frac{\sigma_e}{3\dot{\varepsilon}_e} \tag{2.6}$$

where σ_e the Mises effective stress and $\dot{\varepsilon}_e$ is the effective strain rate. The temperature and strain-rate dependent model, as suggested by Sheppard and Wright [48], takes the following form,

$$\sigma_e = \frac{1}{\beta}\ln\left\{\left(\frac{Z}{A}\right)^{1/n} + \left[\left(\frac{Z}{A}\right)^{2/n} + 1\right]^{1/2}\right\} \tag{2.7}$$

where A, n, and β are material constants, Z is the Zener-Holloman parameter,

$$Z = \dot{\varepsilon}_e \exp\left(\frac{Q_{def}}{RT}\right) \tag{2.8}$$

R is the gas constant, and Q_{def} is the activation energy. Representative values for these parameters are given in Table 2.1 for aluminum alloy AA2024 [49].

Our CFD simulations were performed using the commercial software FLUENT, in which two metal sheets occupy the space beneath the tool, with a total dimension of 100 mm× 55 mm × 3mm. The radius of tool shoulder is 6.5 mm, and the radii of the tapered tool pin are 2 mm at the root and 1.75 mm at the tip with a height of 2.4 mm. The entire workpiece space is discretized by 337,620 cells. FLUENT provides a user defined function to implement the viscosity function in Eq.(2.6), based on the constitutive law in Eq.(2.7).

Table 2.1 Constitutive parameters used in our simulations for AA2024 aluminum alloy [49]

Density (kg/m^3)	A (s^{-1})	n	Q_{def} (kJ/mol)	β (Pa^{-1})
2.7×10^3	2.29×10^{11}	5.46	178	2.09×10^{-8}

As the Coulomb friction cannot be prescribed in FLUENT, ad hoc boundary conditions have to be prescribed by the user defined functions. Following Mostaghel et al. and Chen et al. [40, 50], the interface shear stress is determined from the relative velocity of the tool and workpiece surfaces, i.e., $\mathbf{v}_{rel} = \left(\omega r - \dot{u}_\theta\right)\mathbf{e}_\theta$ in Eq.(2.4) with $\mathbf{e}_\theta$ being the basis vector in θ coordinate. As shown in Figure 2.1(a), whether any given location falls into sticking or sliding state depends on comparing the magnitude of this relative speed to a critical value, v_c,

$$\tau_f = \mu_f p \operatorname{sgn}\left(\frac{\mathbf{v}_{rel}}{\|\mathbf{v}_{rel}\|}\right)\begin{cases} 1, & \|\mathbf{v}_{rel}\| \geq v_c \\ \tanh\left(\dfrac{\|\mathbf{v}_{rel}\|}{v_0}\right), & \|\mathbf{v}_{rel}\| < v_c \end{cases} \tag{2.9}$$

where v_0 is a reference velocity (taken as 0.02 m/s in this work). In contrast to FEA simulations based on the Coulomb friction law, the predicted stick-slip ratio from this model depends on the choice of v_c. Nevertheless, it provides a way to simulate the development of stick-slip in CFD, as opposed to the rather unphysical choice of fixed δ in many other CFD works. To this end, the condition of $\|\mathbf{v}_{rel}\| < v_c$ is denoted as the pseudo-sticking state.

The other type of boundary conditions in FLUENT used in this study follows the work by Liu et al.[39]. Noting that the interfacial shear stress is always limited by the yield strength of the substrate material, the following fitting equation can be used to represent the transient behavior in Figure 2.1(b) [51],

$$\tau_f = m\tau_{yield}\left\{1 - \exp\left[-\left(\frac{\mu_f p}{m\tau_{yield}}\right)^{n_f}\right]\right\}^{1/n_f} \tag{2.10}$$

where m is called friction factor (taken as 0.95) and n_f is a fitting parameter (taken as 1.7 here). In this model, when $\mu_f p > m\tau_{yield}$, the interfacial shear stress takes the value of $m\tau_{yield}$ which corresponds to the sticking state. That is, the stick-slip ratio is determined from the stress condition, which apparently fails to capture the reality if the materials are

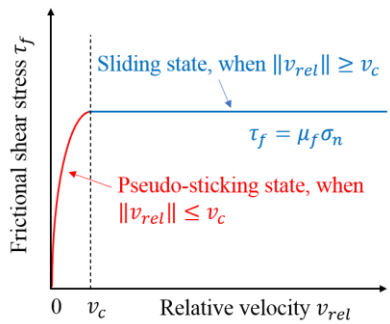

(a)

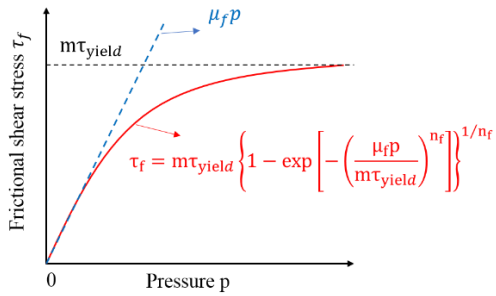

(b)

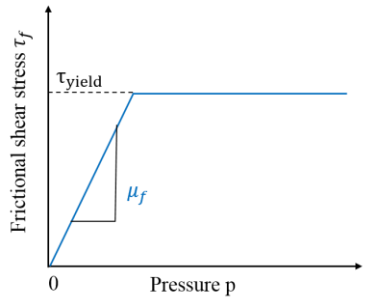

(c)

Figure 2.1 Three types of friction models: (a) pseudo-sticking-state model in CFD simulations[40]; (b) empirical frictional boundary condition in CFD simulations[39]; (c) Coulomb friction used in finite element simulations.

hard. For example, an extremely hard material will never develops the sticking state if taken from Eq.(2.10), which however is known to be untrue.

The above two models have been implemented via user defined functions in FLUENT. For comparison purpose, we also conduct simulations with fully sticking condition, i.e., the workpiece surface follows the motion of the tool surface for the entire simulation history. In all these CFD simulations, the rotational speed ranges from 600 to 1600 rpm, but the tool traveling speed is kept as 20 mm/min.

2.3.2 CFD simulation results

Temperature, velocity, strain rate, and flow stress fields are presented in Figure 2.2 for CFD simulations with the pseudo-sticking-state model in Figure 2.1(a), the empirical friction stress model in Figure 2.1(b), and no-slip boundary condition. Four rotational speeds were specified in these simulations for comparison purpose. It is noted that different interface conditions give rise to different peak temperature values, and thus clearly different heat generation rates. For the infinite friction condition in Figure 2.2(c), temperature is much higher than that from other two models, indicating the significant contributions from plastic heating. The interface stick-slip condition can be obtained by inspecting the radial distribution the velocity of workpiece material right underneath the tool shoulder. This distribution is clearly linear in radial direction in Figure 2.2(c) as it follows the tool rotation, i.e., ωr. It can be seen from the deviation from linearity in Figure 2.2(a) and Figure 2.2(b) that the sticking condition is found in an inner zone (size of c), while an annular sliding zone ($c \le r \le a$ as will be illustrated in Figure 2.10) exists in which the workpiece velocity lags behind that of the tool. Although both Figure 2.2(a) and Figure 2.2(b) show the same trend of increasing c/a with the increase of ω, the exact stick-slip ratio predicted under the same welding parameters is sensitive to the particular interface condition used in these CFD simulations. The strain rate field, being the velocity gradient, shows similar radial distribution. This line of information is critical in predicting the bonding evolution in the Chapter 4. The flow stress relates to temperature and strain rate from the constitutive law in Eq.(2.7), so that it is comparably lower underneath the sticking regime than under the sliding regime.

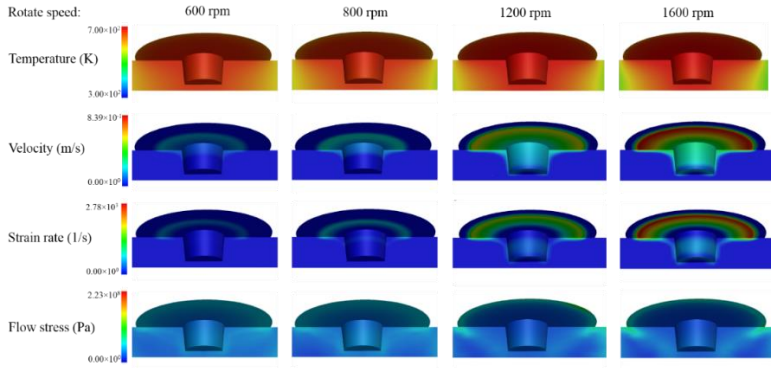

(a)

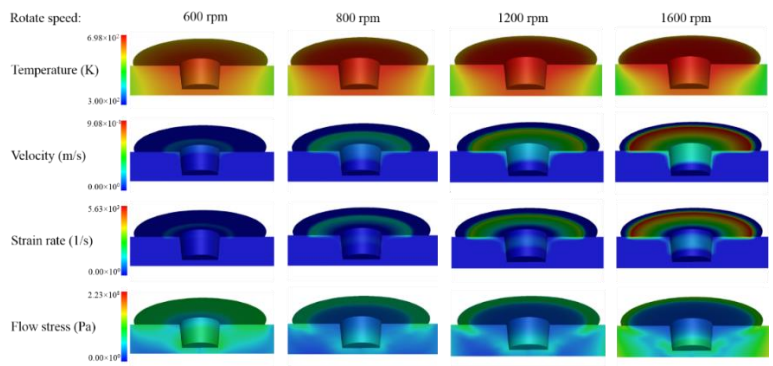

(b)

Figure 2.2 Temperature, velocity, strain rate, and flow stress fields as predicted by CFD simulations using different frictional boundary conditions: (a) pseudo-sticking-state model in Figure 2.1(a); (b) empirical frictional boundary condition in Figure 2.1 (b); (c) no slip boundary condition (equivalent to infinite μ_f).

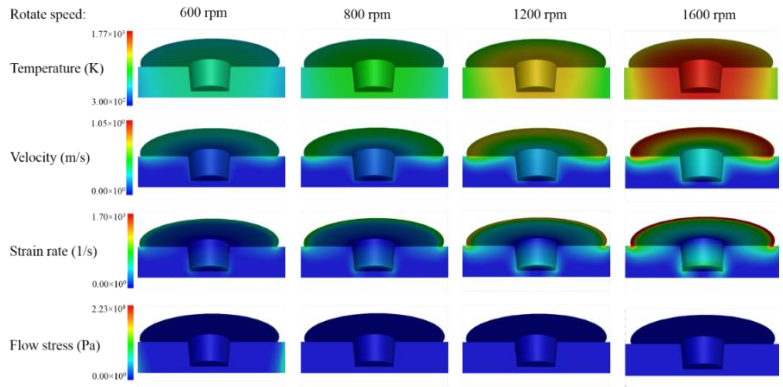

(c)

Figure 2.2 continued

From these results in Figure 2.2, several limitations of CFD simulations can now be seen. First, while all the trends with respect to varying ω are the same, different interfacial conditions give different values of stick-slip ratio, which therefore affects the highest temperature and total heat generation rate. Second, axial force and resulting torque on the tool cannot be directly obtained from CFD simulations; one has to conduct tedious post-processing from the calculated flow stress field. But again the mechanical responses computed in such a way are dubious as all these CFD simulations in Figure 2.2 predict very different thermomechanical fields, albeit the processing and constitutive parameters are the same. Third, when comparing these predictions to experimental measurements that are usually limited to medium- and/or far-range temperature fields, one can arbitrarily change the associated parameters in these ad hoc interface models, such as v_c in Eq.(2.9), to attain a good agreement, which however reduces the confidence in other predicted fields. Fourth, all results in Figure 2.2 are computed from a given pressure (e.g., 50 MPa as adopted here) uniformly distributed from the tool to the workpiece. This is rather a restriction in CFD than a convenient consideration. All these concerns cast challenges to the development of predictive CFD models for FSW.

We now attempt to see whether the strong assumption of a constant and uniform pressure distribution can be relaxed from an iterative process. As shown in the flowchart in Figure 2.3, if the input and computed pressure are not the same, the computed pressure distribution is then taken as the input for the next round of simulations. This procedure will be repeated until two pressures converge. Applying this iteration to the results in Figure 2.2(a), we find out that the area-weighted average pressure converges quickly and decreases from 50 MPa to 39 MPa. As illustrated by the pressure distribution at interface at each iteration in Figure 2.4(a), the final computed pressure distribution shows a clear deviation from the initial applied pressure. Except for several points with extremely high values, for most areas, pressure under the tool is far less than 50 MPa and localized between 30-40 MPa during iteration. Results in Figure 2.4 are for the pseudo-sticking-state model in Figure 2.3(a) and Figure 2.2(a) at a given rotational speed. Although changing ω will also change the final converged pressure value and thus iterations are needed for every set of processing and property parameters, the calculations are very tedious and become

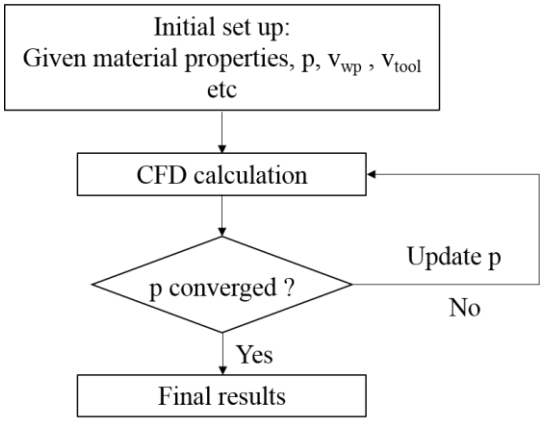

Figure 2.3 Flow chart for the pressure iteration process, where p is the pre-specified pressure value in CFD simulations.

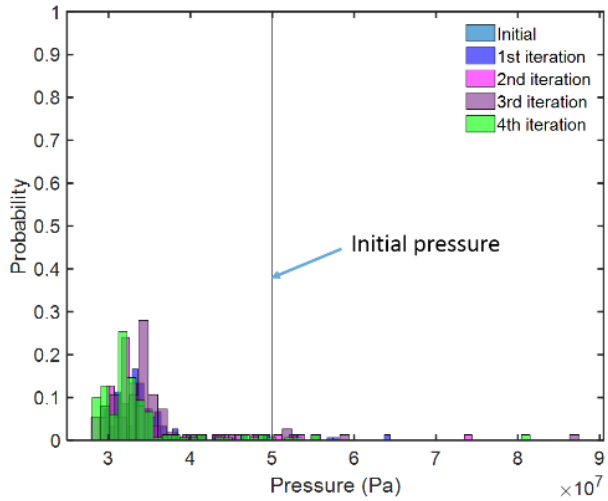

(a)

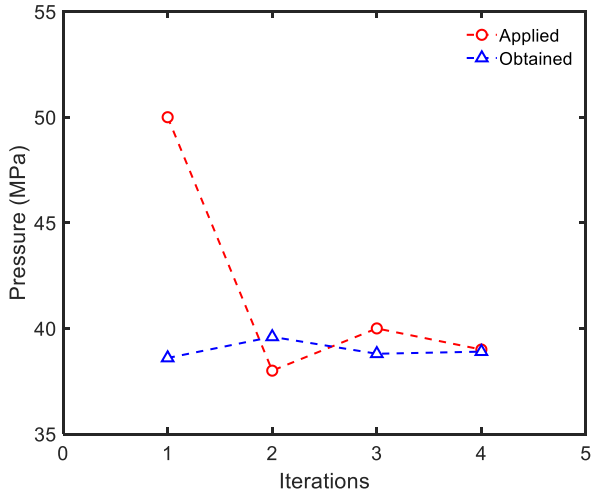

(b)

Figure 2.4 (a) Probability distribution of the computed pressure value (actually the normal stress of the workpiece at contact). (b) The average pressure at each iteration. These results correspond to the CFD simulation results in Figure 2.2(a).

impractical since it oftentimes takes days for individual simulation job to reach the steady state. The final stick-slip ratio after iteration shows some improvement, but it does not change the fact that this pseudo-sticking-state model in Figure 2.1(a) is not a true outcome of frictional contact analysis.

2.4 Coupled-Eulerian-Lagrangian finite element simulation

2.4.1 CEL simulation by ABAQUS

For CEL finite element simulations, we adopt the Johnson-Cook constitutive law [52], which is a strain rate and temperature dependent viscoplastic model, given by

$$\sigma_e = \left(A_{JK} + B_{JK}\varepsilon_e^N\right)\left(1 + C_{JK}\ln\frac{\dot{\varepsilon}_e}{\dot{\varepsilon}_0}\right)\left[1 - \left(\frac{T - T_{ref}}{T_{melt} - T_{ref}}\right)^{m_{JK}}\right] \tag{2.11}$$

where ε_e is the effective strain, $\dot{\varepsilon}_0$ is a characteristic strain rate (taken as 1.0 s^{-1} here), and T_{melt} and T_{ref} are material solidus temperature and reference temperature, respectively. Representative values for the constitutive parameters, A_{JK}, B_{JK}, C_{JK}, N and m_{JK} are given in Table 2.2 for aluminum alloy AA6061-T6. Density of AA6061-T6 is taken as 2690 kgm^{-3}. A 90% fraction of plastic work is assumed to be converted to heat, i.e., α_{TQ} =0.9. The relevant thermomechanical properties, including thermal conductivity, specific heat, friction coefficients, and elastic constants, are taken from several literature works [44, 53-56], as summarized in Table 2.3.

Conventional finite element simulations are based on the Lagrangian view, so needing to solve the Navier-Cauchy equation for momentum transfer. In CEL simulations using the commercial software ABAQUS, the entire control volume is divided into Eulerian and Lagrangian domains, which helps overcome the difficulty in ad hoc frictional modeling in CFD-based models and the difficulty in large deformation in FEA simulations. As shown in Figure 2.5, the tool is modeled as a rigid isothermal Lagrangian body and its movement is controlled by a reference point attached to the bottom surface of the pin. The tool shape and size are the same as in CFD simulations. The entire Eulerian domain is

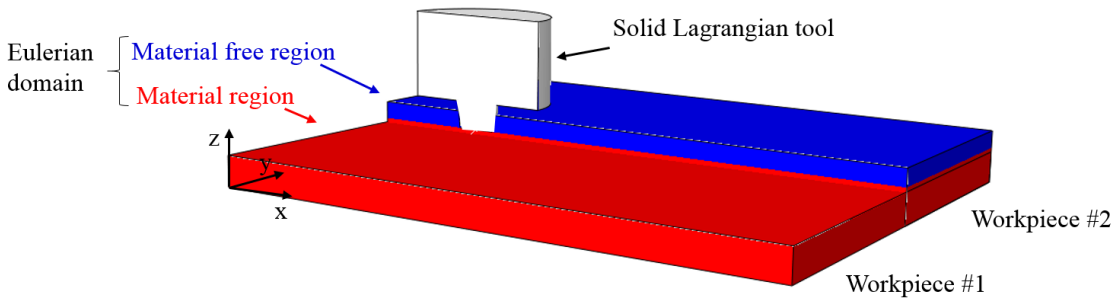

(a)

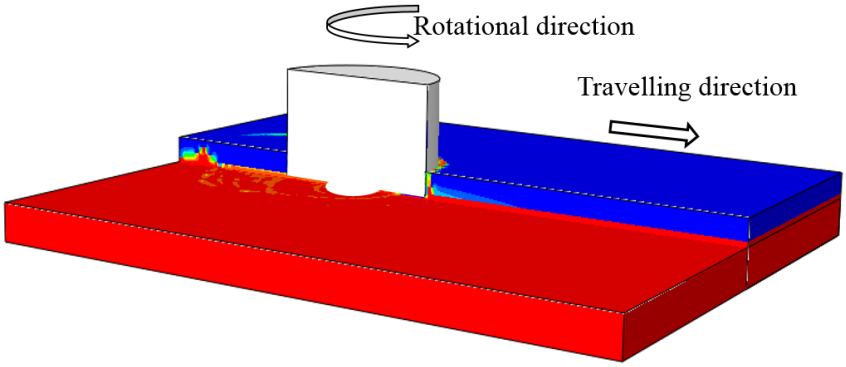

(b)

Figure 2.5 Problem setup in the Coupled-Eulerian-Lagrangian (CEL) finite element simulation for the FSW process: (a) initial configuration, (b) during the welding process.

Table 2.2 Constitutive parameters used in the Johnson-Cook model for AA6061-T6 [44].

A_{JK} (MPa)	B_{JK} (MPa)	C_{JK}	m_{JK}	N	T_{melt} (K)	T_{ref} (K)
324	114	0.002	1.34	0.42	297	856

Table 2.3 Thermomechanical properties for AA6061-T6 [44, 56].

Temperature (K)	Specific heat ($Jkg^{-1}K^{-1}$)	Young's modulus (GPa)	Poisson's ratio	Thermal conductivity ($Wm^{-1}K^{-1}$)	Thermal expansion (10^{-6} K^{-1})
298	945	66.94	0.33	162	23.5
373	978	63.21	0.334	177	24.6
422	1000	61.32	0.335	184	25.7
477	1030	56.8	0.336	192	26.6
533	1052	51.15	0.338	201	27.6
589	1080	47.17	0.36	207	28.5
644	1100	43.51	0.4	217	29.6
700	1130	28.77	0.41	229	30.7
755	1276	20.2	0.42	243	-

meshed with 128,089 EC3D8RT elements, in which the red part represents two workpieces (each with the dimension of 50 mm× 20 mm × 3mm) and the blue part is empty.

The Lagrangian body is coupled to the Eulerian domain through the contact interaction, using the Coulomb friction law as shown in Figure 2.1 (c). It should be mentioned that Figure 2.1 (c) and (b) are very different; CFD simulations based on Figure 2.1 (b) start with a pre-defined pressure, while finite element simulations based on Figure 2.1 (c) need to determine pressure and stick-slip condition by solving the boundary/initial value problem. In our CEL simulations, three different friction coefficients (μ_f =0.3, 0.5, 0.8) would be used to investigate their effects on thermomechanical field distributions and stick-slip conditions on tool-workpiece interface. Velocity constraints are applied on side surfaces and bottom surface of the Eulerian domain to avoid material escaping Figure 2.5. The whole simulation process includes three stages: plunging stage (0.2s), dwelling stage (0.2s) and welding stage (2.5s). The tool rotational speed is kept at 1000 rpm, and the welding speed is 3 mm/s.

2.4.2 CEL simulation results

Simulated temperature and velocity fields in the workpiece #2 during each FSW state with three different friction coefficients are illustrated in Figure 2.6 and Figure 2.7, respectively. Since the view cut is based on a fixed height in the initial configuration, one can actually see some part of workpiece #1 over that original height; these are morphological features not captured in CFD simulations. As these results show, temperature distributions at each stage are very similar in three cases. The highest temperature occurs near the shoulder-pin junction, and a larger friction coefficient will lead to a higher peak temperature. From the velocity contours at different welding stages, one can see that at plunging stage, most of the workpiece material underneath the tool follows the movement of the tool. When reaching to the dwelling stage, material near the outer edge of tool shoulder and pin lags behind, and the size of “sticking” zone shrinks. In comparison, simulations with a higher friction coefficient obtains a larger “sticking” zone size on the interface.

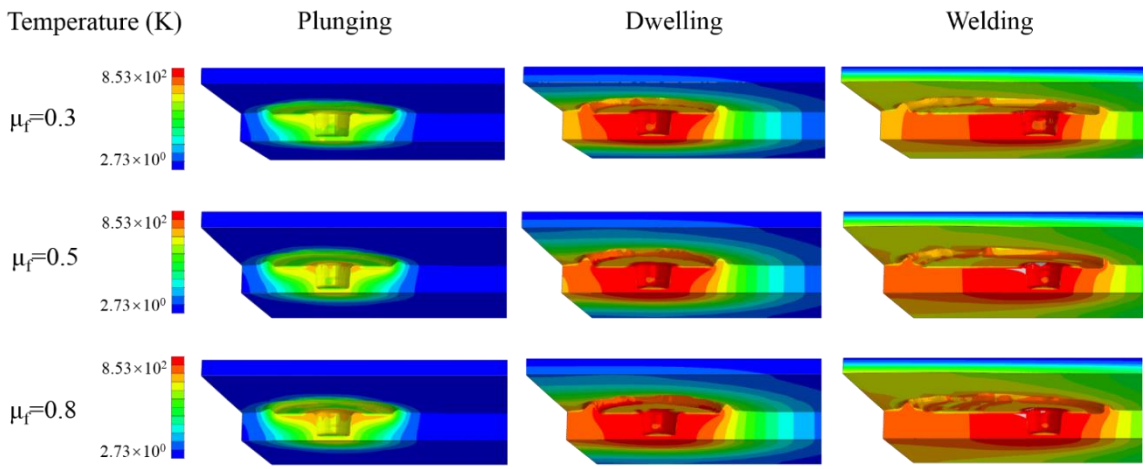

Figure 2.6 CEL simulation results showing the temperature fields in workpiece #2 during each FSW stage with three different friction coefficients. Refer to Figure for model setup.

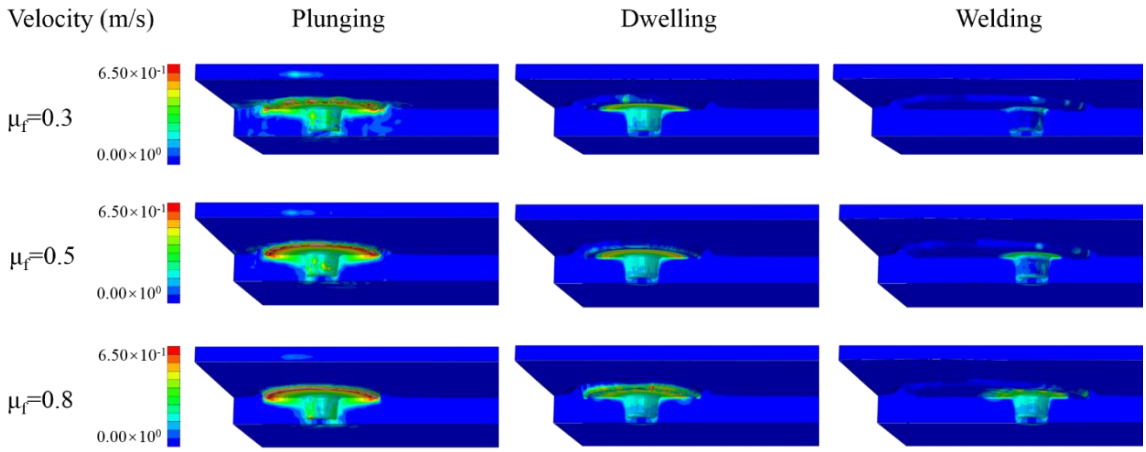

Figure 2.7 CEL simulation results showing the velocity field in workpiece #2 during each FSW stage with three different friction coefficients. Refer to Figure for model setup.

Now switching the view cut along the tool traveling direction in Figure 2.6 and Figure 2.7 (i.e., *xz* plane in Figure 2.5) to the lateral cross-sectional direction (i.e., *yz* plane in Figure 2.5), we plot the distributions of shear stress, pressure, velocity, and material flow stress for the workpiece materials right underneath the tool shoulder in Figure 2.8 and Figure 2.9. For μ_f =0.5 in Figure 2.8, the top row compares several stress measures. While the stick zone can be determined when the shear stress is less than $\mu_f p$, this method turns out to be inaccurate due to the mesh size limitation. Instead, the velocity differences in the bottom row in Figure 2.8 shows the inner stick zone and the outer annular sliding zone. The stick zone is the largest at the plunging state, and correspondingly, the shear stress at the tool-workpiece interface is larger than the workpiece flow stress. At the dwelling and welding stages, flow stress underneath the outer edge of shoulder becomes larger than the shear stress at interface, which narrows down in the sticking zone. Velocity distributions for three friction coefficients are compared in Figure 2.9, which clearly shows that a higher friction coefficient helps obtain a lager sticking zone.

2.5 Analytical stick-slip model based on Hill-Bower similarity analysis

CFD and CEL simulations in Sections 2.2 and 2.3 give rather very different predictions of thermomechanical responses. While the stick-slip ratio is more trustworthy in Section 2.3 than in Section 2.2, these results need to be validated from analytical and experimental results.

2.5.1 Hill-Bower similarity analysis for contact problems

In typical processing conditions, the traveling speed of the tool is much less than ωa, so that only pure torsion needs to be analyzed as in Figure 2.10(a). All simulation results in previous sections found the generated heat is transferred over a much larger size than the tool, so the deformation behavior of the workpiece underneath is effectively creep-dominated and elastic contributions can be neglected. Consequently, we are dealing with a circular torsional contact of a pure creeping solid in Figure 2.10(a).

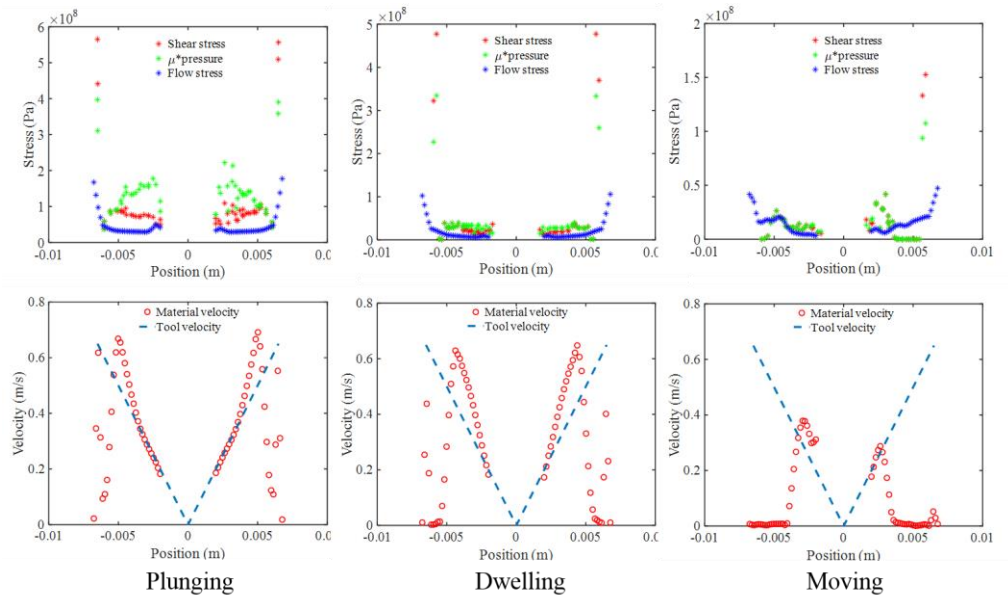

Figure 2.8 CEL simulation results showing the material flow stress (top row) and velocity (bottom row) of the workpieces right underneath the tool for μ_f =0.5. Positive location corresponds to the advancing side (workpiece #1), and negative location to the retreating side (workpiece #2).

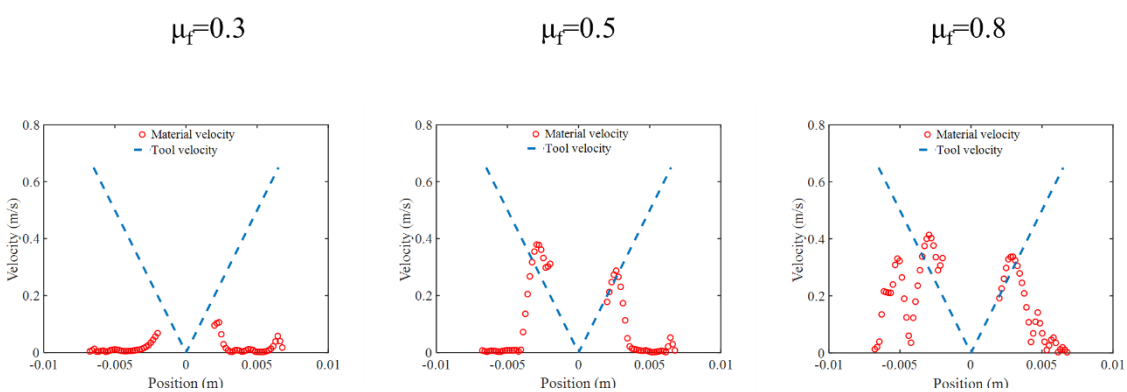

Figure 2.9 Steady-state distribution of workpiece velocity right underneath the tool, as calculated from CEL simulations in Figure , for three different friction coefficients.

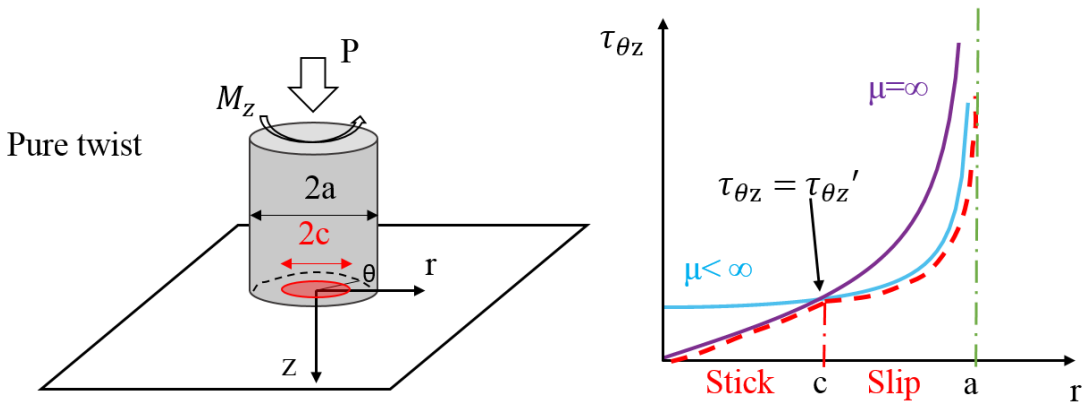

(a) (b)

Figure 2.10 (a) Schematic illustration of the stick-slip condition at the tool-workpiece interface. The boundary is circular when the lateral moving speed is much less than ωa. (b) Solutions of the interfacial shear stress.

Our contact analysis is based on the Hill-Bower similarity relationship [57-59]. At any particular instant, the strain rates and stresses in a pure creeping solid under contact are independent of the history of loading and depend only on the instantaneous velocities and contact radius prescribed on the surface. In terms of mathematical representation, consider a power-law creeping solid with

$$\frac{\sigma}{\sigma_0} = \left(\frac{\dot{\varepsilon}}{\dot{\varepsilon}_0} \right)^{1/n} \tag{2.12}$$

where σ_0 and $\dot{\varepsilon}_0$ are reference stress and reference strain rate, respectively, and n is the stress exponent as in Eq.(2.7). Regardless of the indenter shape (spherical, conical, or punch with a circular end), the effective strain rate is given by

$$\dot{\varepsilon}_{eff} = \frac{\dot{h}}{a} \tag{2.13}$$

with a being the contact radius and $\dot{h}$ being the rate of indentation depth. Therefore, the contact force P can be written as the following relationship,

$$\frac{P}{\pi a^2 \sigma_0} = \left(\frac{\dot{h}}{a\dot{\varepsilon}_0} \right)^{1/n} F_a\left(n, \mu_f\right) \tag{2.14}$$

with the dimensionless function F_a, and the strain rate fields are

$$\dot{\varepsilon}_{ij} = \dot{\varepsilon}_{eff} E_{ij}\left(x_k/a, n, \mu_f\right) \tag{2.15}$$

where E_{ij} are dimensionless functions as the characteristic fields.

Bower et al. made a further step by noting the analogy between the initial value problem of a pure creeping solid under punch contact and the boundary value problem of a nonlinear elastic solid under punch contact[58]. If replacing all the rate measures in the former by the non-rate ones (e.g., $\dot{\varepsilon}_{ij}$ by ε_{ij}), the governing equations for the former are identical to those for the latter. Therefore, the above dimensionless functions in Eqs.(2.15) and (2.16) can be numerically calculated by just finite element simulations with the nonlinear elastic law of $\sigma/\sigma_0 = \left(\varepsilon/\varepsilon_0\right)^{1/n}$.

We now use the above Hill-Bower similarity to attempt an analytical solution for our torsional contact problem in Figure 2.10 (a). Because the nonlinear elastic contact problem does not permit analytical solutions unless $n=1$ (i.e., linear elastic), we make the analogy between a Newtonian viscous fluid and a linear elastic solid. The former is governed by

$$\dot{\varepsilon}_{ij} = \frac{1}{2\eta} s_{ij} \tag{2.16}$$

with s_{ij} being the deviatoric stress tensor. This is merely a multiaxial generalization of Eq.(2.6). The latter is given by the generalized Hooke's law,

$$\varepsilon_{ij} = \frac{1+\nu}{E}\left(\sigma_{ij} - \frac{\nu}{1+\nu}\sigma_{kk}\delta_{ij}\right) \tag{2.17}$$

with E and ν being the Young's modulus and Poisson's ratio respectively, and δ_{ij} being the Kronecker delta. The contact solution of a Newtonian viscous material can be taken from the elastic contact solution, by replacing strain in the elastic solution by strain rate and by taking $\nu = 1/2$ due to incompressibility.

2.5.2 Analytical solution for the torsional contact problem

From the above subsection, it is now established that the torsional contact solution for a Newtonian viscous solid is analogous to the linear elastic problem. Due to rotational symmetry, the stick-slip boundary is circular, and the exact ratio of c/a can be derived below.

The contact pressure distribution is independent of frictional condition[60],

$$\sigma_{zz} = \frac{P}{2\pi a^2}\frac{1}{\sqrt{1-(r/a)^2}} \tag{2.18}$$

so that Coulomb friction stress that sets the upper bound of interface shear stress is

$$\tau'_{\theta z} = \frac{\mu_f P}{2\pi a^2}\frac{1}{\sqrt{1-(r/a)^2}} \tag{2.19}$$

For infinite friction ($\mu_f = \infty$), the shear stress distribution that generates a rotational displacement field of $u_\theta = r\theta$ is given by

$$\tau_{\theta z}\big|_{\mu=\infty} = \frac{3M^*}{4\pi a^3}\frac{r/a}{\sqrt{1-(r/a)^2}} \tag{2.20}$$

where the torque parameter M^* remains to be determined.

As shown in Figure 2.10(b), both Eqs. (2.20) and (2.21) have the same inverse square root singularity when $r \to a^-$, as the same singularity near a crack tip. The purple curve for Eq. (2.20) and the blue curve for Eq. (2.19) naturally intercepts at a location of $r = c$ by equating these two equations, so that $M^* = 2a^2\mu_f P/3c$. Taking the lower bound of these two solutions, the red dashed curve becomes the approximate solution of the shear stress,

$$\tau_{\theta z}\big|_{\mu<\infty} = \frac{\mu_f P}{2\pi a^2}\begin{cases} \dfrac{a}{c}\dfrac{r/a}{\sqrt{1-(r/a)^2}}, & r \le c: \text{stick} \\ \dfrac{1}{\sqrt{1-(r/a)^2}}, & c \le r \le a: \text{slip} \end{cases} \tag{2.21}$$

In other words, the twist stress needed to maintain a perfect bonding (as in infinite friction) is much larger than the upper bound value dictated by the Coulomb friction stress. Therefore, as the rotational angle increases, the slip zone emerges from the contact edge and progresses inward until the entire contacting surface is in sliding condition. Such an elastic solution mimics the stick-slip of a laterally sliding contact, in which the increase of lateral motion will lead to the emergence of annular slip zone and then the propagation towards the center of the contact corresponds to the onset of macroscopic sliding. This is well studied by the Mindlin-Cattaneo solution for Coulomb friction [60], or by some other variant solutions for different friction models [61, 62].

The solution analogy between the Newtonian viscous material and the Hookean solid can now lead to the following understanding. For elastic contacts, the rotation angle dictates the degree of stick-slip ratio of c/a. Due to the analogy, the rotation angle is now replaced by its rate, i.e., the rotation speed of ω. Therefore, for our creeping solid under

contact, it is ω that dictates the stick-slip behavior. In other words, given a set of processing parameters, there will be a steady state with a fixed c/a ratio.

The resulting torque on the tool can be calculated from $M_z = \int_0^a \tau_{\theta z}\big|_{\mu<\infty} 2\pi r dr$, which can be written as the following dimensionless function,

$$\frac{M_z}{\mu P a} = \Pi_M\left(c/a\right) \tag{2.22}$$

As given in Figure 2.11 (a), $\Pi_M\left(c/a\right)$ decreases from about 0.78 (from numerical quadrature) to 2/3 (analytical result) when c/a varies from 0 to 1.

The total heat generation rate can be computed from the above result and Eq.(2.5). For the simplified case of neglecting elasticity and assuming $\alpha_{TQ} = 1$, we have $Q_{total} = \omega M_z$. It should be noted that c/a depends on ω, so we need to introduce a characteristic rotation speed ω_0 for the following dimensionless function,

$$\frac{Q_{total}}{\mu P a \omega_0} = \frac{\omega}{\omega_0}\Pi_M\left(c/a\right) \tag{2.23}$$

More details on the dependence of c/a on ω will be provided in Chapter 4.

2.5.3 Comparisons to numerical simulations

As pointed out in Bower et al. [58], dimensionless functions such as F_a in Eq. (2.14) and E_{ij} in Eq. (2.15) are not so sensitive to n, unless $n \to \infty$. Therefore, it is anticipated that our approximate yet analytical solution may be used to validate the numerical simulation results.

Comparisons to CFD simulations are presented in Figure 2.11, for which we take the results by the empirical friction stress model in Figure 2.3(b) and Figure 2.4(b). In Figure 2.11(a), the blue dashed curve represents our analytical result in Eq.(2.22), plotted against the contact state (i.e., $1-c/a$). The left and right ends of the abscissa thus correspond to fully stick and fully slip conditions, respectively. Data processed from CFD simulations are represented by pink rhombus markers labeled with the corresponding ω value. As shown previously in Figure 2.3, increasing ω increases the stick-slip ratio of

c/a, and at the same time, both numerical simulations and our analytical model show the decrease of the resulting torque in Figure 2.11(a). Although the normalized torque, $M_z/\mu_f Pa$, does not vary significantly, its weak dependence on c/a is well captured here. The corresponding normalized heat generation rate is obtained through analytical solution and post-processing of CFD simulation results, as plotted in Figure 2.11(b). As the pink rhombus markers show, a higher rotation speed in numerical simulations results into a larger stick-slip ratio and a higher total heat generation rate, in almost perfect agreement with the predictions by our analytical model.

Comparisons to CEL simulation results in Figure 2.6-Figure 2.9 are presented in Figure 2.12. The tool rotation speed was fixed in these simulations, but three friction coefficients were adopted. For the normalized torque in Figure 2.12 (a), it can be seen that the increase of friction coefficient will increase the sticking zone size (clearly $c/a \to 1$ as $\mu_f \to \infty$), and at the same time, the normalized torque decreases as the analytical solution has predicted. For the normalized total heat generation rate in Figure 2.12 (b), a higher friction coefficient on the contact surface will lead to a larger stick-slip ratio of c/a and a much higher total heat generation rate, again in almost perfect agreement with our analytical predictions.

The above comparisons in Figure 2.11 and Figure 2.12 suggest that the two analytical results in Eqs. (2.23)and (2.24) provide successful rational analyses that relate $M_z/\mu_f Pa$ and $Q_{total}/\mu_f Pa\omega_0$ to the interfacial stick-slip ratio of c/a. CFD simulations are always based on ad hoc interface conditions (such as those in Figure 2.3(a) and (b)), and therefore they may not predict the same c/a (and thus the same corresponding torque and heat generation rate) as CEL simulations. Nevertheless, all simulation results collapse onto the same master curves of $M_z/\mu_f Pa \sim c/a$ and $Q_{total}/\mu_f Pa\omega_0 \sim c/a$, which provides an alternative way to tuning these simulation methodologies in addition to the common practice of fitting to medium- and far-range temperature fields.

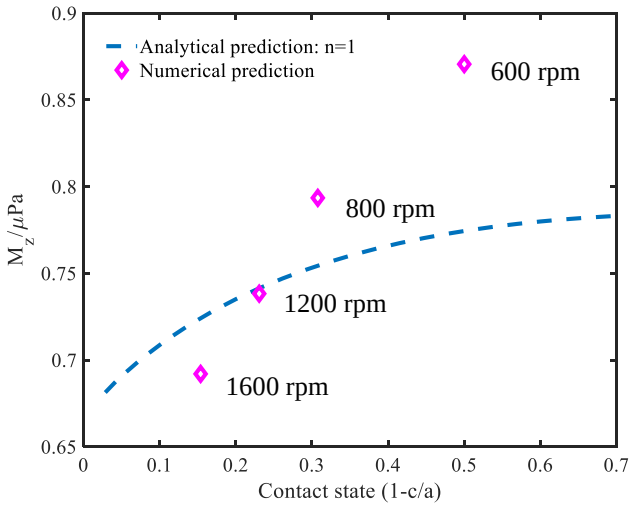

(a)

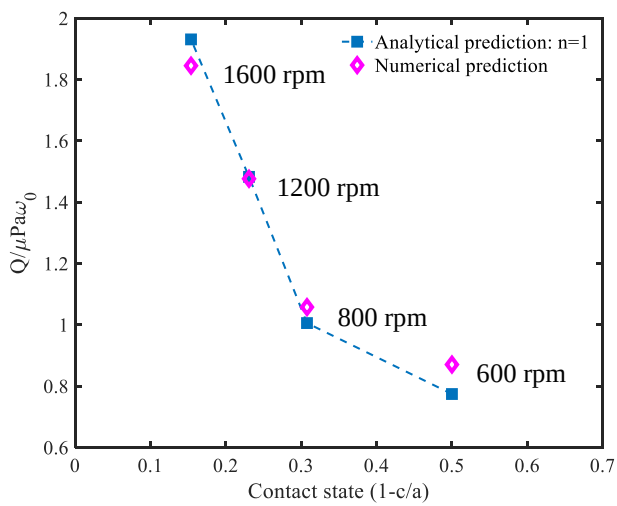

(b)

Figure 2.11 Analytical prediction of the normalized torque in (a) and the normalized heat generate rate in (b) as a function of the contact state (i.e., $1-c/a$), together with the CFD simulation results based on the empirical friction boundary condition in Figure 2.2(b). The parameter ω_0 is 600 rpm.

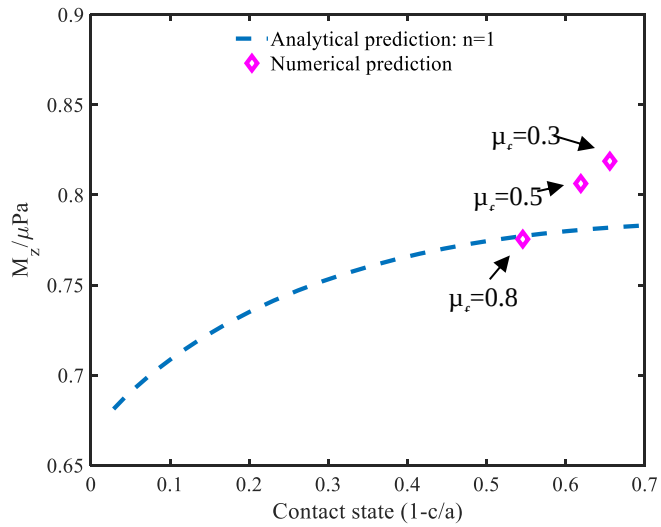

(a)

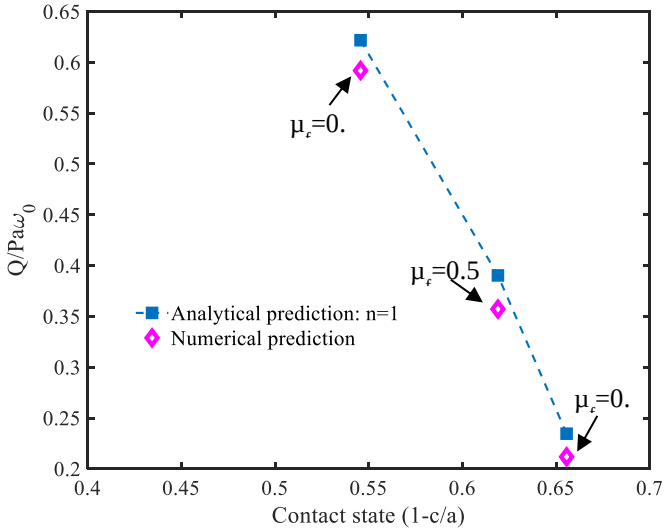

(b)

Figure 2.12 Analytical prediction of the normalized torque in (a) and the normalized heat generate rate in (b) as a function of the contact state (i.e., $1-c/a$), together with the CEL simulation results that correspond to results in Figure 2.6-Figure 2.9. The parameter ω_0 is 1000 rpm.

2.5.4 Comparisons to experimental measurements

As no experimental data have been reported on the stick-slip ratio, we can only attempt to compare to macroscopic thermomechanical responses, including the torque, total heat generation rate, peak temperature, and others.

Peel et al. have conducted extensive FSW tests on a number of aluminum alloys with a wide range of processing parameters [63]. Their torque and axial force data are compiled and processed to generate the normalized torque values, which are then compared to our analytical model and numerical simulations in Figure 2.13(a). Although their aluminum alloys are different from our AA2024, the dependence of $M_z/\mu_f Pa$ on ω/ω_0 shows the same trend, and the same range of variation, as our analytical solution and numerical data (from Figure 2.11(a)). Sato et al. obtained the relationship between tool rotational speed and peak temperature in FSW process for 6000 series aluminum alloy through experiments [64]. A rudimentary heat transfer analysis (to be presented in Chapter 4) shows that the temperature rise, $\Delta T = T_{peak} - T_{initial}$, is proportional to $Q_{total}/2\pi ka$. The experimental finding of increasing peak temperature with the increase of rotation speed agrees with our results in Figure 2.11(b). Roy et al. and Nandan et al complied literature experimental data according to two dimensionless parameters [3, 65], $T^* = T_p/T_{initial}$ with T_p being the final temperature, $Q^* = f\sigma_8 A_{shoulder}\omega C_P/kU^2$, where f is the heat transfer ratio between tool and workpiece, σ_8 is the yield stress, $A_{shoulder}$ is the cross-sectional area of tool shoulder, and U is the tool traveling speed. They have found a good curve fitting to the following representation,

$$T^* = 0.131 \ln Q^* + 0.196 \tag{2.24}$$

In Figure 2.13 (b), selected complied data in Roy et al. are plotted [65], overlaid with our results of the dependence of $Q_{total}/\mu_f Pa\omega_0$ on ω/ω_0. Because of different ways of normalizing the total heat generation rate, this plot should only be understood as showing the same qualitative trend, i.e., a significant increase of the heat generation rate with the increase of tool rotation speed.

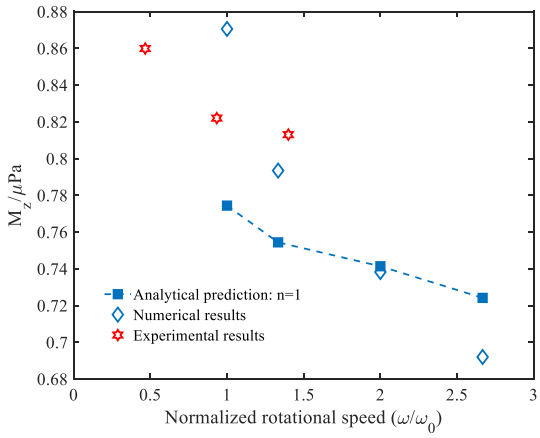

(a)

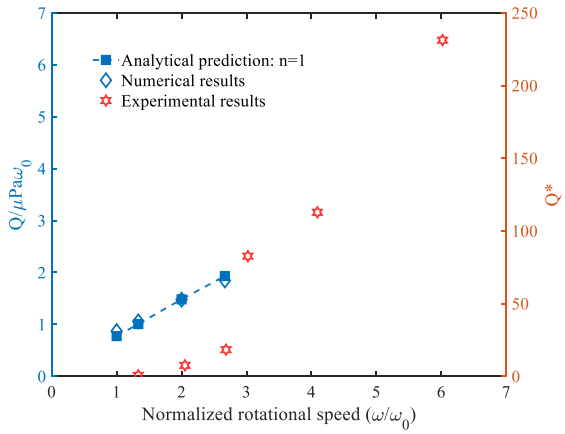

(b)

Figure 2.13 Comparisons among our analytical model, numerical simulations, and literature experimental data on: (a) the normalized torque (with experimental data compiled from Peel et al.[63]), and (b) the normalized total heat generation rate (with experimental data compiled from Roy et al.[65]). Numerical simulations are from Figure 2.12, so that ω_0 is 600 rpm.

2.6 Conclusions

This chapter shows that the FSW thermomechanical responses relate to the processing, geometric, and material constitutive parameters through the interfacial stick-slip ratio of c/a. Main findings are summarized below.

(1) For CFD-based models for FSW process simulation, we have implemented the pseudo-sticking-state model in Figure 2.1(a) and the empirical friction stress model in Figure 2.1 (b) for the interfacial condition into FLUENT. Although the stick-slip behavior can be produced in these models, their predicted c/a values are different and sensitive to their chosen parameters. Consequently, the resulting temperature and strain rate fields in workpiece materials are found to be sensitive to these ad hoc interface models, and correspondingly tedious parameter-fitting and iterative steps (particularly for avoiding predefining a uniform contact pressure) may be required for these CFD results to be predictive.

(2) CEL-based finite element simulations solve the contact problem under Coulomb friction, so that the computed thermomechanical fields are more reliable although computational cost and convergence issue are still the bottleneck concern.

(3) Based on the Hill-Bower similarity analysis for contact problem and the solution analogy between Newtonian viscous material and linear elastic solid, we have derived an approximate yet analytical solution, from which two dimensionless functions can be determined for $M_z/\mu_f Pa \sim c/a$ and $Q_{total}/\mu_f Pa\omega_0 \sim c/a$. These analytical predictions agree very well with the CFD and CEL simulations, and also show the same trends as in many experimental works.

(4) Our numerical and theoretical investigations of temperature and strain-rate fields provide the critical inputs for the bonding analysis. Particularly, the dimensional analysis for torque and total heat generation rate allows us to derive the dependence of bonding extent and fidelity on the processing, geometric, and material constitutive parameters, as will be detailed in Chapter 4.

3 Solid-state-bonding mechanism in friction stir welding

3.1 Introduction

From the viewpoint of materials processing, it has been found that strain rate, temperature, and stress fields are affected both by thermomechanical processing parameters in FSW such as the tool geometry, traveling speed, and rotation speed and by the properties of the joining materials. A multitude of experimental and numerical studies, including computational fluid dynamics (CFD) and finite element method (FEM), have been conducted to understand the characteristics of the thermomechanical fields [39, 66, 67]. A mechanistic understanding of the dependence of bonding evolution on processing parameters and materials behavior is of critical importance, which will eventually affect the structural integrity of the weldments. Studies along this line, however, remains elusive as explained below.

Even though both FSW and conventional diffusion bonding technologies are solid-state bonding in nature, it takes much shorter time in FSW to form the bonding at the interface. In conventional solid-state diffusion bonding processes, it is often understood that the interface free energy reduction as in the sintering process and the applied joining pressure drive the closure of gaps (e.g., from isolated adjourning domains, to meandering tunnels, and to discrete cavities with the increase of the degree of bonding), while the kinetics is governed by the interfacial mass transport at elevated temperatures[35, 68]. Thus it is found that pressure, temperature and bonding time are key factors that could affect the bonding fraction. On the other hand, time elapses rapidly in FSW processes so that the contribution of diffusional processes might be limited (as will be proved so in this chapter). Previous experimental studies conclude empirically that the degree of bonding tends to increase when the applied force/torque and the resulting temperature field are high, but does not change much with respect to the increase of the abutting force (i.e., the lateral force that holds the two workpieces together), which suggest the critical role of creep rather than diffusion on the bonding evolution. In the criterion developed in[69], a parameter that controls the final solid-state bonding was defined to depend on the pressure and the effective stress on the interface. A sound bonding is believed to be attached when this

parameter reaches a critical value. However, no clear mechanisms that control the bonding evolution are clarified in regard to the evolution of this parameter. Chen et al. [32] suggested that the interfacial bonding depends on the viscoplastic crushing of the surface asperities of the two workpieces. Such a model shines key insights on the bonding evolution, but it requires a knowledge of surface roughness, its applicable parametric space has not been given, and the stress triaxiality (i.e., the relative contribution of pressure and shear) is not included.

The unique view in this chapter is motivated by the deformation and failure mechanism maps in polycrystalline materials [70, 71]. Grain boundary diffusional processes are only important at low stress and high temperature, in contrast to the dislocation creep at high stress. The closure of the workpiece-workpiece gap field is a reverse process of intergranular fracture due to cavity growth; the latter may be determined by the interfacial diffusion in the classic Hull-Rimmer model [72], or by the creep-driven growth, or by their competition as governed by the Needleman-Rice length scale [73]. Consequently, a quantitative understanding of the solid-state bonding in FSW relies on a quantitative assessment of the temporal evolution of the stress, strain rate, and temperature fields on the workpiece-workpiece interface, and thus the rigorous determination of the competing roles of interfacial diffusion and creep in the surrounding workpieces. In this chapter, we will first report our simulated transient temperature, stress, and strain rate fields in FSW by using the Coupled Eulerian-Lagrangian (CEL) finite element method in the commercial software, ABAQUS. The thermomechanical histories of four representative reference points on the interface are compared to both the deformation mechanism map and the contour plots of the Needleman-Rice length, which upholds that creep-dominated cavity closure be the solid-state bonding mechanism. A quantitative prediction of the bonding fraction will be presented for these four reference points, and implications on FSW processing parameters and materials parameters will be discussed.

3.2 Friction stir welding processing modeling

3.2.1 Friction stir welding simulation through CEL

As shown in Figure 3.1, the finite element setup using the CEL method includes the sample domain (only the workpiece on the retreating side of the tool is shown here) and the "empty" domain (not shown for clarity; for heat transfer analysis only). It should be noted that the commonly used CFD simulations for FSW face difficulties in modeling the tool-workpiece frictional behavior since pressure has to be specified a priori (such as through the user-defined function in a commercial CFD software, FLUENT). How and what kind of interface boundary condition is applied will significantly change the final simulation results. FEM simulations avoid this problem by directly simulating the Coulomb friction, but the severe plastic deformation cannot be handled in the standard Lagrangian approach, which can be resolved by the CEL approach. The CEL approach divides the entire control volume into Eulerian and Lagrangian domains, thus overcoming the difficulty in frictional modeling in CFD and the difficulty in large deformation in computational solid mechanics. In Figure 3.1, since our objective is devoted to the bonding analysis, for the sake of simplicity, the rotating tool is modeled without pin. The entire FSW process includes plunging, dwelling, and welding, for which the spin rate and welding speed are 1000 rpm and 2 mm/s, respectively. We choose four reference points (A-D in Figure 3.1) on the workpiece-workpiece interface, with the corresponding times when the tool reaches them correspondingly. A steady state obviously is reached upon arriving at Point C.

Considering the extremely high stress and temperature, the power-law creep breaks down, and the hyperbolic sine law is used [11],

$$\dot{\varepsilon}_{creep} = A_n \left[\sinh\left(\frac{\sigma_e}{\sigma_{ref}} \right) \right]^n \exp\left(-\frac{Q}{RT} \right) \tag{3.1}$$

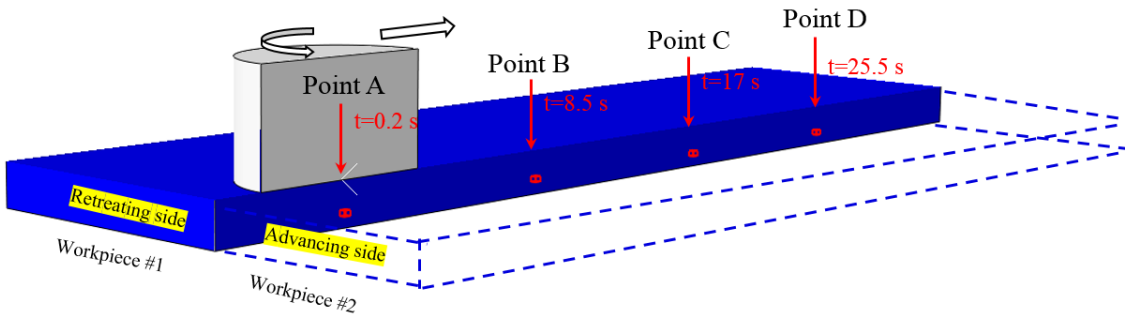

Figure 3.1 Finite element setup using the coupled Eulerian-Lagrangian (CEL) approach in the friction stir welding (FSW) process.

where σ_e is the effective Mises stress, σ_{ref} is the reference stress, A_n is a pre-factor, n is the stress exponent, Q is the activation energy for dislocation creep, R is the gas constant, and T is the absolute temperature. The material of interest is precipitate-strengthened aluminum alloy, Al6061-T6, and the corresponding material parameters include: $A_n = 2.41 \times 10^8 s^{-1}$, n=3.55, σ_{ref}=22.22 MPa, Q=145 kJ/mol, and T_m=856 K [16,17].

3.2.2 Thermal and mechanical variables distribution

Representative results given in Figure 3.2 are for strain rate, temperature, and Mises stress fields when the tool arrives Points A, B, and D, respectively. The temperature field extends to a much wider regime than the strain rate and stress fields.

The thermomechanical histories of these four traced positions are given in the deformation mechanism map in Figure 3.3 (a). The background contours are for the strain rate by the dislocation creep law in Eq. (3.1). The trajectories for all four points, except the early stage of that of Point A, almost collapse onto one another. The stress rises up to high flow strength at low temperature, and then heating from both tool-workpiece friction and plastic deformation leads to the increase of temperature and the corresponding stress decrease due to thermal softening. Even after the tool passes these reference points, the temperature still remains high (as can be seen from the second row in Figure 3.2, but the stress drops rapidly due to the departure of the spinning tool. The boundaries between dislocation creep in Eq. (3.1) and Coble creep that arises from grain boundary diffusion are also shown in Figure 3.3 (a) for grain sizes of 10 and 100 μm. Can we now conclude that diffusional processes do not contribute noticeably to the bonding process? This answer is no, since the interfacial cavity closure is governed by the competition by interfacial diffusion and creep in the surrounding materials, which can only be determined from the Needleman-Rice length scale in Figure 3.3 (b).

We should also point out that these trajectories are universal for other materials as well, because the thermal softening will eventually slow down the heat generation rate by plastic flow, and thus these trajectories plummet at the final stage.

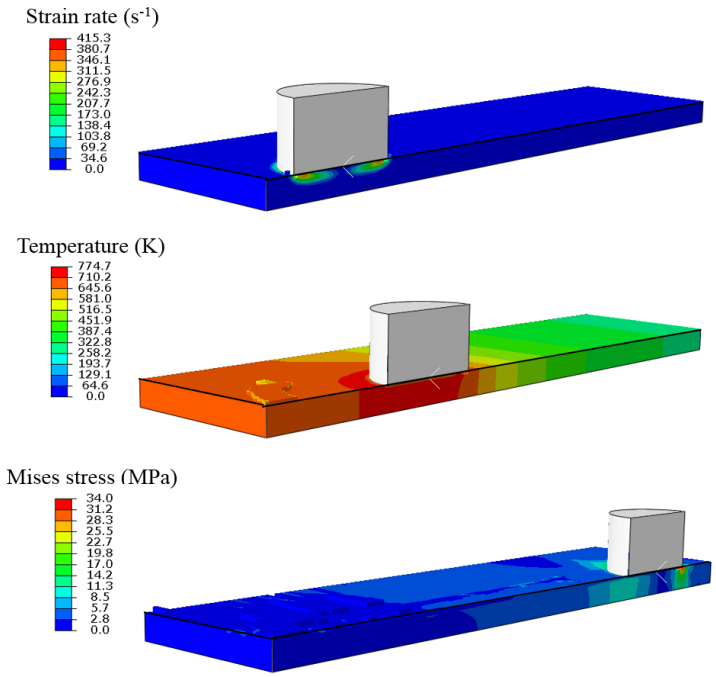

Figure 3.2 Representative results of the strain rate, temperature, and Mises stress fields are given with their corresponding tool locations, where the graininess on the workpiece surface results from plastic flow.

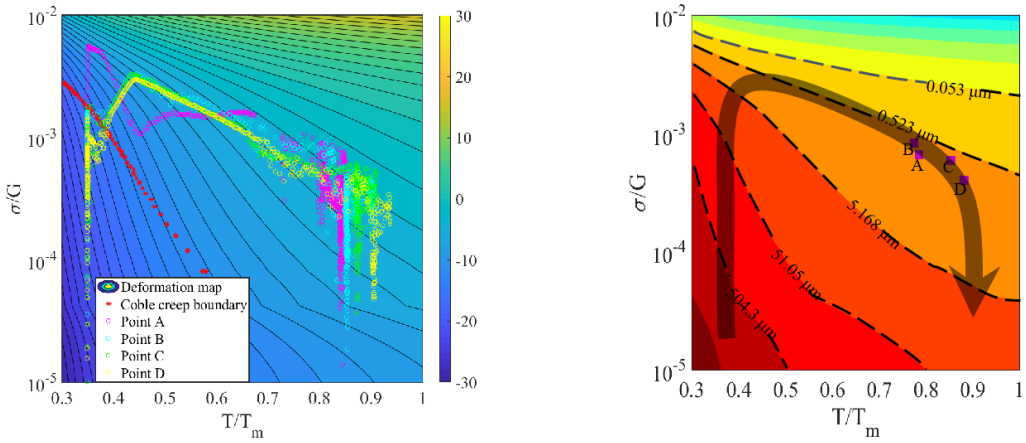

Figure 3.3 (a) Thermomechanical histories of the four reference points are plotted on top of the deformation mechanism map of Al6061-T6 alloy. These histories are located in the dislocation creep regime. (b) Contour plot of the Needleman-Rice length scale, L_{NR}, with respect to the normalized stress and the homologous temperature. The thermomechanical histories are schematically overlaid on this plot. The discrete squares indicate the occurrence of full bonding for the four reference points.

3.3 Cavity closure as the bonding process

A unit process during the interfacial bonding is the shrinkage of the interfacial cavities in Figure 3.4, which is the reverse process of the cavity growth in high temperature fracture. These cavities are lens-like because of the surface tension balance at the high temperature. The bonding fraction is given by $f_b = 1 - f_h$, where $f_h = (a/b)^2$ is the area fraction of these cavities/holes, and a and b are cavity size and cavity spacing, respectively. Based on a modification by Cocks and Ashby [18] to the classic Hull-Rimmer model, the evolution of interfacial cavity is

$$\frac{df_b}{dt} = -\frac{2(1-f_b)}{a^3 \ln\left[\frac{1}{(1-f_b)}\right]} \cdot \frac{D_B \delta_B \Omega}{k_b T} \cdot \sigma_n = -\frac{2(1-f_b)}{\ln\left[\frac{1}{(1-f_b)}\right]} \dot{\varepsilon}_{creep}^{eff} \left(\frac{\sigma_n}{\sigma_e}\right)\left(\frac{L_{NR}}{a}\right)^3 \tag{3.2}$$

where D_B is the interfacial diffusion coefficient, δ_B is the interface boundary thickness (usually several atomic sizes), Ω is atomic volume, and k_b is the Boltzmann's constant. The combination of diffusivity and $k_b T$ arises from the Nernst-Einstein relationship. When the applied normal stress is tensile/compressive, the bonding fraction decreases/increases accordingly. The conversion to the use of the effective creep rate, $\dot{\varepsilon}_{creep}^{eff}$, and the Needleman-Rice length, L_{NR}, will be discussed shortly.

The cavity can growth or shrink when there is a creep deformation in the surrounding material. Under the multiaxial stress state, extensive numerical simulation results by Sham and Needleman [74] can be fitted to

$$\frac{1}{f_b} \cdot \frac{df_b}{dt} = -(1-f_b)\dot{\varepsilon}_{creep}^{eff} \cdot C_{coeff}$$

$$C_{coeff} = \begin{cases} \left[\alpha_n \left|\frac{\sigma_m}{\sigma_e}\right| + \beta_n\right]^n \operatorname{sgn}\left(\frac{\sigma_m}{\sigma_e}\right), & \left|\frac{\sigma_m}{\sigma_e}\right| > 1 \\ \left[\alpha_n + \beta_n\right]^n \frac{\sigma_m}{\sigma_e}, & \left|\frac{\sigma_m}{\sigma_e}\right| \le 1 \end{cases} \tag{3.3}$$

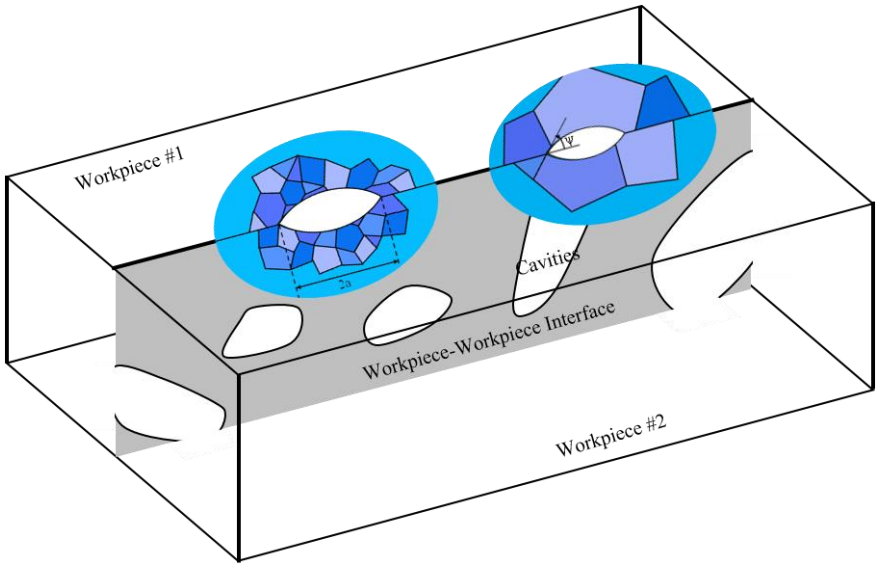

Figure 3.4 Schematic illustrations of bonded and unbonded regimes on the workpiece-workpiece interface. Cavities tend to be lens like because of the balance of surface tensions, but they may coalescence into meandering stripes at a low degree of bonding.

where dimensional parameters are $\alpha_n = \frac{3}{2n}$ and $\beta_n = \frac{(n-1)(n+0.4319)}{n^2}$, sgn() is the sign function, and σ_m is the mean stress. We have added a multiplicative factor of $\frac{1}{f_b}$ to the left hand side of Eq. (3.3), without which the original Sham-Needleman equation only works when f_b is larger than a critical value (e.g., 0.4). The comparison between the diffusional and creep processes in Eqs. (3.2) and (3.3) defines the Needleman-Rice length scale,

$$L_{NR} = \left[\frac{D_B \delta_B \Omega}{k_B T} \frac{\sigma_e}{\dot{\varepsilon}_{creep}^{eff}} \right]^{\frac{1}{3}} \tag{3.4}$$

This can also be viewed as a kinematic constraint, that is, if the interfacial diffusion is not divergence free, the surrounding materials must creep to ensure continuity.

Contours of L_{NR} are given in Figure 3.3(b) for our aluminum alloy. When L_{NR} is larger than cavity size, the cavity closure is governed by interfacial diffusion. A small L_{NR} corresponds to the creep dominant closure of cavities, as shown by the term of $\left(\frac{L_{NR}}{a}\right)^3$ in Eq. (3.2). The stress-temperature trajectories in Figure 3.3(a), if plotted on top of Figure 3.3(b), will indicate that our reference point will only enter the large-L_{NR} regime when the tool passes it (i.e., temperature still remaining high but stress decreasing dramatically).

Thermomechanical history data for these four reference points are used as inputs to Eq. (3.3), which is then integrated implicitly to predict the evolution of f_b. Two initial values are chosen, with $f_b|_{t=0} = 0.8$ representing finely polished workpieces and 0.01 for rough surfaces. Such a choice helps avoid the need to conduct experimental characterization of interface morphology. As shown in Figure 3.5, along with the movement of the tool, the area fraction of cavities, f_h, remains almost unchanged until the reference point falls into the thermomechanical process zone. Referring back to Figure 3.2, one can see that although the temperature field extends to a much larger zone, the strain

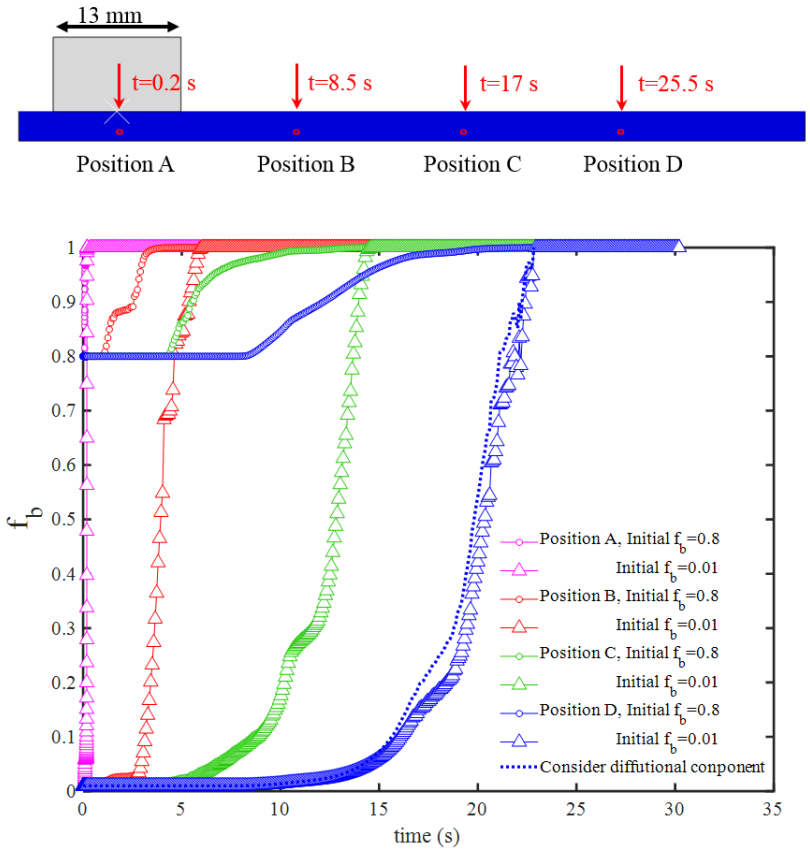

Figure 3.5 The evolution of f_b (i.e., the area fraction of bonding and no cavities) for the four reference points, with two initial values representing smooth and rough workpiece-workpiece interface.

rate field is rather narrowly localized near the tool. The evolution of f_b is directly governed by $\dot{\varepsilon}_{creep}^{eff}$, but not by T. Before the tool moves right to the top of the reference point, f_b rapidly increases to unity even with a very small $f_b|_{t=0}$, indicating that a full degree of bonding can be achieved mainly by creep before the reference point falls into the wake of the tool. An additional calculation is presented by the dashed line in which Eq. (3.2) is added onto the evolution of f_b. Before a full bonding is reached, both the temperature and stress at this reference point D are high, corresponding to the regime in Figure 3.3 (b) with L_{NR} being around several microns. Even with the choice of a=1 μm, the diffusion-driven reduction of f_b has little contribution to the overall evolution.

The generality of our model can also be confirmed from the discrete squares in Figure 3.3(b), which indicate the occurrence of full bonding for these four reference points. The Needleman-Rice contour plots are quite universal with respect to the normalized stress and temperature, as this length in Eq. (3.4) is primarily dictated by the stress exponent and the difference between the creep activation energy in Eq. (3.1) and the diffusion activation energy of D_B in Eq. (3.2). During the friction stir welding, the temperature rise softens the material and thus decreases the heat generation rate by plastic flow, and then the temperature rise slows down, which naturally leads to the universal trajectory in Figure 3.3(b). Full bonding occurs at locations with very low Needleman-Rice length values, so that diffusional bonding plays a secondary role as compared to creep-induced cavity closure.

3.4 Conclusions

In summary, from the simulated thermomechanical histories of a number of reference points on the workpiece-workpiece interface, we find out the interface traverses in regimes with very low L_{NR}, thus indicating the dominance of creep-controlled cavity closure. The evolution rate of the interfacial bonding depends primarily on the creep strain rate in the surrounding workpieces abutting at the interface, but not on the far-reaching temperature field. This study helps reveal design strategies in promoting the solid-state

bonding in FSW by entering and staying in the creep-dominant interfacial cavity closure through tuning materials constitutive parameters, thermomechanical processing parameters, and geometric shape factors.

4 Analytical and computational mechanics modeling of the solid-state bonding

4.1 Introduction

In this chapter, we propose a novel view on the solid-state bonding by treating the bonding process as a reverse one to the intergranular fracture in polycrystalline materials. The latter has been well understood in a vast number of literature [70, 71, 75-78]. At moderate temperature and stress, the dominant mechanisms include diffusive and creep-driven growth of grain boundary cavities, and these solutions can be used with some modifications for our cavity shrinkage problem. This viewpoint has many noteworthy differences from the conventional solid-state-bonding models. First, the mere consideration of interface energy reduction for the diffusive shrinkage of cavities is insufficient. The applied stress field biases the chemical potential [72], and thus drives the self-diffusion as described onto the third cavity in Figure 4.1(c). Compression increases chemical potential while tension decreases it, and the resulting diffusion is along the bonded interface, as opposed to the widely accepted model of volumetric inter-diffusion in the direction normal to the interface. Second, creep deformation of the surrounding workpiece materials also contributes to the volume change of the cavity, as shown schematically by the first cavity in Figure 4.1 (c). The competition between interface diffusion and bulk creep determines a length scale [73]. If this Needleman-Rice length is larger than the cavity size, then the cavity growth/shrinkage is governed by diffusive process; the opposite limit corresponds to the creep dominant behavior. Consequently, a complete understanding of bonding mechanisms requires a thorough knowledge of the applied thermomechanical trajectories for this Needleman-Rice-type analysis. For our FSW process, this has been accomplished in Chapter 3. Third, as individual cavities are subjected to different thermomechanical loading histories, it is not amenable to track all these cavities in a discrete manner. As shown in Figure 4.1 (c), we can homogenize these cavities and design an order parameter field as proposed by Tvergaard [76]. All the above details needed for the establishment of our bonding model will be elaborated in Section 4.2.

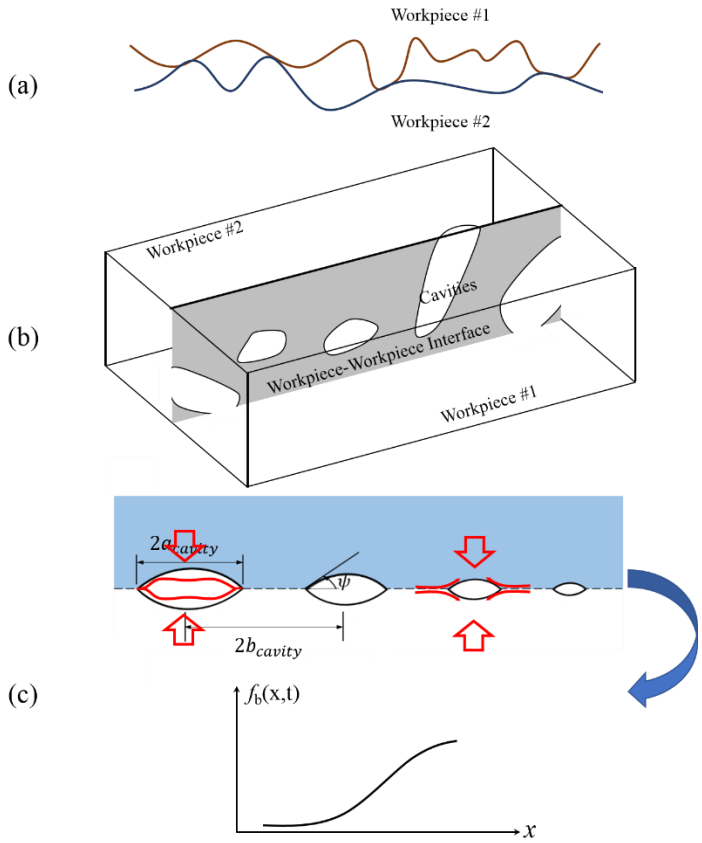

Figure 4.1 Schematic illustration of various solid-state-bonding models. (a) Rough surface contact between two workpieces is usually supported by isolated and widely separated asperities. (b) Bonding two workpieces is equivalent to the shrinkage and closure of interfacial cavities. (c) A discrete array of cavities, which can be closed by creep-controlled or diffusive processes, is homogenized into a field of bonding fraction, $f_b\left(x_\alpha, t\right)$.

For the FSW process, most literature studies on the effects of operation parameters on final bonding quality of the end products are mainly experimental and empirical. The most widely investigated parameters include the tool rotational speed, welding speed, and axial force. It has been found that the increase in rotational speed is favorable for enhancing joint strength [79-81]. Shen et al. [82] found that a higher penetration depth over a wide range of traveling speeds helps increase the weld strength. For the tool geometry, Boz and Kurt [83] and Zhao et al.[84] found that an improved bonding performance could be obtained using screw-pitched and tapered sir pin. However, numerical and analytical investigations on how these operation parameters affect the final bonding condition at interface is still limited. In Chapter 2, the relationship between these fields and the processing, geometric, material constitutive parameters has been thoroughly investigated, and an analytical solution based on the interfacial stick-slip behavior has been proposed and the predicted torque and total heat generation rate agree well with the numerical simulations. Because our bonding model in Section 4.2 depends directly on the temperature, strain rate, and stress fields and their histories, numerical simulation results of the FSW process will be directly used to predict the evolution of workpiece-workpiece bonding fraction with respect to varying input parameters, as will be presented in Section 4.3.

With so many controlling parameters involved in the FSW process, a better strategy that can find great applications in realistic problems will be the development of an analytical solution to predict the ultimate bonding extent. In Chapter 2, an analytical solution has been derived to determine the dependence of torque and total heat generation rate on the interfacial stick-slip condition, which can be further extended to find the full strain-rate and temperature fields. Combining these results with our findings in Sections 4.2 and 4.3, a flow chart of successive steps is proposed to first use the input processing, geometric, and material constitutive parameters to determine the peak temperature and the stick-slip ratio, and then to use the resulting strain-rate field to determine the extent of full bonding, as will be explained in details in Section 4.4. When comparing the prediction from this analytical approach to the numerical simulation results in Section 4.3, we can identify the most critical input parameters, together with their ranges to which the final

bonding extent is sensitive. These comparisons will be made for both FSW and friction stir cladding problem. A process window can be established from the finding that the bonding extent changes rapidly when traversing in the map of major processing parameters, as will be discussed in Section 4.5.

4.2 The solid-state bonding model

Referring to the processes in Figure 4.1(c), we will first discuss the behavior of individual cavities under various closure mechanisms (top figure), and then formulate the homogenized model that can be readily used with finite element simulations (bottom figure).

The interfacial cavities are of the lenticular shape, and the half dihedral angle is determined from the Young-Dupré equation,

$$\cos\psi = \frac{\gamma_{interface}}{2\gamma_{cavity}} < 1 \tag{4.1}$$

where $\gamma_{interface}$ is the workpiece-workpiece interface energy per unit area, and γ_{cavity} is the cavity surface energy per unit area. The Laplace pressure inside the cavity modifies its chemical potential by

$$\Delta\mu_{cavity} = -\Omega\sigma_{sintering} = -\Omega\frac{2\gamma_{cavity} - \gamma_{interface}}{R} \tag{4.2}$$

where Ω is the atomic volume of the (self) diffusing species, $\sigma_{sintering}$ (positive according to Eq. (4.1) is the sintering stress, and R is the radius of the spherical cap which relates to the cavity half size of a_{cavity} by $a_{cavity} = R\sin\psi$. Now, as $\Delta\mu_{\text{interface}} = 0$, we have $\Delta\mu = \Delta\mu_{cavity} - \Delta\mu_{interface}$ <0, and thus self-diffusion will be directed from the bonded interface to the cavity surface and close the cavity accordingly.

When an arbitrary stress field is applied from faraway, the bonded segment is now stressed, so that the chemical potential change is therefore $\Delta\mu_{interface} = -\Omega\sigma_n$. If neglecting the Laplace pressure in Eq. (4.2), an applied tensile stress will reduce the chemical potential

at the bonded interface, thus leading to the self-diffusion from cavity to the interface and to the cavity growth. This is the classic Hull-Rimmer model [72]. Combining the Laplace pressure and the applied stress, we have

$$\Delta\mu = \Delta\mu_{cavity} - \Delta\mu_{interface} = \Omega\left(\sigma_n - \sigma_{sintering}\right) \tag{4.3}$$

If the applied tensile stress is larger (or lower) than the sintering stress, cavity grows (or shrinks). A more rigorous analysis for the Hull-Rimmer model should consider the chemomechanical equilibrium over the entire interface/surface, as solved by Chuang and Rice [85] and Chuang et al. [86], which will be used later in this section for our bonding fraction evolution equation. In our solid-state-bonding problem, σ_n is negative, so that the diffusion flux is always directed towards the cavity as depicted in Figure 4.1(c). This is the diffusive process for cavity closure.

The other process for cavity growth/shrinkage is the creep deformation in Figure 4.1 (c). No analytical solution can be found in general, except for the Newtonian viscous solid for it is analogous to the elasticity problem when making the replacement of strain rates by strains. Just from a simple dimensional argument, one can see that the magnitude of the volume growth rate will be proportional to the effective creep strain rate in the surrounding material, with its sign governed by the mean stress. But the detailed dependence on the creep stress exponent and stress multiaxiality has to be determined from finite element simulations, as performed extensively by Needleman and Rice [73] and Sham and Needleman [74]. Their solutions can be used to establish curve-fitting equations for our bonding fraction evolution equation, as will be shown shortly below.

In the homogenization model by Tvergaard [76], a square array of cavities with size a_{cavity} and spacing b_{cavity} extends over the entire interface, so that we can define the degree of bonding by

$$f_b = 1 - \frac{a_{cavity}^2}{b_{cavity}^2} \tag{4.4}$$

Therefore, our bonding model will be based on the spatiotemporal evolution of the bonding fraction field, $f_b\left(x_\alpha, t\right)$, where x_α are the two coordinates spanning the interface.

For the diffusive process, we take a slight modification from the solutions presented earlier [75, 76, 85, 86], given by

$$\frac{df_b}{dt} = -\frac{2\left(1-f_b\right)}{a_{cavity}^3 \ln\left[1/\left(1-f_b\right)\right]}\left(\sigma_n - f_b\sigma_{sintering}\right)\frac{D_B\delta_B\Omega}{k_B T} \tag{4.5}$$

where D_B is the interfacial diffusion coefficient, δ_B is the interface boundary thickness of several atomic sizes, k_B is the Boltzmann constant, and T is the absolute temperature. The factor of $1-f_b$ in the numerator at the right hand side is introduced merely to regularize the divergence problem at $f_b \to 1$.

For the creep-controlled process, the solution of Sham and Needleman [74] is modified slightly to

$$\frac{1}{f_b}\frac{df_b}{dt} = -\left(1-f_b\right)\dot{\varepsilon}_{creep}^{eff} \times \begin{cases} \left[\alpha_n\left|\frac{\sigma_m}{\sigma_e}\right| + \beta_n\right]^n \operatorname{sgn}\left(\frac{\sigma_m}{\sigma_e}\right), & if \left|\frac{\sigma_m}{\sigma_e}\right| > 1 \\ \left[\alpha_n + \beta_n\right]^n \frac{\sigma_m}{\sigma_e}, & if \left|\frac{\sigma_m}{\sigma_e}\right| \le 1 \end{cases} \tag{4.6}$$

where two dimensionless parameters are introduced for curve fitting to finite element simulations, $\alpha_n = \frac{3}{2n}$ and $\beta_n = \frac{(n-1)(n+0.4319)}{n^2}$, n is the stress exponent in a power-law creep constitutive law, $\operatorname{sgn}(\ )$ is the sign function, $\dot{\varepsilon}_{creep}^{eff}$ is the effective creep rate (J_2 component, positive definite), σ_m is the mean stress, and σ_e is the Mises stress. Whether the cavity grows or shrinks depends on if $\sigma_m > 0$ or $\sigma_m < 0$. We have added a

multiplicative factor of $1/f_b$ to the left hand side of Eq.(4.6), without which the original Sham-Needleman equation only works when f_b is larger than a critical value (e.g., 0.4).

In realistic FSW conditions, the sintering stress can be neglected as it is usually too low (e.g., a few MPa) as compared to the applied stress. We can now rewrite Eq. (4.5) in a similar way to Eq.(4.6), given by

$$\frac{df_b}{dt} = -\frac{2(1-f_b)}{\ln\left[1/(1-f_b)\right]}\dot{\varepsilon}_{creep}^{eff}\left(\frac{\sigma_n}{\sigma_e}\right)\left(\frac{L_{NR}}{a_{cavity}}\right)^3 \tag{4.7}$$

where L_{NR} is the Needleman-Rice length scale,

$$L_{NR} = \left[\frac{D_B\delta_B\Omega}{k_BT}\cdot\frac{\sigma_e}{\dot{\varepsilon}_{creep}^{eff}}\right]^{1/3} \tag{4.8}$$

Neglecting a weak dependence on f_b and stress triaxiality, we have the following

$$\frac{(df_b/dt)_{diffusive}}{(df_b/dt)_{creep}} \propto \left(\frac{L_{NR}}{a_{cavity}}\right)^3 \tag{4.9}$$

from the comparison between the diffusive and creep-controlled processes. It should be noted that D_B has an Arrhenius dependence on temperature, and so is the creep rate. But their corresponding activation energies are very different, leading to a representative L_{NR} contour plot in Figure 4.2(a) for AA6061-T6, with the constitutive parameters given in Table 4.1 and the diffusion parameters from Frost and Ashby [87]. Overlaid on Figure 4.2 are the thermomechanical histories of several representative points on the workpiece-workpiece interface during FSW, as will be discussed later in the next section. Moving towards higher stress and temperature, L_{NR} decreases dramatically, so that the relative significance from diffusive process drops sharply according to Eq.(4.9). Our preliminary calculations in Chapter 3 [8] uses a small a_{cavity} of 1 μm, which already finds little difference between the creep-controlled bonding evolution and the one governed by both

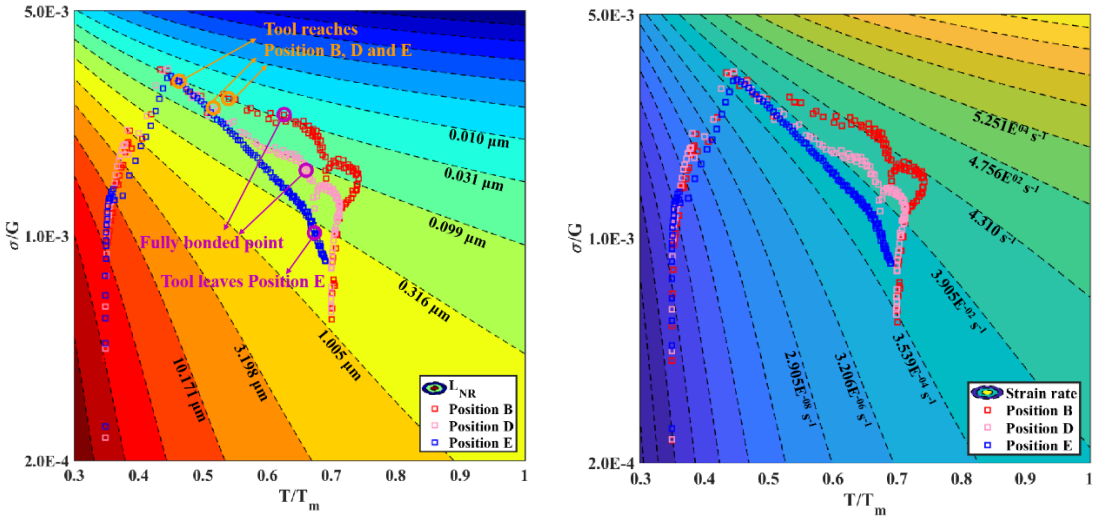

(a) (b)

Figure 4.2 (a) The contour plot of the Needleman-Rice length scale, L_{NR}, with respect to the homologous temperature and normalized stress, which dictates the relative significance of diffusive and creep-controlled processes for cavity closure. (b) The corresponding contour plot of strain rates for AA6061-T6 aluminum alloy. Overlaid on these plots are the thermomechanical histories of three reference points (B, D, and E) from Figure 4.3(b). The orange markers denote the instant of tool front reaching these points, and the purple ones denote the condition of reaching full bonding for B and D and the condition of tool leaving point E.

Table 4.1 Constitutive parameters used in our CEL simulations of AA6061-T6 [88, 89].

A_n (s^{-1})	σ_{ref} (MPa)	n	Q (kJ/mol)
2.41×10^{8}	22.22	3.55	145

processes.

4.3 Bonding prediction from CEL-based numerical simulations

4.3.1 Model setup

The coupled-Eulerian-Lagrangian (CEL) finite element simulations were performed to compute the strain rate and temperature fields under the FSW process. Essential details on this approach, and its comparison to Computational-Fluid-Dynamics (CFD) simulations, have been presented in Chapter 2. As shown by the three-dimensional (3D) CEL model using Abaqus Explicit in Figure 4.3, the Eulerian part has a dimension of 40 mm×30 mm×14.5 mm, including the workpiece domain (thickness of 13 mm) and the "void" domain (thickness of 1.5 mm), with a total of 85,760 EC3D8RT elements. The tool is modeled as a Lagrangian body with a circular bottom of radius a=6.5 mm and without the pin for the sake of simplicity. Velocity constraints are applied at model boundaries to avoid material escaping, while the connection between Lagrangian and Eulerian domains is through the Coulomb friction with a fixed friction coefficient of μ_f=0.5 throughout this study.

The workpiece material can be divided into two parts in butt configuration for modeling the FSW process in Figure 4.3 (b), or into a cladding layer on top of a substrate in Figure 4.3 (c). The cladding thickness can also be varied systematically, and the example in Figure 4.3 (c) corresponds to a thickness of 1 mm. All three stages of FSW process were modeled, including plunging of the tool, dwelling, and welding (i.e., laterally moving the tool). The processing parameters are varied in the range of the rotational speed of ω from 600 to 1400 rpm, the welding speed of V_t from 1 to 3 mm/s, and the plunging depth of h_p from 0.065 to 0.075 mm. The axial force, P, can be calculated afterwards. Additional simulations were also performed without the lateral motion, in order to validate an analytical solution (in Section 4.4) for the relationship between ω and torque.

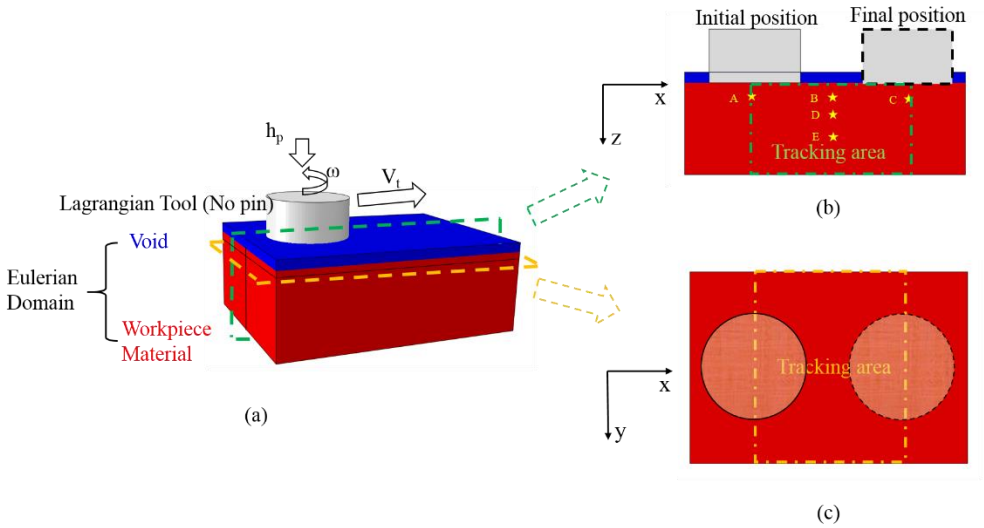

Figure 4.3 Finite element setup using the Coupled Eulerian-Lagrangian (CEL) approach for the FSW process. (a) Delineation of various Eulerian and Lagrangian domains in the model. (b) Cross-sectional view of the two workpieces with the dashed box being the tracking area. (c) The cladding-substrate interface with the dashed box being the tracing area.

The material is modeled by the hyperbolic-sine creep law, given by:

$$\dot{\varepsilon}_{creep} = A_n \left[\sinh\left(\frac{\sigma}{\sigma_{ref}} \right) \right]^n \exp\left(-\frac{Q_{creep}}{RT} \right) \tag{4.10}$$

where A_n is a pre-factor, σ_{ref} is the reference stress, n is the stress exponent, Q_{creep} is the activation energy, and R is the gas constant. The test material of interest is a precipitation-strengthened aluminum alloy, AA6061-T6, with the corresponding parameters given in Table 4.1 [88, 89]. Density of AA6061-T6 is taken as 2690 kg·m^{-3}. Other thermomechanical properties used in the simulation are listed in Table 4.2 [44, 56]. The Taylor-Quinney factor that describes the fraction of plastic work to be converted to heat is taken as 0.6.

4.3.2 Predicted bonding evolution in abutting workpieces

The computed strain rate, stress, and temperature fields from CEL finite element simulations can be used as inputs for the bonding evolution equations in Eqs. (4.5) and (4.6). As has already been shown in Chapter 2, the temperature field over the contact zone varies very slowly, but the strain rate and stress fields concentrate near the tool edge and are very sensitive to the interface stick-slip behavior. Therefore, a fine time step (practically found to be less than 1/100 of $2a/V_t$) needs to be adopted when integrating Eqs. (4.5) and (4.6) explicitly.

For the five reference points marked in the rectangular tracking regime on the workpiece-workpiece interface in Figure 4.3 (b), the evolution of their bonding fractions is presented in Figure 4.4, with ω =1000 rpm, h_p =0.07 mm, V_t =2 mm/s, and two initial bonding-fraction values of f_b^0 =0.01 and 0.2 (qualitatively representing a rough surface and a well-polished one). As reference points A-C are on the same height but at different *x* location, their responses are essentially the same except for the corresponding delay in time. As reference points B-E are at different depths, the deepest point E never reaches a meaningful bonding fraction, primarily due to the rapid decay of the strain field with respect to the depth. The final bonding fraction distributions in the tracking area under

Table 4.2 Thermomechanical properties for AA6061-T6 [44, 56]

Temperature (K)	Specific heat ($Jkg^{-1}K^{-1}$)	Young's modulus (GPa)	Poisson's ratio	Thermal conductivity ($Wm^{-1}K^{-1}$)	Thermal expansion (10^{-6} K^{-1})
298	945	66.94	0.33	162	23.5
373	978	63.21	0.334	177	24.6
422	1000	61.32	0.335	184	25.7
477	1030	56.8	0.336	192	26.6
533	1052	51.15	0.338	201	27.6
589	1080	47.17	0.36	207	28.5
644	1100	43.51	0.4	217	29.6
700	1130	28.77	0.41	229	30.7
755	1276	20.2	0.42	243	-

different rotational speeds are shown in Figure 4.5 with the same processing parameters as in Figure 4.4 and f_b^0=0.2.

The first critical observation from the bonding fraction evolution in Figure 4.4 and the final distribution in Figure 4.5 lies on the effects of f_b^0. The bonding fraction does not change until the material points enters into the severe thermomechanical process zone. From Figure 4.4 (a), if a full bonding can be reached, not only the transition from f_b^0 to unity is fast, but also the time for its occurrence is insensitive to f_b^0. From the depth profile in Figure 4.5 (b), there exists a Heaviside-like behavior of "on" and "off" bonding. Correspondingly in Figure 4.5 (a), the transition from full bonding (yellow) to no bonding (blue with the initial value f_b^0) is sharp. The location of this on/off interface is insensitive to f_b^0, but a lower value of f_b^0 tends to lead to a long tail that extends far from the on/off interface. As mentioned in Section 4.2, our model does not have an explicit treatment of surface roughness. Although this appears to be a limitation of our model, various degrees of surface roughness only affects f_b^0, and f_b^0 has negligible effect on the predicted bonding extent. Consequently, these results conclude that the rate-determining process in bonding analysis should be the cavity closure step, but not the rough surface contact analysis (which is otherwise sensitive to f_b^0).

The second critical observation from these results pertains to the competition between diffusive and creep-controlled cavity closure processes. All these calculations in Figure 4.4 and Figure 4.5 are based on integrating Eq. (4.6). Under realistic processing, geometric, and material constitutive parameters used in this FSW analysis, the corresponding results by summing the integrations of Eqs. (4.5) and (4.6) have indistinguishable differences from Figure 4.4 and Figure 4.5 when using a_{cavity} >1 μm. Cavities smaller than this size actually fall into the sintering behavior. A mechanistic understanding of such insignificant contribution from diffusive process can be derived from Figure 4.2, in which the thermomechanical histories experienced by reference points

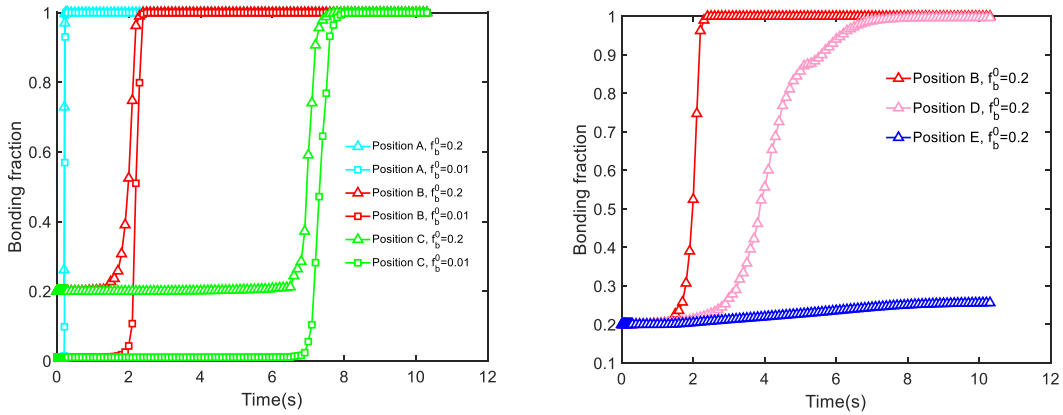

(a) (b)

Figure 4.4 The evolution of bonding fraction, f_b, for the five reference points in Figure 4.3 (b), based on the calculated strain-rate and temperature fields from CEL simulations. Two initial values, f_b^0 =0.01 and 0.2, represent initially smooth and rough workpiece-workpiece interface.(a) Reference points A, B, and C, moving away in x direction. (b) Reference points B, C, and E, moving away in the depth direction.

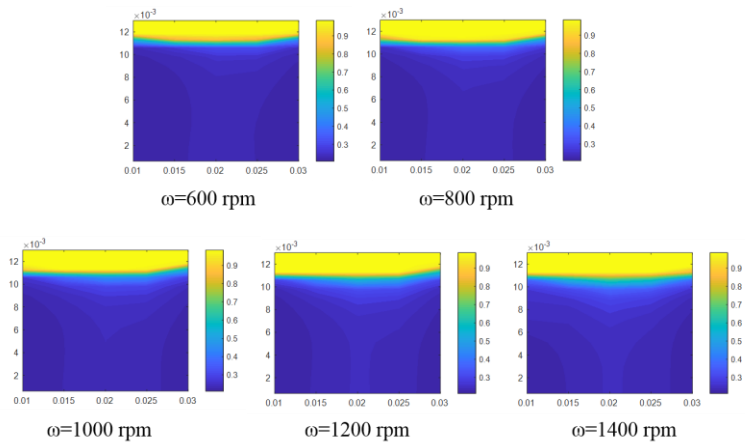

(a)

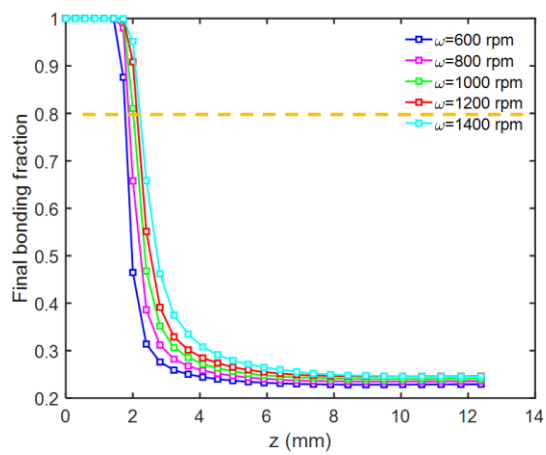

(b)

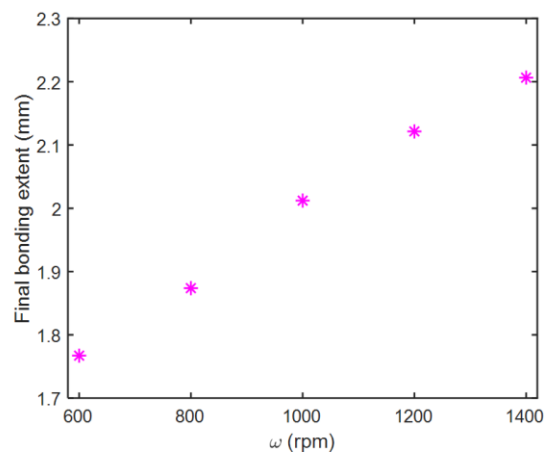

(c)

Figure 4.5 (a) Contour plots of the final bonding fraction with respect to varying ω for the FSW process in Figure 4.3 (b), with V_t =2 mm/s and h_p =0.07 mm. (b) The corresponding bonding fraction distribution in the depth direction. (c) The bonding extent with respect to varying ω when taking the critical bonding fraction for full bonding as 0.8.

B, D, and E (different depths) are plotted on top of L_{NR}. The corresponding f_b evolution of these three points is given in Figure 4.4 (b). Reference point B is the first one to reach the full bonding state, followed by reference point D. On the three trajectories, orange markers indicate when the tool front reaches the *x* coordinate of these three reference points, and purple markers indicate when the full bonding is reached for B and D and when the tool end leaves E. If a material point experiences a long period of time in high temperature and high strain rate like B and D in Figure 4.2 (b), it rapidly reaches the full bonding. But reference point E never reaches the full bonding, essentially because the corresponding strain rate field experience by this point is too low. Also the entire thermomechanical trajectory is needed; knowing the start and end points is certainly insufficient as bonding is predicated from integrating Eqs.(4.5) and (4.6). For the successful bonding in referent points B and D, the corresponding L_{NR} is extremely low. As the relative significance of diffusive and creep-controlled cavity closure processes is dictated by $\left(L_{NR}/a_{cavity}\right)^3$ in Eq. (4.9), it now becomes obvious that diffusive process has almost no contribution to the chosen FSW processing parameters. In other words, "diffusion bonding" as suggested by almost all solid-state-bonding studies is actually creep-controlled, but not governed by diffusive process.

For the sake of practical consideration and also noting the mesh size limitation, the critical value for the full bonding to take place is adopted as 0.8, as shown by the example in Figure 4.5 (b). From results in Figure 4.5 (c) and Figure 4.6, it is found that the bonding extent in the depth direction increases with the increase of tool rotational speed ω (mainly because of the corresponding increase of the strain-rate level), with the decrease of tool traveling speed V_t (for a longer time in the severe thermomechanical process zone), and with the increase of plunging depth h_p (due to the increased stress level). These trends agree qualitatively with the experimental discussions in the introduction section. A question that naturally arises is the maximum bonding depth, as these predicted values are still less than half of the tool radius (6.5 mm here). The answer will be addressed from our analytical solution in Section 4.4.

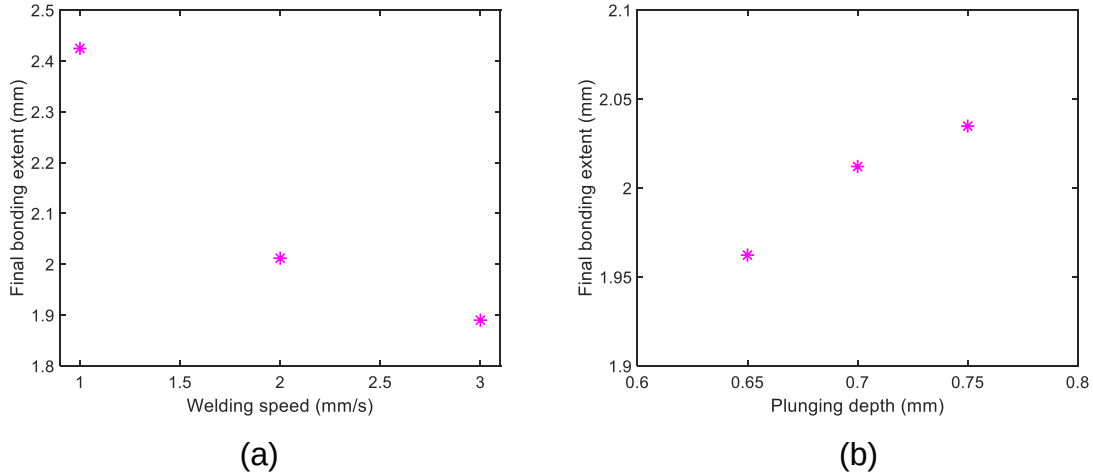

Figure 4.6 The final bonding extent for the FSW process in Figure 4.3 (b). (a) Varying V_t with ω=1000 rpm and h_p=0.07 mm. (b) Varying h_p with ω=1000 rpm and V_t=2 mm/s.

4.3.3 Predicted bonding evolution in cladding configuration

A variant form of FSW that also finds widespread applications is the bonding for the cladding-substrate configuration in Figure 4.3 (c). The calculation procedure is the same as the above subsection, with the results given in Figure 4.7 and Figure 4.8 for a cladding thickness of d =1 mm. Results in Figure 4.7(a) correspond to the instant when the tool center arrives the right boundary of the rectangular tracking zone in Figure 4.3 (c), so that the adjacent area has not reached the full bonding because of insufficient time in the high strain-rate state. The bonding distribution along the *y* direction again shows a Heaviside-type transition with long tails extending to faraway whereas the sensitivity to f_b^0 is found. With the increase of ω or h_p, or with the decrease of V_t, the bonding extent in lateral direction increases, but all these results are close to the tool radius of 6.5mm for the range of processing parameters used in these studies. Increasing the cladding thickness will reduce the bonding extent dramatically, which will be elaborated later in Section 4.5.

4.4 An analytical model for the prediction of bonding extent in FSW

In Chapter 2, based on the Hill-Bower similarity analysis [57-59] and the solution analogy between Newtonian viscous material and Hookean solid, we have developed an approximate yet analytical solution to relate the resulting torque and total heat generation rate to the stick-slip ratio of c/a, as shown by the problem setup in Figure 4.9. In this chapter, based on the analytical solution in Chapter 2 and the bonding model in Section 4.2, we now attempt to derive another approximate yet analytical solution to relate the final bonding extent to the processing parameters (such as the axial load and the tool rotational speed).

As shown in Figure 4.9, the interface shear stress is limited by the Coulomb friction stress,

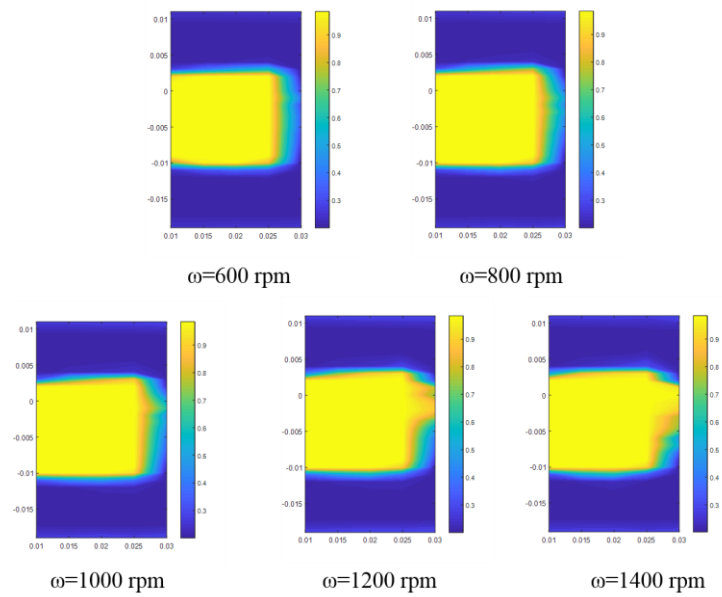

(a)

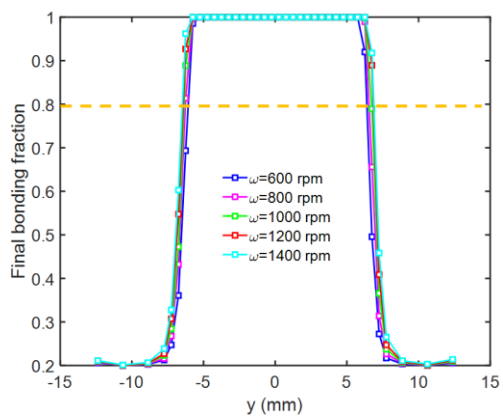

(b)

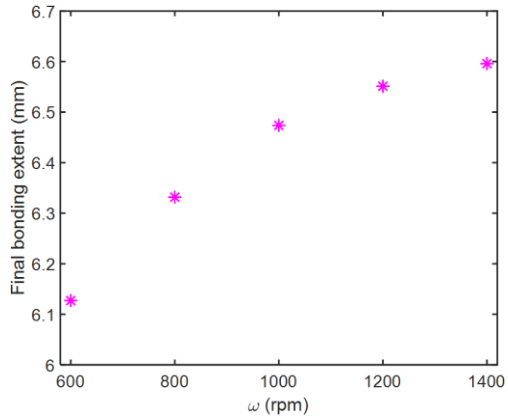

(c)

Figure 4.7 (a) Contour plots of the final bonding fraction with respect to varying ω for the cladding problem in Figure 4.3 (c), with V_t =2 mm/s and h_p =0.07 mm. (b) The corresponding bonding fraction distribution along the dashed line in Figure 4.3 (c). (c) The bonding extent with respect to varying ω when taking the critical bonding fraction for full bonding as 0.8. In these calculations, the cladding thickness is d =1 mm.

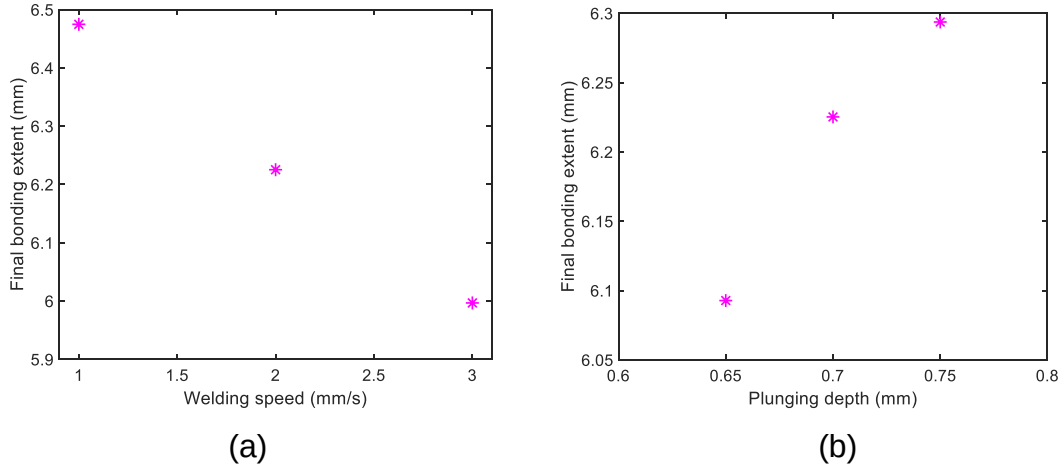

Figure 4.8 The final bonding extent for the FSW cladding process in Figure 4.3 (c). (a) Varying V_t with ω=1000 rpm and h_p=0.07 mm. (b) Varying h_p with ω=1000 rpm and V_t=2 mm/s.

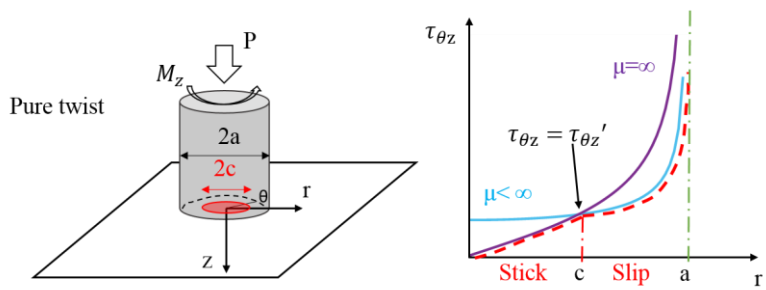

Figure 4.9 Our analytical model of the interface stick-slip behavior and the shear stress distribution. There exists an annular sliding zone ($c \le r \le a$) in which the theoretical shear stress at infinite friction is larger than the Coulomb friction as determined from the normal pressure distribution. The red dashed curve represents our approximate yet analytical solution. The resulting strain rate field in the substrate provides the critical input for bonding analysis.

$$\tau'_{\theta z} = \frac{\mu_f P}{2\pi a^2} \frac{1}{\sqrt{1-(r/a)^2}} \tag{4.11}$$

where μ_f is the friction coefficient. For infinite friction ($\mu_f = \infty$), the shear stress distribution that generates a rotational displacement field of the form of $u_\theta = r\theta$ (i.e., exactly following the spinning rigid indenter) is given by

$$\tau_{\theta z}\Big|_{\mu=\infty} = \frac{3M^*}{4\pi a^3} \frac{r/a}{\sqrt{1-(r/a)^2}} \tag{4.12}$$

where the torque parameter M^* remains to be determined. Under finite friction, the shear stress distribution can be taken as the lower one of the above two solutions, as shown by the dashed red curve in Figure 4.9. Equating these two solutions at $r = c$ determines the value of M^*. Therefore, the shear stress solution is approximately,

$$\tau_{\theta z}\Big|_{\mu<\infty} = \frac{\mu_f P}{2\pi a^2} \begin{cases} \dfrac{a}{c} \dfrac{r/a}{\sqrt{1-(r/a)^2}}, & r \le c : \text{stick} \\ \dfrac{1}{\sqrt{1-(r/a)^2}}, & c \le r \le a : \text{slip} \end{cases} \tag{4.13}$$

The resulting torque on the tool, as given by $M_z = \int_0^a \tau_{\theta z}\Big|_{\mu<\infty} 2\pi r dr$, can be written in a dimensionless function,

$$\frac{2}{3}\Big|_{c/a=1} \le \frac{M_z}{\mu P a} = \Pi_M(c/a) \le 0.78\Big|_{c/a=0} \tag{4.14}$$

as has been studied extensively in Chapter 2.

Now because the main processing parameters are ω, h_p, and V_t, we need to find the dependence of the normalized torque, $M_z/\mu P a$, on ω (which certainly needs an appropriate way to normalize). As $V_t << \omega a$, we conduct additional numerical simulations

in Figure 4.3 with the removal of the lateral moving of the tool. The resulting relationship of $M_z/\mu Pa \sim \omega$ is given in Figure 4.10, showing a reduction of torque with the increase of tool rotational speed, but the ordinate range falls within predictions in Eq.(4.14).

The elastic twisting contact solution for infinite friction is of the form in Eq.(4.12), leading to the following relationship between the rotation angle Θ and the torque [60]:

$$\Theta\big|_{\mu_f=\infty} = \frac{3M_z}{16Ga^3} \tag{4.15}$$

where G is the shear modulus. This solution works for $\mu_f = \infty$ and thus $c/a \to 1$. In general, we need to multiply Eq. (4.15) by a dimensionless function $\Phi(c/a)$,

$$\Theta\big|_{\mu_f<\infty} = \frac{3M_z}{16Ga^3}\Phi(c/a) \tag{4.16}$$

The friction coefficient does not explicitly enter into this dimensionless function due to the dependence of c/a on μ_f. From the solution analogy between Newtonian viscous material and Hookean solid, strains in elastic solution will be replaced by strain rates, and shear modulus by viscosity, so that the corresponding solution for our problem is

$$\omega = \frac{3M_z}{16\eta a^3}\Phi(c/a) \tag{4.17}$$

where the shear viscosity is $\eta = \frac{1}{2}\frac{ds_{ij}}{d\dot{\varepsilon}_{ij}}$ as evaluated from the material constitutive law in Eq. (4.10).

Results from CEL simulations are given in Figure 4.11 for five different values of ω. In the elastic solution of Eq. (4.16), when $c/a \to 0$, the rotation angle approaches infinity. Therefore, from the two limits: $\Phi(c/a=1)=1$ and $\Phi(c/a \to 0) \to \infty$, Figure 4.11 can be fitted to a tangent function of the form of

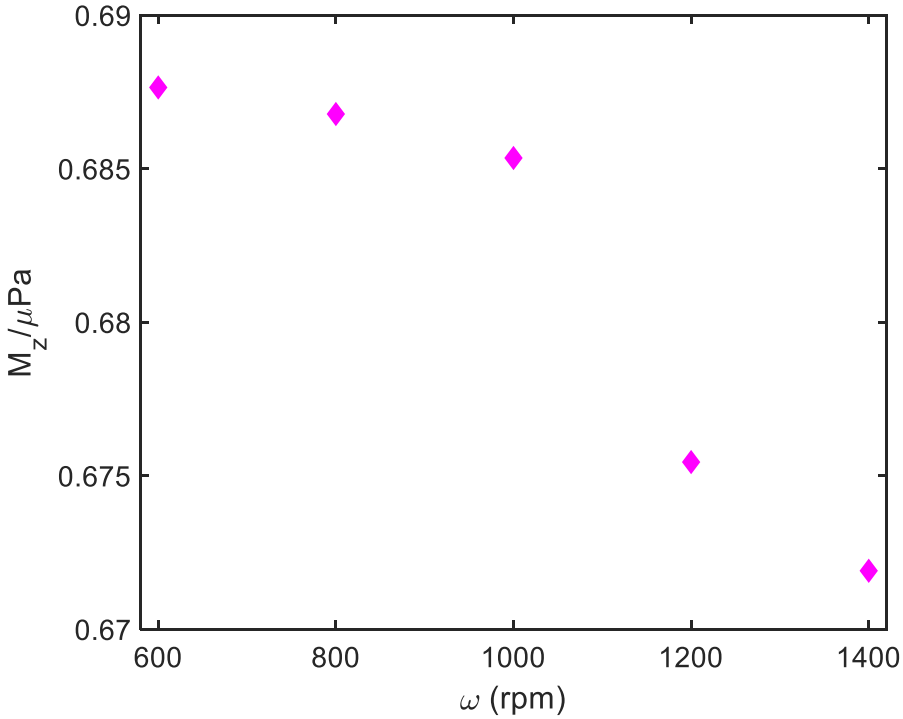

Figure 4.10 From CEL finite element simulations Figure 4.3 (but with the lateral motion turned off), the normalized torque, $M_z/\mu_f Pa$, is plotted against the tool rotational speed, ω.

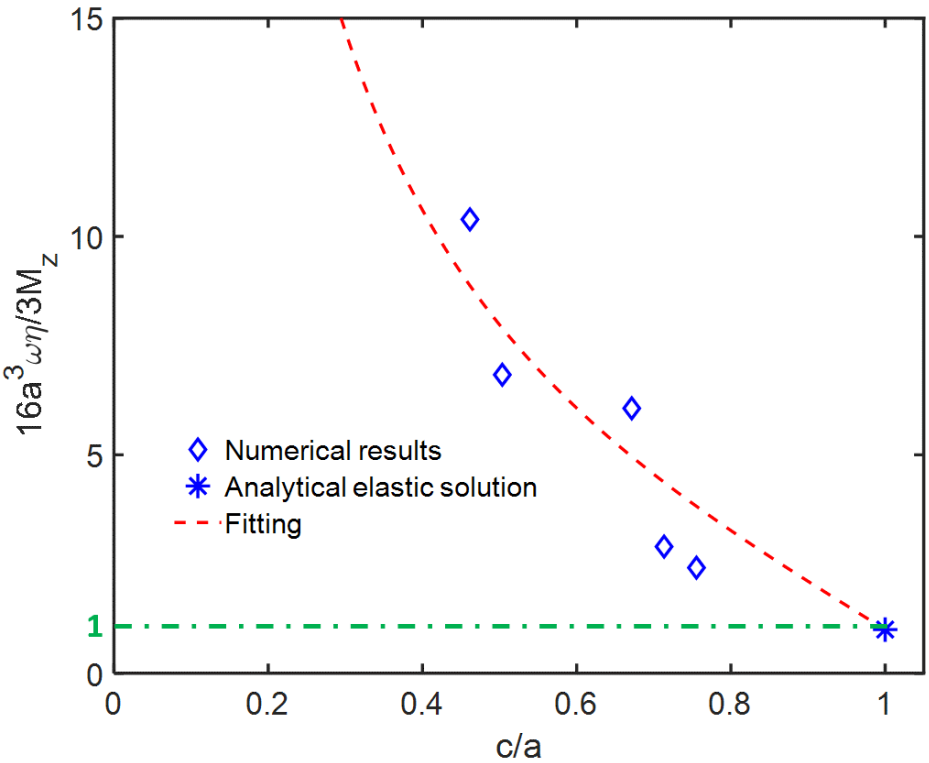

Figure 4.11 A dimensionless parametric group, combining ω, a, M_z, and workpiece material viscosity of η, is plotted against the stick-slip ratio of c/a. Blue diamonds are CEL simulation results with five different values of ω. Blue asterisk is the analytical solution at c/a=1. The red dashed curve represents a fitting equation, to be used to construct our flowchart in Figure 4.13.

$$\Phi\left(\frac{c}{a}\right) = 6.98\tan\left[\frac{\pi}{2}\left(1-\frac{c}{a}\right)\right]+1 \tag{4.18}$$

Substituting Eq. (4.18) into Eq.(4.17), we now make a connection between c/a and ω.

In Section 4.3, we have already shown that the diffusive process in Eq. (4.5) contributes insignificantly as compared to the creep-controlled process in Eq.(4.6). As the mean stress is negative in our FSW process, we rewrite Eq. (4.6) into a simplified form,

$$\frac{df_b}{dt} = f_b\left(1-f_b\right)\dot{\varepsilon}_{creep}^{eff} C_0\left(n, \left|\frac{\sigma_m}{\sigma_e}\right|\right) \tag{4.19}$$

with C_0 being a dimensionless function. Rearranging and integrating this equation gives

$$\int_{f_b^0}^{f_b^{final}} \frac{1}{f_b\left(1-f_b\right)} df_b = \int_{t=0}^{t=t^*} C_0 \dot{\varepsilon}_{creep}^{eff} dt \tag{4.20}$$

As shown by the strain rate and temperature fields in Chapter 2, the right-hand-side integrant is only large when the material point enters below the tool (or into the thermomechanical process zone). Thus the elapsed time can be approximated by $2a/V_t$, and $\dot{\varepsilon}_{creep}^{eff}\left(x_i, t\right)$ can take the highest value, $\dot{\varepsilon}_{creep,\max}^{eff}\left(x_i\right)$, over this entire elapsed time, leading to

$$\left[\ln\left(\frac{f_b}{1-f_b}\right)\right]_{f_b^0}^{f_b^{final}} \approx C_0 \dot{\varepsilon}_{creep,\max}^{eff} \frac{2a}{V_t} \tag{4.21}$$

For the FSW process, one primary interest is the prediction of bonding depth. For the steady state problem in Figure 4.12 (a), we only need to find $\dot{\varepsilon}_{creep,\max}^{eff}\left(z\right)$. Contact problems have an inverse square root decay of the deformation fields, so that we introduce the following

$$\dot{\varepsilon}_{creep,\max}^{eff} \approx \frac{\omega}{\left(\frac{z}{c}\right)^2 E\left(\frac{c}{a}\right)} \tag{4.22}$$

where the dimensionless function $E(c/a)$ is introduced to consider the dependence on interface stick-slip condition (which does not permit analytical solution, thus requiring curve fitting for this dimensionless function). Combining all the above equations, we now have the final bonding fraction at a given depth of z by

$$\ln\left[\frac{f_b^{final}(z)}{1-f_b^{final}(z)}\right] \approx \ln\left(\frac{f_b^0}{1-f_b^0}\right) + C_0 \frac{\omega}{(z/c)^2 E(c/a)} \frac{2a}{V_t} \tag{4.23}$$

Similarly, for the FSW cladding problem in Figure 4.12(b), the bonding extent in the lateral direction is derived as

$$\ln\left[\frac{f_b^{final}(y)}{1-f_b^{final}(y)}\right] \approx \ln\left(\frac{f_b^0}{1-f_b^0}\right) + C_0 \frac{\omega}{\frac{y^2+d^2}{c^2} E\left(\frac{c}{a},\frac{d}{a}\right)} \frac{2a}{V_t} \tag{4.24}$$

in which the dimensionless function $E(c/a, d/a)$ again needs to be curve fitted by comparing this equation to the bonding fraction calculations based on the actual strain-rate and temperature fields in CEL numerical simulations.

The key steps for the bonding fraction prediction are now summarized into the flowchart in Figure 4.13, as discussed below.

(1) Given all the processing parameters (ω, V_t, and h_p or P), material constitutive parameters in Eq.(4.10), and geometric parameters (a and tool shape). The most important ones are ω and P, as they are easily and practically accessible in the FSW technique.

(2) As the stick-slip ratio is not known a priori, an iterative procedure in the shaded box is needed.

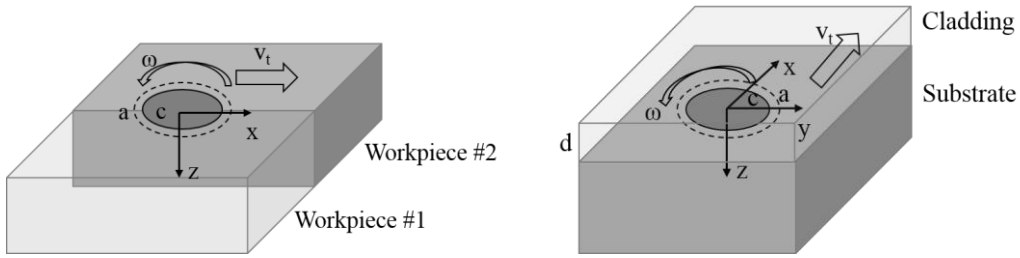

Figure 4.12 Schematic illustrations of the coordinates, stick-slip behavior, and interfaces in our bonding analysis, in which (a) corresponds to Figure 4.3 (b), and (b) corresponds to Figure 4.3 (c).

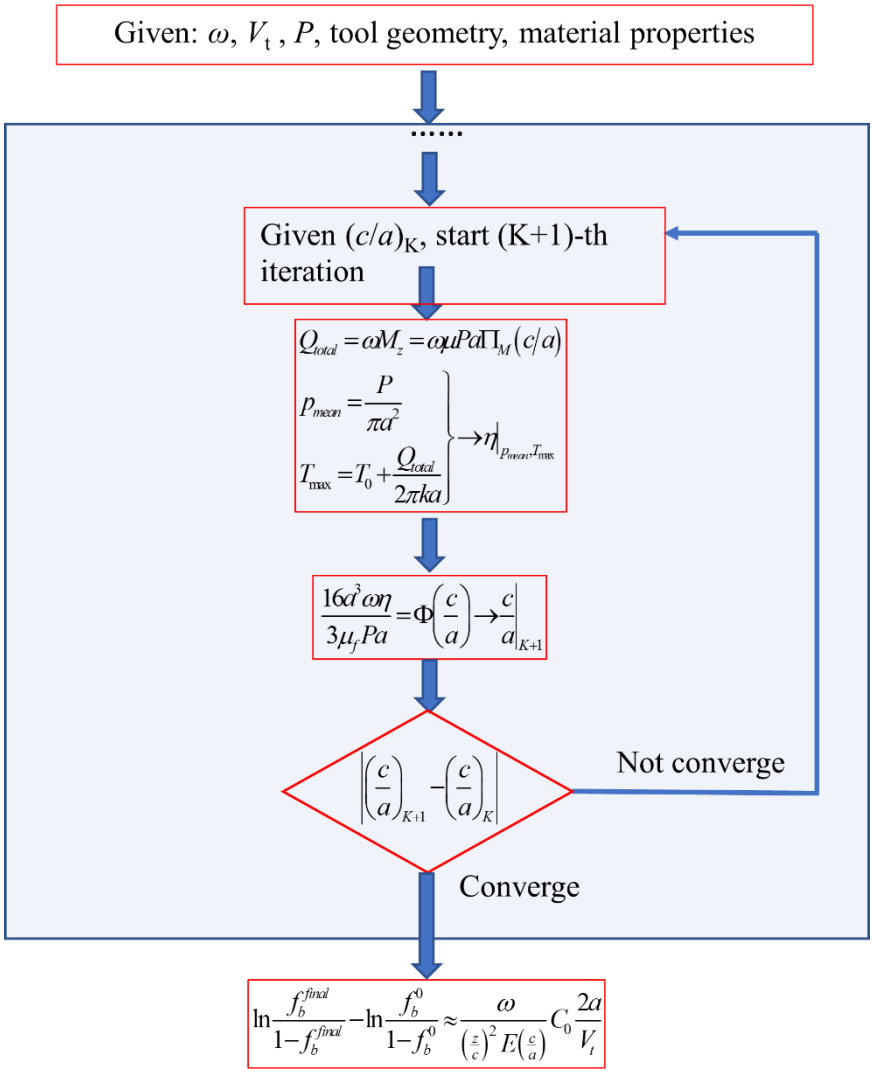

Figure 4.13 A flowchart representing our approximate yet analytical solution from the processing, geometric, and material constitutive parameters to the bonding fraction evolution.

a. At the beginning of the $(K+1)$-th iteration, we know $(c/a)\big|^{K}$.

b. Determine the normalized torque from $\frac{M_z}{\mu P a} = \Pi_M(c/a)$, and the total heat generation rate from $Q_{total} = \omega M_z$ (true only when the Taylor-Quinney factor is α_{TQ}=1).

c. Our prior numerical simulations in Chapter 2 show the large thermally affected zone, so that the temperature near the tool can be calculated from $T_{\max} = T_0 + \frac{Q_{total}}{2\pi k a}$, where k is the thermal conductivity, based on the Rosenthal solution for a circular zone of heat source on a half space [90].

d. Based on the mean contact pressure (because P is given) and the above temperature, we determine the corresponding material viscosity from the material constitutive law in Eq. (4.10).

e. Using the normalized function $\Phi(c/a)$ in Eqs. (4.17) and (4.18) to obtain a new stick-slip ratio of $(c/a)\big|^{K+1}$.

f. Check the convergence of $\left|(c/a)^{K+1} - (c/a)^{K}\right|$ and determine if next iteration is needed.

(3) Upon the determination of c/a, we can use Eq. (4.23) or Eq. (4.24) to calculate the final bonding fraction of a given material point. The fitting equation for $E(c/a)$ will be given later in Figure 4.15.

4.5 Comparisons between numerical and analytical models

This section aims to validate the bonding extent prediction from comparing the analytical solution (using the flowchart in Figure 4.13) to the detailed calculations in Section 4.3 (using the CEL-simulated fields as inputs to the bonding fraction evolution equations in Section 4.2).

For the FSW process in Figure 4.13 (b) and the results in Figure 4.4 Figure 4.6, plotted in Figure 4.14 are the final bonding fraction distributions in the depth direction with

a wide range of ω values. The numerical results are the same as in Figure 4.5(b). As explained in the previous section, the strain rate fields have a dependence on c/a that does not permit analytical solution. To this end, for each of these five ω values, we can read their corresponding c/a values from CEL simulations, adjust the E value in Eq. (4.23) to find agreements between the solid and dashed curves in Figure 4.14, and thus obtain a relationship between E and c/a, as presented in Figure 4.15. Also noting the form of $\Phi(c/a)$, we can curve the discrete diamond markers in Figure 4.15 by

$$E\left(\frac{c}{a}\right) = -2250\tan\left[\frac{\pi}{2}\left(1-\frac{c}{a}\right)\right] + 3070 \tag{4.25}$$

This fitting equation completes the flowchart in Figure 4.13.

For the FSW cladding process in Figure 4.3(c) and the results in Figure 4.7 and Figure 4.8, plotted in Figure 4.16 are the final bonding fraction along the lateral direction for different cladding thickness values. In Eq.(4.24) , the particular form of $\left(y^2+d^2\right)/c^2$ is assumed because of the inverse square decay of the deformation fields upon contact. In spite of tuning the dimensionless function of $E(c/a, d/a)$, predictions from our flowchart in Figure 4.13 show the same trends as the numerical results, especially for the thickness dependence. We choose a total of six different thickness values, and keep other processing parameters as ω=1000 rpm, V_t=2 mm/s, and h_p=0.07 mm. It can be seen that there is a sudden "on/off" transition when d increases from 2 to 3 mm, exactly in the same manner as the z-axis distributions of bonding fraction in Figure 4.5 and Figure 4.6. Consequently, we can directly use the bonding extent in the FSW process as the critical cladding thickness in the FSW cladding process.

Upon the fitting and validation of our analytical solution and the flowchart in Figure 4.13, we now aim to construct a bonding map with respect to the processing parameters. That is, with varying ω and P like in the actual applications, what is the corresponding

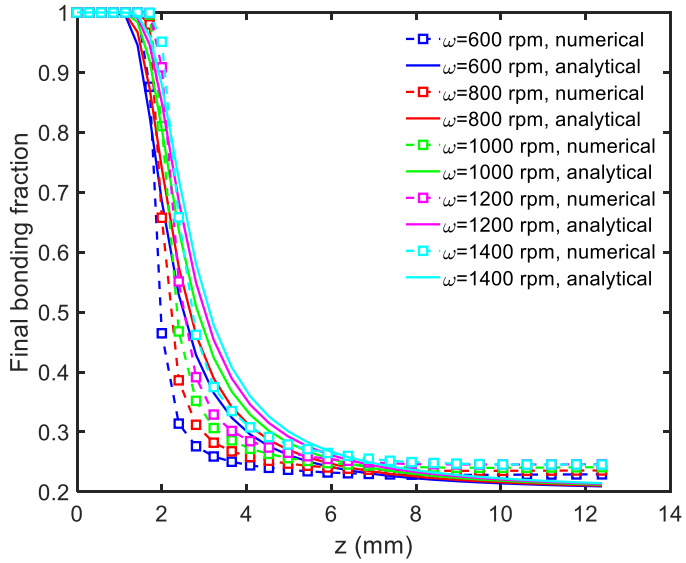

Figure 4.14 Comparisons between the CEL numerical simulation results in Figure 4.5(b) and our analytical model for the bonding fraction distribution along the depth direction in the FSW setup in Figure 4.3(b).

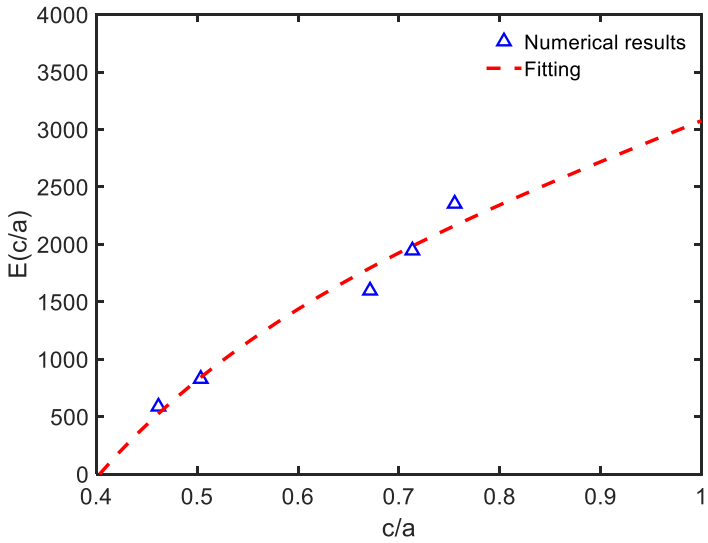

Figure 4.15 The dimensionless function, $E(c/a)$, in the flowchart of Figure 4.13.

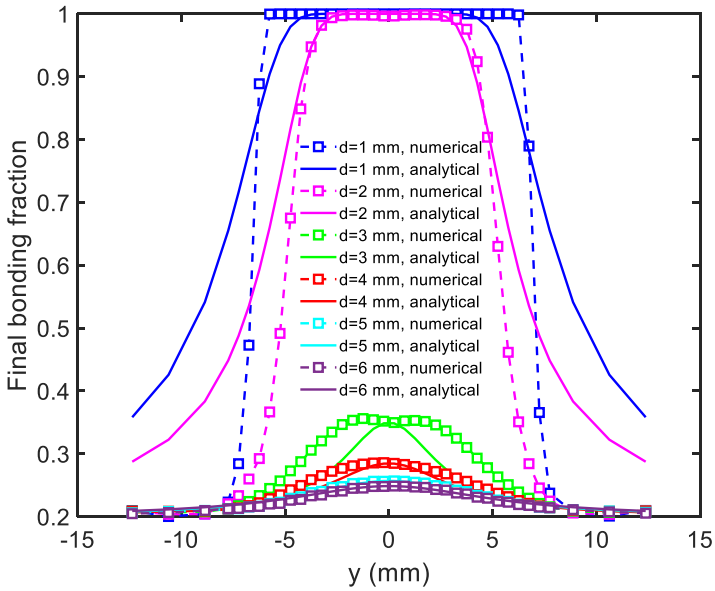

Figure 4.16 The final bonding fraction distribution on the cladding-substrate interface along the dashed line in Figure 4.3 (c), with respect to various choice of cladding thickness of d .

bonding extent in FSW? Do we also see a sudden "on/off" transition between full bonding and no bonding? Can a process window be determined with respect to these input parameters? Answers to these questions are given in Figure 4.17 and Figure 4.18. In our CEL simulations, the tool plunging depth is prescribed, but the axial pressure can be calculated as a result. The predicted c/a and bonding extent for the FSW process with respect to ω and P is given in Figure 4.17 and Figure 4.18, respectively, where surfaces are from our flowchart in Figure 4.13 and discrete triangles correspond to five different ω values from CEL simulations in Figure 4.3 (b). The collapse of discrete triangles onto the surfaces validates the success of our analytical solution and flowchart analysis. These 3D plots resemble cliffs on a terrain map, indicating the sharp "on/off" transition as exactly have been seen in Figure 4.3 and Figure 4.7. With the increase of ω and P, the bonding extent sees a rapid jump from zero to almost half of the tool radius. This upper bound is essentially due to the rapid decay of strain rate fields in the depth direction.

The bonding map in Figure 4.18 can be used to find the process window for the design and improvement of FSW processes. As a rule of thumb, the bonding extent sees a binary "on/off" transition, and the maximum bonding extent lies within the thermomechanical process zone, or simply half of the tool radius. Further validation of this bonding map requires additional FSW experiments as most of them in literature do not have direct bonding measurements.

4.6 Conclusions

A mechanistic understanding of bonding behavior under various operation conditions of the FSW process is critical in its successful engineering applications. There are three main contributions in this work as shown below.

(1) Bonding Model: Most solid-state-bonding models rely on rough surface contact and volumetric inter-diffusion for interfacial gap closure. Here we propose a completely different viewpoint, based on the well-established knowledge in grain boundary creep fracture of high temperature polycrystalline materials. The interfacial cavities will shrink under the combined action of sintering and applied compressive stresses via the Hull-Rimmer diffusive process, or under the creep-controlled deformation

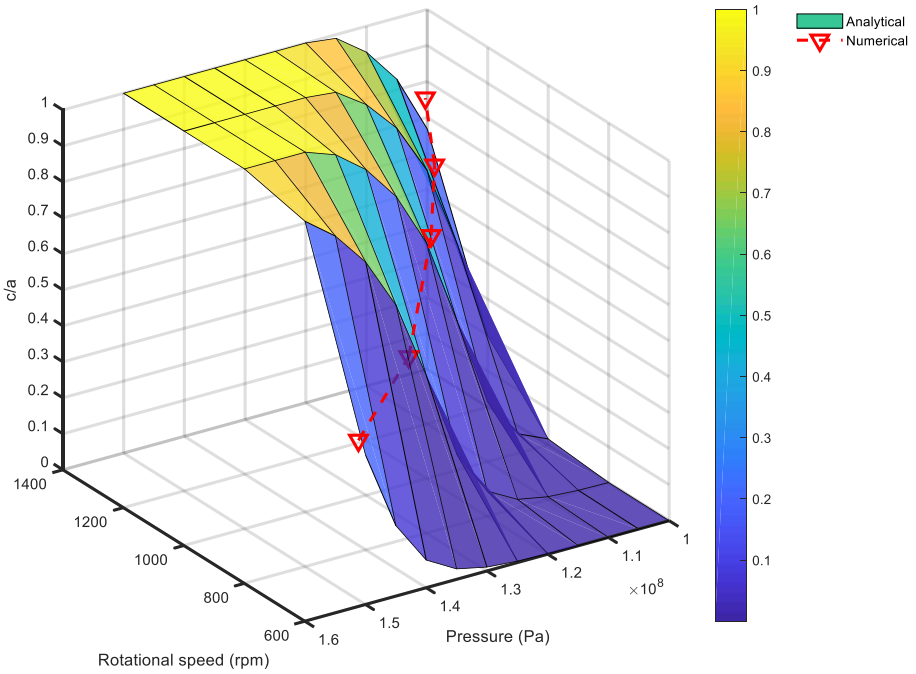

Figure 4.17 The stick-slip ratio with respect to two processing parameters (axial pressure and tool rotational speed), obtained from the CEL numerical simulations of the FSW setup in Figure 4.3 (b) and our analytical solution based on Figure 4.13.

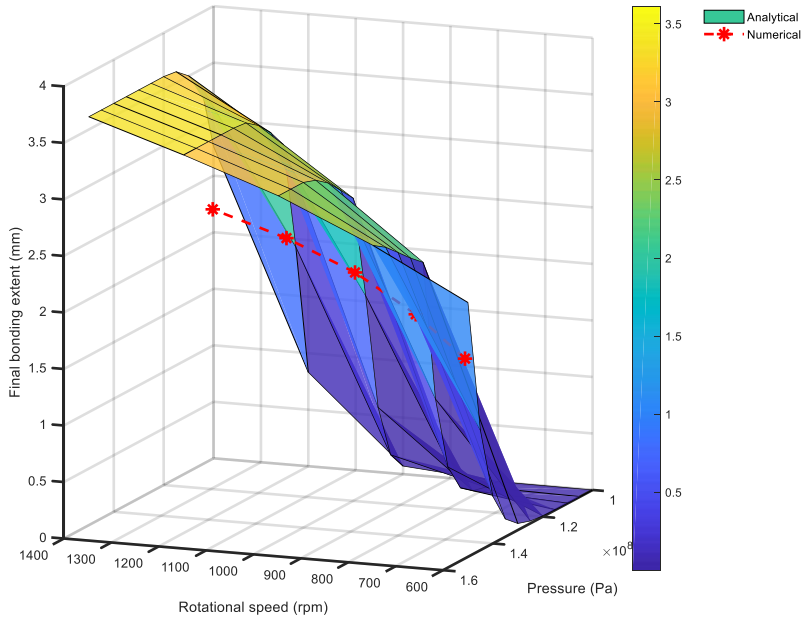

Figure 4.18 The final bonding extent on the workpiece-workpiece interface with respect to two processing parameters (axial pressure and tool rotational speed), obtained from the CEL numerical simulations of the FSW setup in Figure 4.3 (b) and our analytical solution based on Figure 4.13.

process. The competition between these two processes is dictated by the Needleman-Rice length scale, L_{NR}. When plotting the thermomechanical histories of materials under FSW tool, one can thus immediately tell that diffusive process plays a negligible role in the bonding evolution. Thus, the solid state bonding under FSW relies mainly on the creep strain rate in the adjourning workpieces, weakly on stress triaxiality, and negligibly on interfacial diffusion.

(2) Predicting bonding evolution from CEL simulation results: Using the calculated strain rate and temperature fields from CEL finite element simulations, we can predict the evolution of the bonding fraction. These results are insensitive to the initial bonding fraction, suggesting that a rough surface contact analysis be not needed. The bonding extent increases with the increase of tool rotational speed and plunging depth, or with the decrease of tool welding speed. The maximum bonding extent in the FSW process, as well as the maximum cladding thickness that can be made full-bonded in the FSW cladding process, is found to be about half of the tool radius.

(3) Bonding Map and Process Window: Based on the Hill-Bower similarity analysis and the solution analogy between Newtonian viscous material and Hookean solid, we can derive an approximate yet analytical solution to predict the bonding extent. The resulting bonding map shows that the dependence of bonding extent on processing parameters (mainly ω and P) shows a sharp transition between no bonding and full bonding. The analytical prediction agrees well with numerical simulations, thus providing a process window for future design and applications of this FSW technique.

5 Micromechanical investigation of the role of percolation on ductility enhancement in metallic glass composites

5.1 Introduction

It is well known that the poor ductility of monolithic bulk metallic glasses (BMGs) arises from the sudden initiation of strain localization into shear bands and the catastrophic propagation of these unconstrained shear bands [91]. Bulk metallic glass composites (BMGCs) have been developed to overcome this ductility limitation by introducing a second phase, either ex situ or in situ, to the glassy matrix. Processing, characterization, and mechanistic studies have been extensively reported and reviewed in the past two decades [92-102]. For example, a microstructure comprised of the $Zr_{58.5}Ti_{14.3}Nb_{5.2}Cu_{6.1}Ni_{4.9}Be_{11.0}$ (at.%) BMG matrix and the dendritic-like crystalline second-phase is found to be effective in blocking the shear bands with the volume fraction of the crystalline phase of about 55% [92]. Mismatches in the thermal and mechanical properties of the BMG and second phases could facilitate the occurrence of multiple shear bands, and the propagation of these shear bands can be arrested by these second phase particles [93-95]. Following the processing-microstructure-property relationship in materials science, a multitude of BMGC studies aim at the correlation between the ductility improvement and the microstructural design (including phase selection, property mismatches, and topological information). Detailed shear band arrangements for BMGCs were obtained during tensile tests by using both scanning electron microscopy (SEM) and finite element simulations [96], which found that the mechanical property mismatches between the matrix and second phases could change the relative degree of deviatoric and hydrostatic stress fields near the second phases. Thus the shear stress concentration caused by the shear bands could be mitigated. When the volume fraction of the second phase can be systematically varied, a number of studies [97-102] found a nonlinear relationship between the ductility improvement and this volume fraction, which was further interpreted by the percolation theory.

In a two-phase heterogenous structure, a physical property that has opposite dependence on these constituent phases will show a sharp change when a percolation limit

is reached. For example, consider an electrically insulating matrix with a conducting second phase. With the increase of the volume fraction of the second phase, above the percolation limit, it is always possible to find out a connected path, albeit serpentine, of the second phase that shorts the circuit. The percolation limit, as schematically illustrated in Figure 5.1, depends on the dimensionality (2D or 3D) and morphology of the second phase. Such a view on the connectivity has motivated many BMG studies to correlate the effectiveness of ductility improvement to the percolation limit, since it is the blocking of shear bands that delays the failure.

Here we would like to point out three shortcomings of the percolation-limit-based explanation for BMGCs:

(1) The shear bands in the BMG matrix are not randomly arranged, as mostly governed by the generally multiaxial stress state (e.g., mostly along 45º direction off the loading axis). The geometric way to block them effectively does not exactly correspond to the random connecting path in percolation analysis.

(2) The local interaction between shear bands and the second phase critically depends on property mismatches between BMG and second phases (e.g., rigid particles leading to nucleation of shear bands tangent to the particle surface, but soft particles giving shear bands in radial direction). As notches and holes have been found to be beneficial in some metallic glasses, near the curved surface of the second phase, a large ratio of mean to Mises stresses can be achieved that delays the shear failure. This is again not in the percolation analysis.

(3) Even with the second phase already in the percolation regime, the effectiveness of ductility improvement depends on the resistance to the impinging shear bands by the second phase. This will be elaborated below based on the results in Figure 5.2 and Figure 5.3.

Prior studies [97-102] are mostly focused on particles or dendrites as the second phase. In our recent experiment (details on processing and testing will be reported elsewhere), a Zr-based BMG phase was prepared by suction casting into a pure Ni foam, as shown in Figure 5.2. The volume fraction of Ni phase is about 11%, which is far less

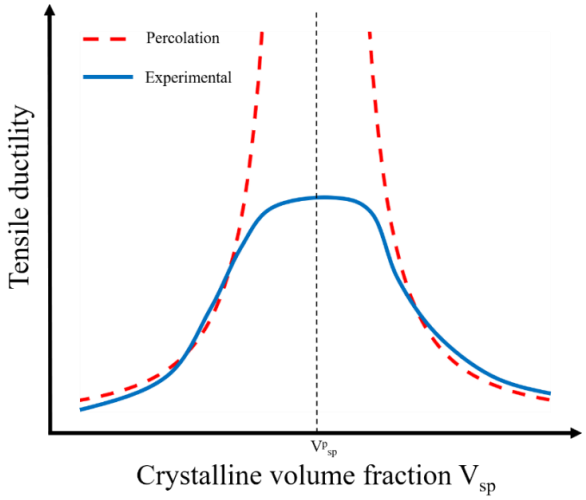

Figure 5.1 Schematic illustration of the dependence of tensile ductility on the volume fraction of the second phase, together with the percolation limits in which the divergence corresponds to some physical properties that rely on the connectivity of the two constituent phases.

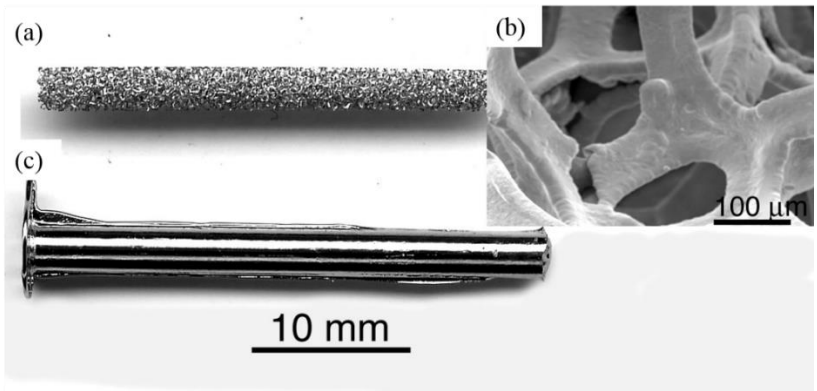

Figure 5.2 (a) Pure Ni foam was used to prepare a BMG composite, in which the Zr-based BMG phase infiltrated into the open space in the foam. (b) SEM image shows some detailed features of the open-cell structure in the Ni foam. (c) The as-cast rod of BMG-Ni composite. Note the same scale bar applies to both (a) and (c).

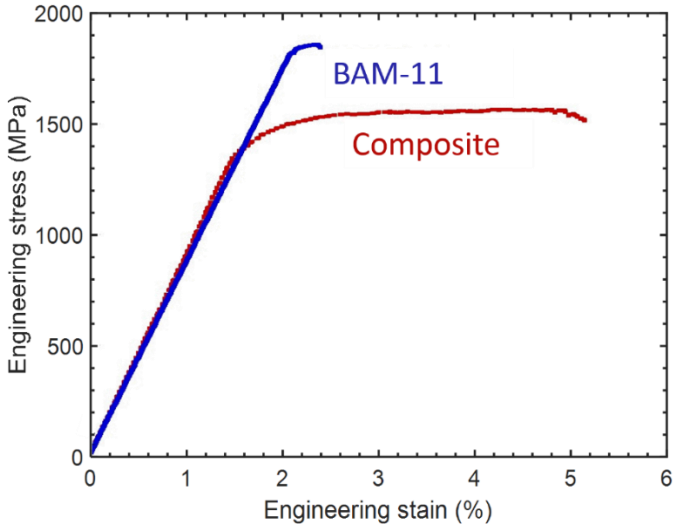

Figure 5.3 The engineering stress versus engineering strain curves for a Zr-based monolithic BMG and the BMG-Ni composite.

than the percolation limit for particulate composite. Nevertheless, the Ni foam is completely percolated. The engineering stress-strain curves are presented in Figure 5.3 for this BMG composite and the corresponding monolithic BMG. A ductility improvement of about 4% can be found. Although this is less than the ductility enhancement in dendritic BMGCs at about 50% volume fraction, it should be noted that the particle/dendrite BMG composites with similar volume fractions do not even exhibit noticeable ductility enhancement. We also note that the monolithic BMG has a yield strength of about 1.8 GPa and the pure Ni here yields at about 300 MPa, so that the strength of the foam-based composite agrees with a volume-fraction-weighted average of these two constituent phases. The moderate ductility enhancement in this fully percolated foam-based BMGC clearly depends on the resistance of the foam walls to the shear band propagation, which will be investigated in this work by a micromechanical finite element simulation.

The objective of this chapter is to investigate the role of percolation, as well as the mismatch in mechanical properties of the BMG matrix and the second phase, on the effectiveness of two types of second phases (i.e., particle and honeycomb) in blocking the shear bands through a thermo-mechanical finite element method. As will be discussed in Section 5.2, our method is based on a free-volume-based viscoplasticity model [91, 103], supplemented with the thermal transport analysis which provides a length scale and resolves the mesh dependence problem. Our simulation results in Section 5.3 will focus on the probability distribution of the effective shear strain in the BMG phase. We develop simple mechanistic models based on shear-force dipoles in bi-material and beam bending to understand these numerical findings. These results illustrate how factors other than percolation affect the ductility improvement in BMGCs. Finally, concluding remarks will be given in Section 5.4.

5.2 Constitutive model for BMGs

Among many constitutive laws for the deformation behavior of BMGs, a common feature is the introduction of a local structural measure, as well as the evolution of this order parameter in relationship to the inelastic deformation [91, 103]. The shear band will initiate if there is a certain softening mechanism with respect to this order parameter.

Different constitutive laws will not affect the simulation results of strain partitioning between the BMG and the second phases, and among the shear bands, provided the model has a physically meaning length scale. Along this line, we choose the multiaxial generalization of Spaepen's free volume model [91, 103]. The total strain rates are decomposed into elastic and plastic parts by

$$\dot{\varepsilon}_{ij} = \dot{\varepsilon}_{ij}^{elastic} + \dot{\varepsilon}_{ij}^{plastic} \tag{5.1}$$

Where

$$\dot{\varepsilon}_{ij}^{elastic} = \frac{1+\nu}{E}\left(\dot{\sigma}_{ij} - \frac{\nu}{1+\nu}\dot{\sigma}_{kk}\delta_{ij}\right) \tag{5.2}$$

$$\dot{\varepsilon}_{ij}^{plastic} = \upsilon e^{-\alpha v^{*}/v_f} e^{-\Delta G^{m}/k_B T} \sinh\left(\frac{\sigma_e \Omega}{2k_B T}\right)\frac{3s_{ij}}{2\sigma_e} \tag{5.3}$$

and δ_{ij} is Kronecker delta function, E the Young's modulus, ν Poisson's ratio, υ the frequency of atomic vibration, v_f the average free volume per atom, v^* the critical volume, α a geometric factor of unity, Ω the atomic volume, ΔG^m the activation energy for atomic jumps, σ_{ij} the stress tensor, σ_e the Mises stress, s_{ij} the deviatoric stress tensor, k_B the Boltzmann constant, and T the absolute temperature. The second exponential term in Eq. (5.3) is the Arrhenius dependence, the first exponential term provides additional volume for atomic jumps, the hyperbolic sine function describes the bias to the activation energy by the shear stress, and the last term assumes the flow directions are proportional to the deviatoric stress tensor. The free volume is a dynamic order parameter and evolves by the competition between a stress-driven creation process and a diffusional annihilation process, given by

$$\frac{\partial v_f}{\partial t} = \upsilon v^{*} e^{-\alpha v^{*}/v_f} e^{-\Delta G^{m}/k_B T}\left\{\frac{2\alpha k_B T}{v_f C_{eff}}\left(\cosh\frac{\sigma_e \Omega}{2k_B T} - 1\right) - \frac{1}{n_D}\right\} \tag{5.4}$$

where n_D is the number of atomic jumps (usually taken to be 3~10) that are needed to annihilate a free volume of v^*, and an effective modulus is

$$C_{eff} = \frac{E}{3(1-\nu)} \tag{5.5}$$

The shear-stress-driven process for the free volume creation in Eq.(5.4) will reduce the viscosity in Eq.(5.3), thus providing a strain softening mechanism. Consequently, strain localization into narrow shear bands can be understood as a constitutive instability. Since our objective is on a quantitative prediction of shear band strain, we note that predictions of the above model depend on the mesh size since it does not have a length scale. We can relate the rate of the plastic work to the heat transfer by

$$\rho C_P \frac{\partial T}{\partial t} = k\nabla^2 T + \alpha_{TQ}\sigma_{ij}\frac{\partial \varepsilon_{ij}^p}{dt} \tag{5.6}$$

where ρ is the material density, C_P is the specific heat, k is the thermal conductivity, and α_{TQ} is the Taylor-Quinney coefficient that describes the fraction of the plastic work that is converted to heat. The free volume model in Eqs. (5.3) and (5.4) has been implemented into a commercial finite element software, ABAQUS, by the user-defined material (UMAT) subroutine. The integration scheme is based on a fully implicit formulation. With the addition of Eq. (5.6), since the thermal transport analysis is already integrated in ABAQUS, we can merely adopt an explicit scheme for the last term in Eq. (5.6), which allows us to easily modify the UMAT code in [103] for the thermomechanical model in this work.

Our finite element simulations have a length scale,

$$L_H = \sqrt{\frac{k}{\rho C_P \upsilon} e^{\Delta G^m / k_B T}} \tag{5.7}$$

that governs the shear band width. Using ΔG^m ~10^{-19} J and the parameters in Table 5.2, this length is found to be about 10 μm. Individual phase sizes in BMGCs are typically much larger than this, so that a fine mesh that is needed to resolve the length scale in Eq. (5.7) gives rise to significant computational costs. It is found that, through our numerical simulations, adjusting ΔG^m and the mesh size proportionally to L_H will not change the predicted shear-band strain if averaged through the shear band thickness direction.

Consequently, our simulations presented in Section 5.3 are all based on a mesh resolution of 0.1 mm.

5.3 Numerical simulation results

The free-volume-based thermomechanical finite element framework allows us to systematically study various aspects of the microstructural information. The schematic illustrations in Figure 5.4 (a) and Figure 5.4 (b) will be used to investigate the effect of property mismatches between the BMG matrix and the second phase on the shear band arrangements. The setups in Figure 5.4 (c) and Figure 5.4 (d) will help us test the synergy between percolation and shear resistance on the shear bands. The volume fraction can be changed by adjusting the geometrical parameters on these plots. The following results adopt the constitutive parameters for a Zr-based BMG (Table 5.1) and Mises plasticity for Ni (Table 5.2). Other parameters not included in Table 5.1 and 5.2 include the heat conduction length, as has been discussed in the preceding section, and the initial free volume, taken as

$$v_f\big|_{t=0} = 0.05\alpha v^* \tag{5.8}$$

It should be noted that a quantitative experimental calibration of the parameters in the Spaepen model still remains elusive. On one hand, the unit events in this model, being atomistic jumps into nearby vacancies, could be generalized to cooperative motion of shear transition zones (STZs). However, the STZ model has quite complicated kinetic processes that are not feasible to deal with in a constitutive modeling framework (e.g., stochastic processes must be incorporated). On the other hand, regardless of the debates on the atomistic mechanisms, most available models lead to the strain localization via the constitutive instability (softening being a quintessential one). To this end, the generalized Spaepen model in the previous section can be regarded as a phenomenological approach.

The shear-band initiation site is found to depend on the stiffness of the second phase, as shown by the Ni and the rigid second phases in Figure 5.5. Contours of SDV1, corresponding to $v_f \big/ \left(\alpha v^*\right)$, together with the displacement field (with a magnification

Table 5.1 Representative values for material parameters in the free volume model of the BMG phase.

Parameters	Value
Reference stress (GPa), $\sigma_0 = 2k_B T/\Omega$	0.32
Young's modulus	$290.6\sigma_0$
Yield stress	$5.8\sigma_0$
Poisson's ratio	0.333
Density (kg·m^{-3})	6834
Specific heat (J·kg^{-1}K^{-1})	320
Thermal conductivity(W·m^{-1}K^{-1})	4.8
Thermal expansion coefficient(K^{-1})	10.1×10^{-6}
Reference temperature (K)	298

Table 5.2 Representative values for material parameters in the conventional Mises plasticity model of the Ni phase.

Parameters	Value
Reference stress (GPa), $\sigma_0 = 2k_B T/\Omega$	0.32
Young's modulus	$503\sigma_0$
Yield stress	$1\sigma_0$
Poisson's ratio	0.3
Density (kg·m^{-3})	8908
Specific heat (J·kg^{-1}K^{-1})	440
Thermal conductivity(W·m^{-1}K^{-1})	90.7
Thermal expansion coefficient (K^{-1})	13×10^{-6}
Reference temperature (K)	298

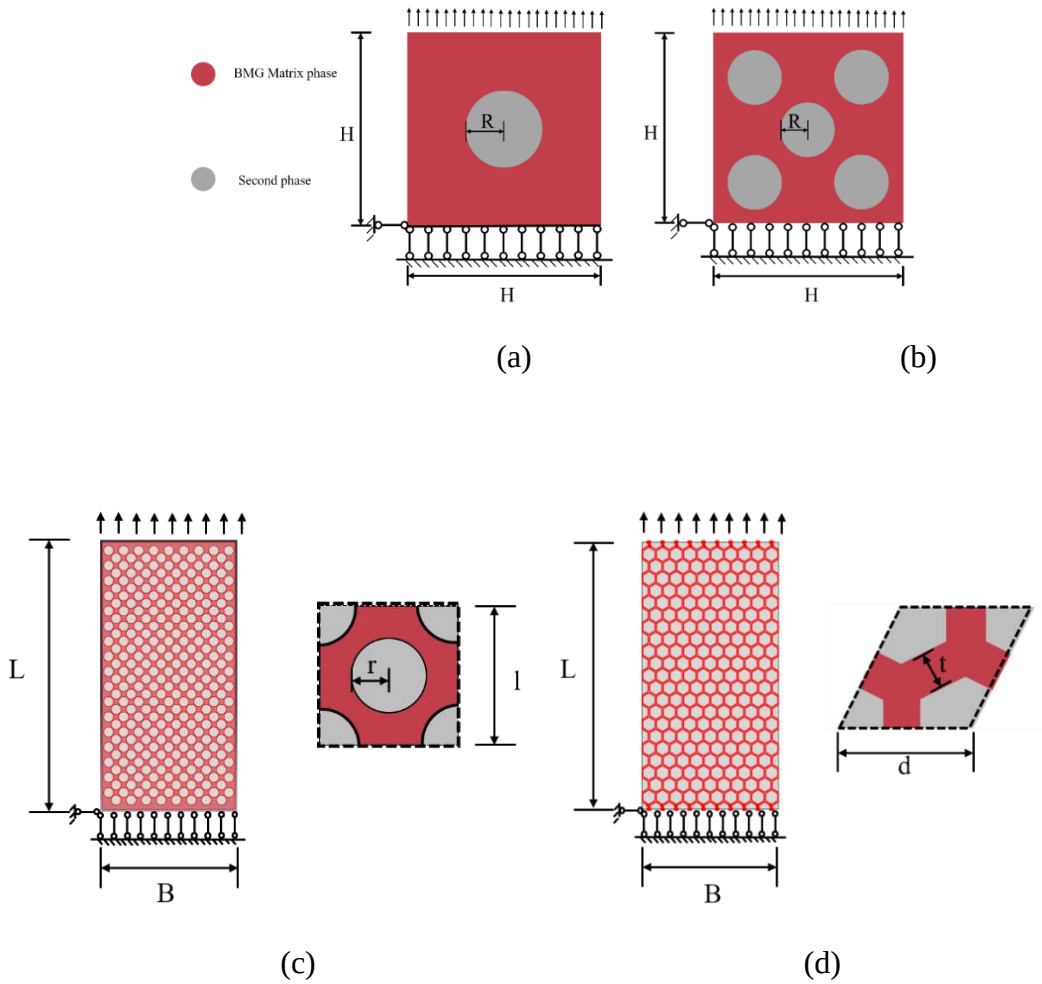

Figure 5.4 Schematic illustration of the BMG-composite model with various microstructural features, in which the red regime represents the BMG phase and the gray regime represents the crystalline second-phase. (a) One inclusion model with H=2.5mm and R=0.4mm. (b) Five inclusion model with H=2.5mm and R=0.3mm. These two models will be used to investigate the shear-band nucleation behavior. (c) Particulate composite model with L=19mm and B=10mm. The volume fraction of the second phase can be tuned by varying both *l* and *r*. (d) Honeycomb composite model with L=19mm and B=10mm, to mimic the foam-based composite in Figure 5.2. The thickness *t* can be varied to change the volume fraction.

factor of unity) exhibit the geometrical arrangements of these shear bands. For the Ni second phase, shear bands take place from the interface and emanant outwards, so that their blockage needs to be realized by arranging other second-phase particles in these 45º directions. When the second phase is rigid, shear bands are found to be tangent to the interface, so that arranging other rigid particles in 45º directions is futile; they need to be translated upward or downward by one radius distance. Following the results in Figure 5.5 (a), we now align a few soft particles in the two 45º directions and also vary the elastic constants of these particles from $1E_{\mathrm{Ni}}$ to $5E_{\mathrm{Ni}}$, as shown in Figure 5.6. Comparing Figure 5.5 (a) to Figure 5.6 (a), it is found that, instead of having a major shear band running along the centers of these particles, multiple shear bands appear and eventually the most strain-localized shear band will be selected as the one off from the centerline of these particles. Comparing Figure 5.5 (b) to Figure 5.6 (c), it is found that the increase of the stiffness of the second phase significantly reduces the strain localization and simultaneously facilitates the initiation of multiple shear bands. A convenient way to illustrate the degree of shear band blockage is given in Figure 5.7, by plotting the volumetric probability of the Mises strain in the BMG matrix. These three cases correspond to those in Figure 5.6. Note the logarithmic scale in the ordinate. The vast majority in the BMG matrix has the strain magnitude around the applied macroscopic strain (being 0.1 in Figure 5.7), while a low volumetric fraction in the BMG matrix has extremely large shear strain in the shear bands. Because the BMGC ductility is governed by these extreme cases, we see that the stiffness increase of the second phase, i.e., from Figure 5.7 (a) to Figure 5.7 (c), reduces the tails at the large strain limit and thus delays the potential failure in these shear bands. From the above simulation results in Figure 5.5-Figure 5.7, we can conclude that, to effectively block shear bands, any possible shear-band line or plane (e.g., two 45º directions off the loading axis in uniaxial tests) should strike through the second phase. Also the shear-band resistance in the second phase depends synergistically on the stiffness, shape, and density of the second phase. A simple mechanistic analysis is given next in Figure 5.8.

When a propagating shear band is impinged at the interface between the BMG matrix and the second phase, the resulting stress field can be approximated by that caused

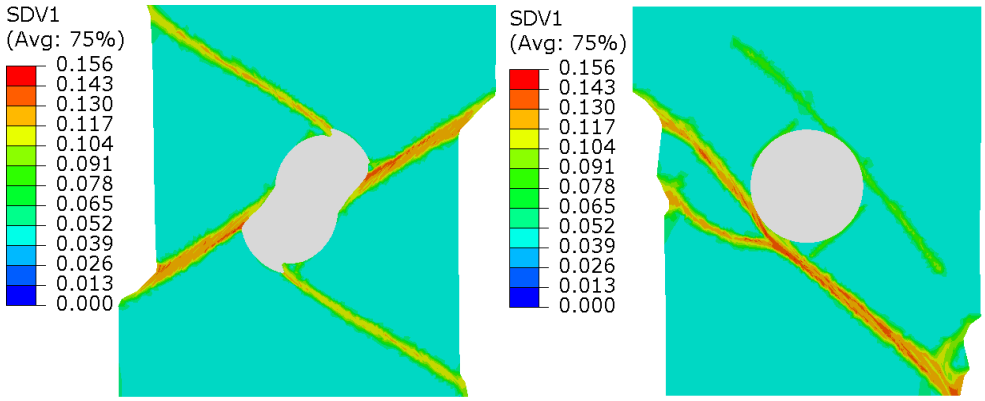

(a) (b)

Figure 5.5 From the geometric setup in Figure 5.4 (a), the shear-band nucleation site and the subsequent propagation are sensitive to the mechanical properties of the second phase: (a) with Ni being the second phase, and (b) with the second phase being rigid. In these contour plots, SDV1 represents the normalized free volume.

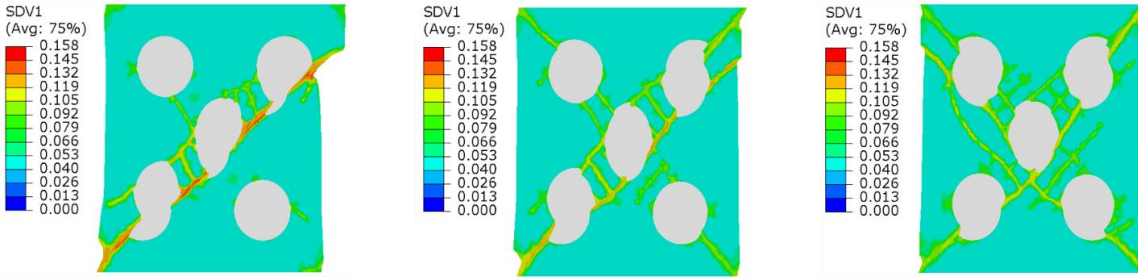

$E_{sp}=1E_{Ni}$ $E_{sp}=3E_{Ni}$ $E_{sp}=5E_{Ni}$

(a) (b) (c)

Figure 5.6 From the geometric setup in Figure 5.4 (b), the initiation and propagation of shear bands exhibit a strong dependence on the mechanical properties of the second phase: (a) with Ni being the second phase, (b) the same as Ni but with a three-times increase of the Young's modulus, (c) with a five-times increase of the Young's modulus. All these figures are plotted when the macroscopic applied strain equals to 0.1.

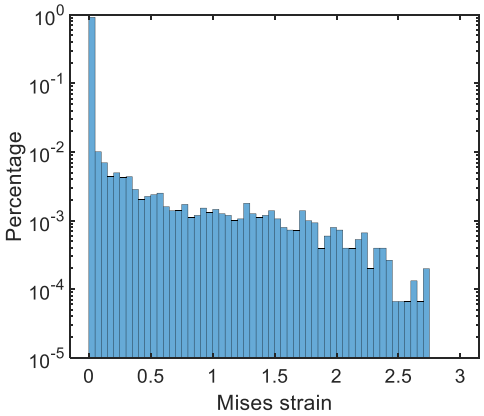

(a)

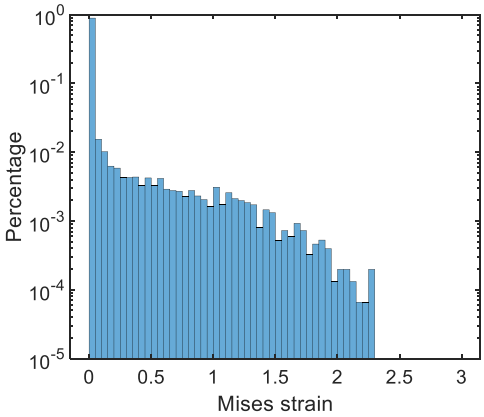

(b)

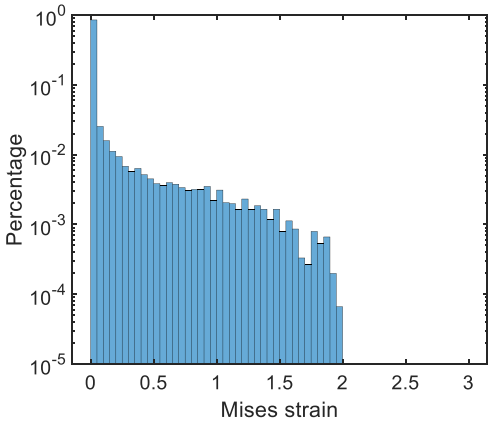

(c)

Figure 5.7 Corresponding to the simulation results in Figure 5.6, the probability distribution of Mises strain in the BMG phase is plotted when the macroscopic applied strain equals to 0.1. With the increase of the Young's modulus of the second from that of Ni to three-times and five times, it becomes less likely to find out the location in BMG phase with large shear strain, meaning that the stiff second-phase suppresses the extent of shear localization in the BMG phase.

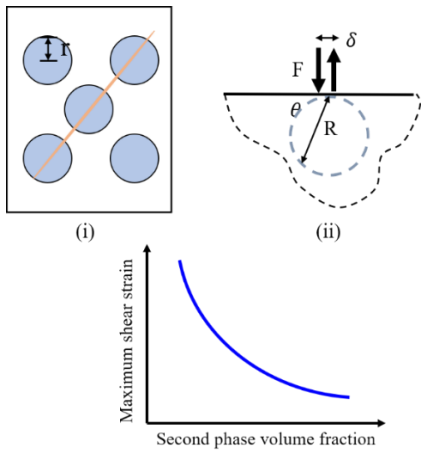

(a)

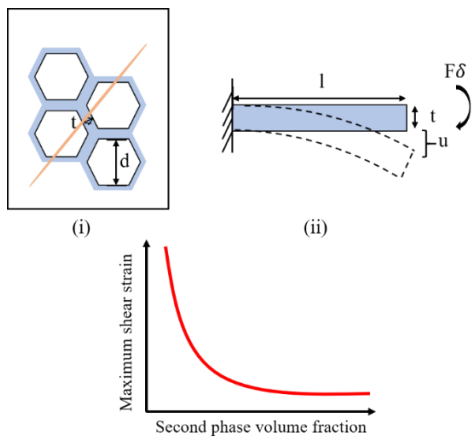

(b)

Figure 5.8 Schematic illustration of the BMG-composite models and the mechanical response on the second phase. (a) For a shear force dipole applied on the circular second phase, the deformation resistance (see text for the mathematical representation) scales as $1/R^2$. Thus the lower the volume fraction of the second phase, the smaller its deformation resistance and the higher the effective shear strain of the neighboring shear band that applies this shear force dipole to the second phase. (b) In the honeycomb configuration, the bending resistance scales as $1/t^3$, so that a low volume fraction has a reduced resistance to the neighboring shear band propagation.

by an interfacial shear-force dipole in Figure 5.8 (a). In the plane strain condition, subjected to a pair of line forces at a spacing of δ, the resulting shear strain field scales as [104],

$$\gamma_{R\theta} = \frac{2F\delta}{\pi R^2 b G^*} \sin^2\theta \tag{5.9}$$

where R is the distance to the location of the applied dipole, b is the out-of-plane thickness, and G^* is the effective shear modulus. The product of $F\delta$ is proportional to $E_{BMG} L_H \varepsilon_e^{SB}$, so that the shear resistance scales as $1/R^2$, or equivalently speaking, inversely to the volume fraction of the second phase. Note G^* also depends on the size of the second phase. For a bimaterial, ignoring the difference in Poisson's ratios, we can write

$$G^* \approx \left[1/G_{BMG} + 1/G_{\text{second-phase}}\right]^{-1} \tag{5.10}$$

Borrowing the solution from the indentation response on a film/substrate system [105], we can write,

$$G^* \approx \left[\frac{1}{G_{BMG}}\left(1+e^{-\beta R/L_H \varepsilon_e^{SB}}\right) + \frac{1}{G_{\text{second-phase}}}\left(1-e^{-\beta R/L_H \varepsilon_e^{SB}}\right)\right]^{-1} \tag{5.11}$$

which includes an exponential dependence on the ratio of shear-band-induced offset to second-phase size. The dimensionless factor β of order unity needs to be determined numerically. As R decreases, the contribution from the second phase stiffness reduces rapidly. The joint result of R^2 and G^* in Eq. (5.9) leads to a schematic drawing of the maximum shear band strain versus the second phase volume fraction V_{sp} ($V_{partcile}$ here denoting the particulate second-phase) in Figure 5.8 (a), roughly scaling as

$$\varepsilon_{e,BMG}^{\max} \sim \frac{1}{V_{particle}}\left[1+\frac{G_{BMG}}{G_{particle}}\frac{1-e^{-\beta l\sqrt{V_{particle}}/L_H \varepsilon_e^{SB}}}{1+e^{-\beta l\sqrt{V_{particle}}/L_H \varepsilon_e^{SB}}}\right] \tag{5.12}$$

For the honeycomb composite in Figure 5.4 (d), the resistance to the shear band can be estimated from a cantilever beam subjected to a torque [104],

$$\varepsilon_{bending}^{\max} = \frac{6F\delta l}{Ebt^3} \tag{5.13}$$

which relates the maximum bending strain to the beam length l, thickness t, and out-of-plane width b. When the cell size of the honeycomb remains unchanged, the volume

fraction of the second phase will be proportional to the wall thickness *t*. Consequently, the maximum shear-band strain will scale with respect to the second phase volume fraction by,

$$\varepsilon_{e,BMG}^{\max} \sim \frac{1}{V_{honeycomb}^{3}} \tag{5.14}$$

as schematically shown in Figure 5.8 (b).

In addition to the percolation analysis, the two relationships in Eq. (5.12) and Eq. (5.14) provides the ductility dependence on the volume fraction, as will be validated by our simulation results in Figure 5.9-Figure 5.14. In these simulations, the BMG matrix and the Ni second phase adopt the material parameters in Table 5.1 and 5.2, respectively. For the particulate BMGC, we keep *l* as a constant in Figure 5.4 (c) and change the volume fraction by adjusting the particle size. The corresponding strain and temperature contours with different volume fractions are given in Figure 5.9 and Figure 5.10, respectively. As the trend predicted in Eq. (5.12), the increase of the volume fraction leads to an increased effectiveness of blocking the shear bands, as well as an increased trend of shear band multiplication. Accordingly, the temperature field becomes less localized and its magnitude also reduces. The volume probability of the shear-strain distribution in the BMG matrix is given in Figure 5.11. The tail at the highest shear-band strain reduces both in height of probability and in extent of shear strain, indicating an increased effectiveness of ductility improvement.

Similar trends have been found for the honeycomb case in Figure 5.12-Figure 5.14. In this case, the volume fraction of the second phase is varied by changing the wall thickness while the cell size remains a constant in Figure 5.4 (d). With the increase of V_{sp}, more shear bands will form, meaning that thicker walls are more effective in reducing the shear localization. Compared to the particle BMGC in Figure 5.9-Figure 5.11, above a certain volume fraction (roughly 20% here), the honeycomb BMGC is more effective in resisting shear bands than the particle BMGC. As shown in Figure 5.14, the highest shear-band strain reduces from 3.0 to 0.5 when $V_{honeycomb}$ increases from 10% to 60%. This comparison can also be seen in Figure 5.15, which plots the maximum shear-band strain

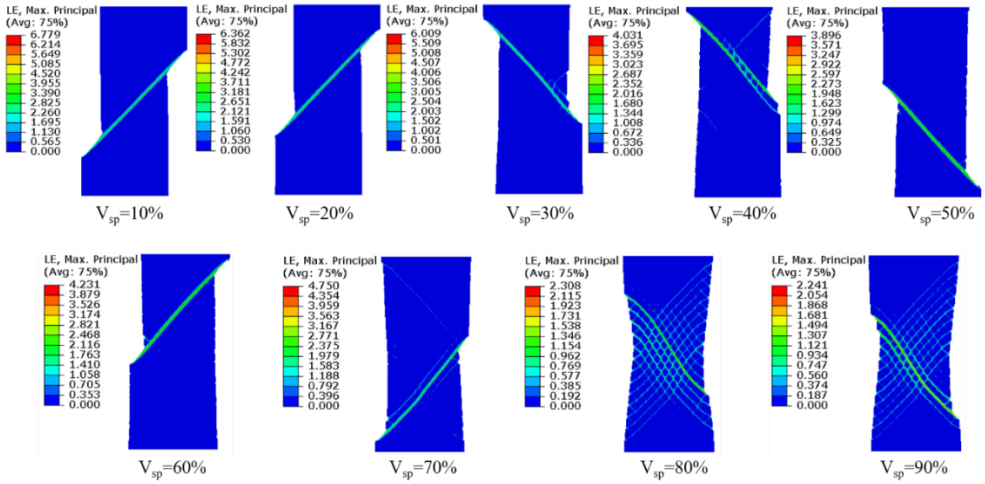

Figure 5.9 Contour plots of the maximum in-plane principal strain in BMG-composite model of Figure 5.4 (c), when the applied macroscopic strain equals to 0.13. The volume fraction of the Ni phase ranges from 10% to 90% as labeled.

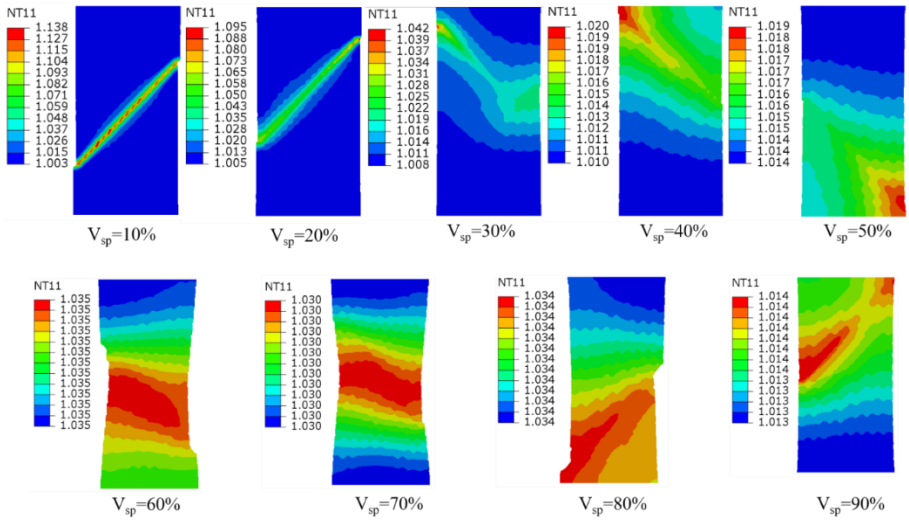

Figure 5.10 Contour plots of the temperature field in BMG-composite model of Figure 5.4(c). The volume fraction of the Ni phase ranges from 10% to 90% as labeled. It should be noted that these snapshots were taken at different applied strains than those in Figure 5.9.

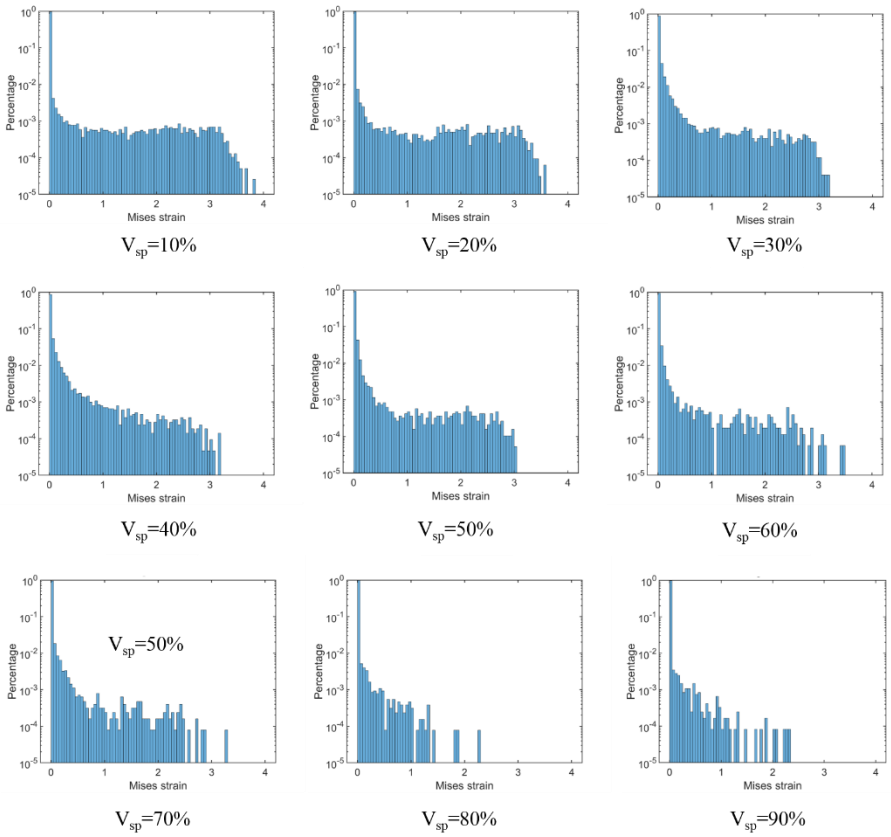

Figure 5.11 Corresponding to the simulation results in Figure 5.9, the probability distribution of Mises strain in the BMG phase is plotted when the macroscopic applied strain equals to 0.04. Only the portion of the BMG phase with the Mises strain larger than 0.04 is included in these probability plots. The probability at high Mises strain reduces as the volume fraction increases, meaning the shear bands are more effectively blocked and thus have reduced shear-strain magnitude. Red-dotted curves provide a logarithmic fitting and thus gives the extent of the maximum shear-band strain.

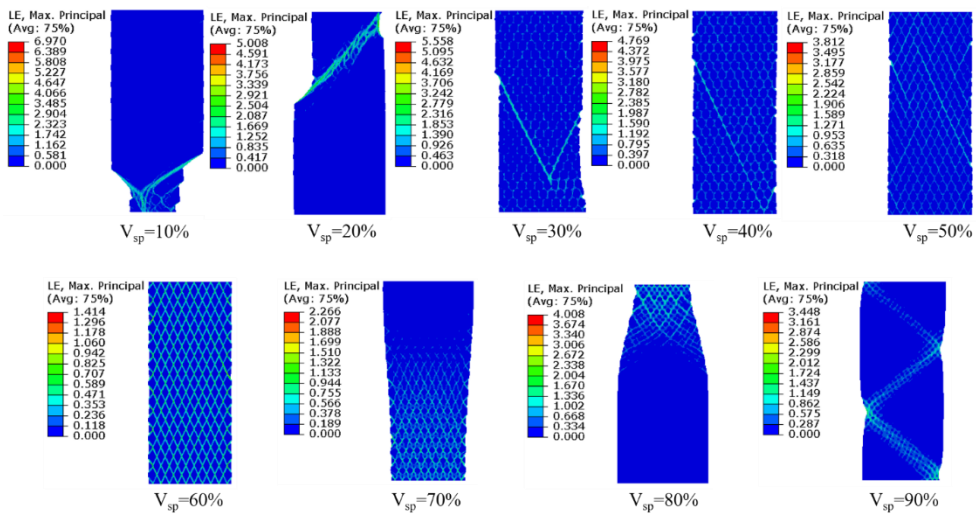

Figure 5.12 Contour plots of the maximum in-plane principal strain in the honeycomb BMG-composite model of Figure 5.4 (d), when the applied macroscopic strain equals to 0.13. The volume fraction of the Ni phase ranges from 10% to 90% as labeled.

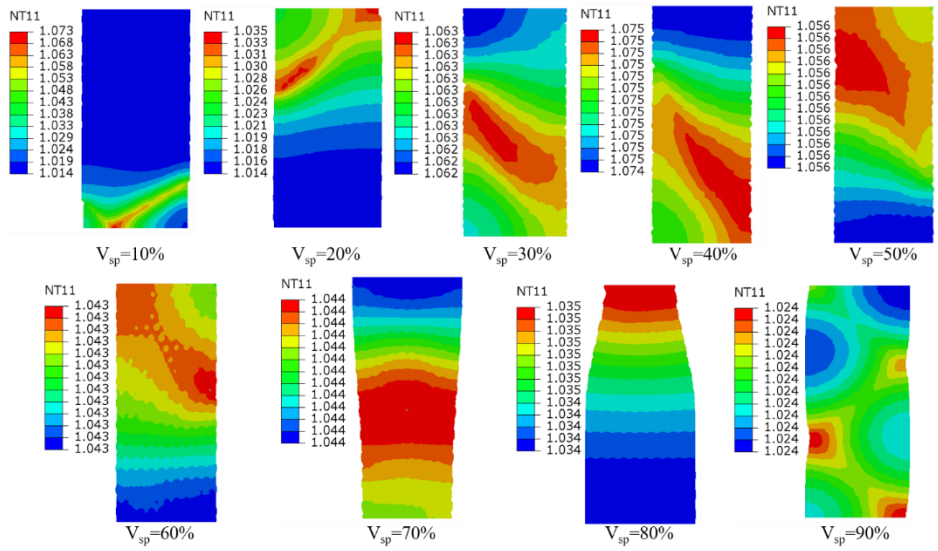

Figure 5.13 Contour plots of the temperature field in the honeycomb BMG-composite model of Figure 5.4 (d). The volume fraction of the Ni phase ranges from 10% to 90% as labeled. Note that these plots use different legend bounds. As the ductility is enhanced, the temperature “localization” becomes more “diffused”.

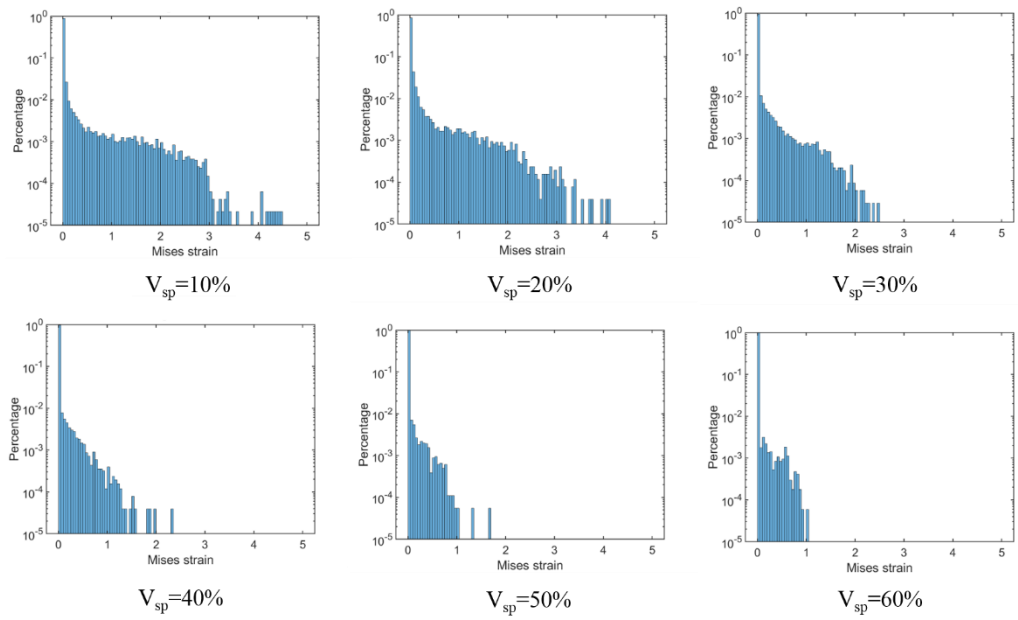

Figure 5.14 Corresponding to the simulation results in Figure 5.12, the probability distribution of Mises strain in the BMG phase is plotted when the macroscopic applied strain equals to 0.04. The probability at high Mises strain reduces significantly as the volume fraction increases. Comparing these results to Figure 5.11, it can be concluded that the honeycomb composite is more effectively in reducing shear band strains than the particulate composite. Again red-dotted curves provide a logarithmic fitting and thus gives the extent of the maximum shear-band strain.

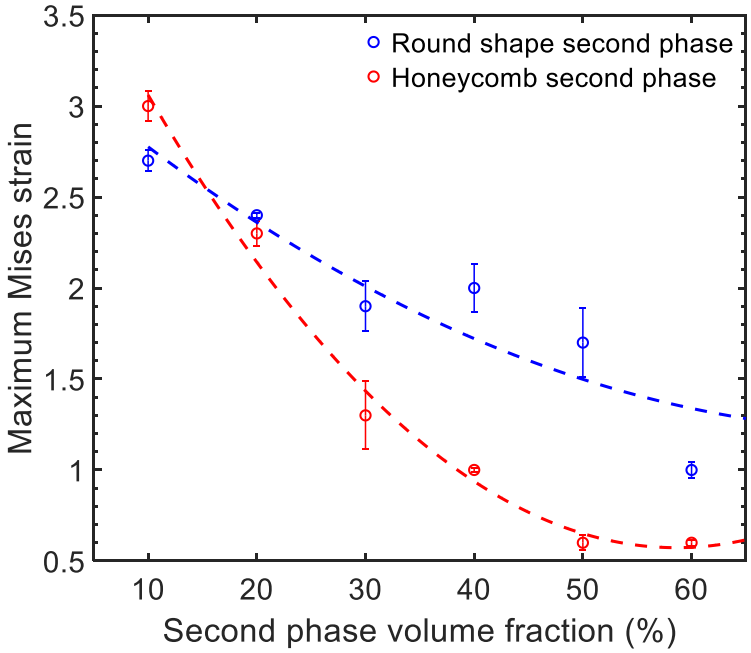

Figure 5.15 The maximum shear-band strain in the BMG phase as a function of the volume fraction of the second phase for the particulate and honeycomb composites when the macroscopic applied strain equals to 0.04. These datapoints are essentially the rightmost limits in Figure 5.11 and Figure 5.14, as obtained from the red-dotted logarithmic fitting curves. Again it can be concluded that the honeycomb composite is more effectively in blocking the shear-band propagation.

(i.e., tails in Figure 5.11 and Figure 5.14) for these two types of BMGCs. The tails in Figure 5.11 and Figure 5.14 can be fitted to a logarithmic decay, which resembles the weakest-link-type failure analysis in brittle solids. The maximum shear-band strain is obtained from the dashed fitting curves. Trends in Figure 5.15 are in good agreement with the comparison of the two trends in Eqs. (5.12) and (5.14).

5.4 Conclusions

A free-volume-based thermomechanical model has been implemented into a nonlinear finite element framework through a user-defined material subroutine in ABAQUS. Numerical simulations have been conducted to investigate the role of microstructure and property mismatches on the effectiveness of the second phase in resisting the strain localization in the BMG shear bands. Main observations and conclusions are as follows:

1) Shear-band initiation locations and their propagation directions in BMGCs under uniaxial tension are significant influenced by the stiffness of the second phase particles. With a low second-phase stiffness, the shear band would like to emanant from the interface and then has to be blocked by other second phases lying in 45º directions from the center one. For BMGCs with an extremely high second-phase stiffness, the initiated shear bands are tangent to the interface.
2) The resistance to the impinging shear band relies on both the second phase stiffness and some geometric parameters such as the particle size and the cell wall thickness. For our 2D cases, closed-form estimates are derived to correlate the dependence of the maximum shear-band strain to the volume fraction.
3) Through numerical simulations on two types of BMGCs, it can be concluded that along with the increase of the second-phase volume fraction, the BMG strain field will localize in more bands during tension, and at the same time temperature bands become thicker and finally turn into almost uniform distribution. Also, under the same volume fraction, the honeycomb BMGC is much more efficient in promoting the ductility than the particle BMGC.

4) Numerical simulations and approximate relationships in Eqs. (5.12) and (5.14) show the same trends in Figure 5.15, which also agrees with our recent BMGC made from a Ni foam (in which percolation limit is clearly reached despite the low volume fraction of about 11%). Consequently, the percolation analysis in Figure 5.1, the shear-band resistance study in Figure 5.15, and foam-based BMGCs in Figure 5.2 should synergistically be investigated so as to determine the ductility enhancement.

6 Conclusions and perspectives

As concluding remarks, the main objective of this dissertation work is to understand the mechanics of friction stir welding by using both computational and analytical methods. To achieve this goal, a series of thermo-mechanical finite element models and analytical models have been developed to investigate the tool-workpiece stick-slip conditions and workpiece-workpiece bonding formation. The summary is as follows:

(1) Tool-workpiece stick-slip conditions are investigated through both numerical simulation and analytical interpretation. We have employed the Coupled Eulerian-Lagrangian (CEL) method to simulate the FSW process and predict the interfacial stick-slip ratio, torque and heat generation rate, comparison is made between CEL simulation results and outcomes obtain through CFD methodologies with different frictional boundary conditions. Based on the Hill-Bower similarity relationship in the contact analysis, an analytical model is developed to prove why a constant stick-slip fraction will be developed in the steady state, to correlate the stick-slip fraction to processing parameters such as the tool spin rate, and further to derive dimensionless functions for torque and heat-generation-rate predictions. Pros and cons of various numerical approaches in predicting stick-slip are discussed, and our analytical model has been found to agree well with our numerical simulation and literature experimental results. These analyses provide the critical strain-rate and temperature fields that are needed for the bonding analysis.

(2) A critical assessment of various solid-state-bonding mechanisms is established for friction stir welding (FSW) processes of engineering alloys. For the wide spectrum of material constitutive laws and FSW processing conditions examined and employed in realistic applications, the thermomechanical history on the workpiece-workpiece interface traverses in the creep-dominated regime for the growth/shrinkage of interfacial cavities. The evolution of the bonding fraction relies mainly on the creep strain rate in the adjourning workpieces, weakly on stress triaxiality, and negligibly on interfacial diffusion.

(3) Based on the solid-state bonding mechanism in friction stir welding that has been investigated, we derive a general modeling framework of bonding fraction evolution, which directly depends on the stress, strain rate, and temperature fields near the interface. The full field information computed by finite element simulations is used as inputs to assess the evolution and extent of bonding fraction at the workpiece-workpiece interface. Based on the stick-slip contact analysis, an approximate but analytical solution has been developed to derive the bonding fraction field from the given processing, geometric, and material constitutive parameters, and the predicted ultimate bonding extent with respect to these parameters becomes a figure of merit for the study of processing window for industrial applications and design of the FSW process.

Apart from investigations on friction stir welding, ductility enhancement in metallic glass composites has also been studied in the thesis. A thermo-mechanical finite element method based on the free volume model and plasticity-induced heating is proposed to investigate the inhomogeneous deformation behaviors of bulk metallic glass. We demonstrate that an enhanced ductility can be realized in a BMGC made from crystalline Ni foam (completely percolated even with a volume fraction of about 11%), suggesting the resistance in the second phase to the impinging shear-force dipole from neighboring shear bands be the dominant factor for such a ductility improvement. The shortcomings of percolation approach, as well as the synergistic effects of microstructure and mismatches in mechanical properties, are investigated. The effectiveness of ductility improvement is demonstrated by calculating the probability distributions of the shear-band effective strain.

This dissertation presents a couple of original works on mechanics of the friction stir welding investigation, although many insightful results are obtained, these works can be further extended along following lines:

(1) Experimental validation of bonding map. As mentioned above, predictions on bonding condition at workpiece-workpiece interface with respect to vary operation parameters was established and process window could be found for the design and improvement of solid-state welding technique. Corresponding experiments should be conducted to validate the bonding map under different operation parameters.

(2) Workpiece-workpiece interface interaction investigation for dissimilar materials. Friction stir welding are widely used to joint dissimilar materials, such as steel and aluminum, current procedure for solid-state-bonding mechanism determination could be extended to study the bonding formation mechanism for dissimilar materials.

(3) Predictive modeling of ductile fracture in metal joining parts. Physical and mechanical drawbacks such as voids, flaws and residual stresses that are introduced during joining procedures are key factors that will finally lead to structural failure in practical application, a microstructure based finite element simulation that utilize the CPFEM and the constitutive model which could describe the behavior of progressively cavitating solids will be applied to investigate the ductile fracture resistance of weld part.

List of references

[1] H.B. Cary, S.C. Helzer, Modern welding technology, (1979).

[2] R.S. Mishra, Z. Ma, Friction stir welding and processing, Materials science and engineering: R: reports 50(1-2) (2005) 1-78.

[3] R. Nandan, T. DebRoy, H. Bhadeshia, Recent advances in friction-stir welding–process, weldment structure and properties, Progress in materials science 53(6) (2008) 980-1023.

[4] D.M. Neto, P. Neto, Numerical modeling of friction stir welding process: a literature review, The International Journal of Advanced Manufacturing Technology 65(1-4) (2013) 115-126.

[5] Z. Yu, H. Choo, Z. Feng, S.C. Vogel, Influence of thermo-mechanical parameters on texture and tensile behavior of friction stir processed Mg alloy, Scripta Materialia 63(11) (2010) 1112-1115.

[6] N. Switzner, Z. Yu, M. Eff, T. Lienert, A. Fonseca, Microstructure and mechanical property variations within inertia friction-welded joints of stainless steel to steel, The International Journal of Advanced Manufacturing Technology 95(9-12) (2018) 4327-4340.

[7] W. Cai, G. Daehn, A. Vivek, J. Li, H. Khan, R.S. Mishra, M. Komarasamy, A state-of-the-art review on solid-state metal joining, Journal of Manufacturing Science and Engineering 141(3) (2019).

[8] X. Wang, Y. Gao, M. McDonnell, Z. Feng, On the solid-state-bonding mechanism in friction stir welding, Extreme Mechanics Letters (2020) 100727.

[9] R. Nandan, G. Roy, T. Lienert, T. DebRoy, Numerical modelling of 3D plastic flow and heat transfer during friction stir welding of stainless steel, Science and Technology of Welding and Joining 11(5) (2006) 526-537.

[10] A. Arora, R. Nandan, A.P. Reynolds, T. DebRoy, Torque, power requirement and stir zone geometry in friction stir welding through modeling and experiments, Scripta Materialia 60(1) (2009) 13-16.

[11] P. Colegrove, H. Shercliff, Experimental and numerical analysis of aluminium alloy 7075-T7351 friction stir welds, Science and Technology of Welding and Joining 8(5) (2003) 360-368.

[12] P. Colegrove, H. Shercliff, Two-dimensional CFD modelling of flow round profiled FSW tooling, Science and technology of welding and joining 9(6) (2004) 483-492.

[13] P.A. Colegrove, H.R. Shercliff, 3-Dimensional CFD modelling of flow round a threaded friction stir welding tool profile, Journal of materials processing technology 169(2) (2005) 320-327.

[14] X. Liu, G. Chen, J. Ni, Z. Feng, Computational fluid dynamics modeling on steady-state friction stir welding of aluminum alloy 6061 to TRIP steel, Journal of Manufacturing Science and Engineering 139(5) (2017) 051004.

[15] T. Seidel, A.P. Reynolds, Two-dimensional friction stir welding process model based on fluid mechanics, Science and technology of welding and joining 8(3) (2003) 175-183.

[16] P. Ulysse, Three-dimensional modeling of the friction stir-welding process, International Journal of Machine Tools and Manufacture 42(14) (2002) 1549-1557.

[17] H. Schmidt, J. Hattel, A local model for the thermomechanical conditions in friction stir welding, Modelling and simulation in materials science and engineering 13(1) (2004) 77.

[18] Z. Zhang, H. Zhang, Numerical studies on effect of axial pressure in friction stir welding, Science and Technology of Welding and Joining 12(3) (2007) 226-248.

[19] X. Zhu, Y. Chao, Numerical simulation of transient temperature and residual stresses in friction stir welding of 304L stainless steel, Journal of materials processing technology 146(2) (2004) 263-272.

[20] H.N.B. Schmidt, J. Hattel, Heat source models in simulation of heat flow in friction stir welding, International Journal of Offshore and Polar Engineering 14(04) (2004).

[21] H. Schmidt, J. Hattel, J. Wert, An analytical model for the heat generation in friction stir welding, Modelling and simulation in materials science and engineering 12(1) (2003) 143.

[22] Z. Yu, W. Zhang, H. Choo, Z. Feng, Transient heat and material flow modeling of friction stir processing of magnesium alloy using threaded tool, Metallurgical and Materials Transactions A 43(2) (2012) 724-737.

[23] F. William, J.W.L. Horigan, Process for diffusion-bonding, Google Patents, 1965.

[24] S. Dunkerton, Diffusion Bonding—An Overview, Diffusion Bonding 2, Springer1991, pp. 1-12.

[25] B. Kang, W. Cai, C.-A. Tan, Dynamic response of battery tabs under ultrasonic welding, Journal of Manufacturing Science and Engineering 135(5) (2013).

[26] K. Martinsen, S. Hu, B. Carlson, Joining of dissimilar materials, Cirp Annals 64(2) (2015) 679-699.

[27] T.Z. Blazynski, Explosive welding, forming and compaction, Springer Science & Business Media2012.

[28] A. Loureiro, R. Mendes, J. Ribeiro, R. Leal, I. Galvão, Effect of explosive mixture on quality of explosive welds of copper to aluminium, Materials & Design 95 (2016) 256-267.

[29] Y. Lu, J.Y. Huang, C. Wang, S. Sun, J. Lou, Cold welding of ultrathin gold nanowires, Nature nanotechnology 5(3) (2010) 218-224.

[30] W.t. King, W. Owczarski, Diffusion welding of commercially pure titanium, WELD J 46(7) (1967) 289.

[31] C. Hamilton, Pressure requirements for diffusion bonding titanium, Titanium science and technology, Springer1973, pp. 625-648.

[32] G. Chen, Z. Feng, J. Chen, L. Liu, H. Li, Q. Liu, S. Zhang, X. Cao, G. Zhang, Q. Shi, Analytical approach for describing the collapse of surface asperities under compressive stress during rapid solid state bonding, Scripta Materialia 128 (2017) 41-44.

[33] Y.-F. Gao, A. Bower, Elastic–plastic contact of a rough surface with Weierstrass profile, Proceedings of the Royal Society A: Mathematical, Physical and Engineering Sciences 462(2065) (2006) 319-348.

[34] S. Babu, M. Santella, Z. Feng, B. Riemer, J. Cohron, Empirical model of effects of pressure and temperature on electrical contact resistance of metals, Science and technology of welding and joining 6(3) (2001) 126-132.

[35] B. Derby, E. Wallach, Theoretical model for diffusion bonding, Metal Science 16(1) (1982) 49-56.

[36] B. Derby, E. Wallach, Diffusion bonding: development of theoretical model, Metal Science 18(9) (1984) 427-431.

[37] A. Hill, E. Wallach, Modelling solid-state diffusion bonding, Acta Metallurgica 37(9) (1989) 2425-2437.

[38] B. Liechty, B. Webb, Modeling the frictional boundary condition in friction stir welding, International Journal of Machine Tools and Manufacture 48(12-13) (2008) 1474-1485.

[39] X. Liu, G. Chen, J. Ni, Z. Feng, Computational fluid dynamics modeling on steady-state friction stir welding of aluminum alloy 6061 to TRIP steel, Journal of Manufacturing Science and Engineering 139(5) (2017).

[40] G. Chen, Z. Feng, Y. Zhu, Q. Shi, An alternative frictional boundary condition for computational fluid dynamics simulation of friction stir welding, Journal of Materials Engineering and Performance 25(9) (2016) 4016-4023.

[41] S. Xu, X. Deng, Two and three-dimensional finite element models for the friction stir welding process, 4th Int. Symp. On Friction Stir Welding, TWI Ltd., Park City, Utah, USA, 2003.

[42] S.-w. Xu, X. Deng, A.P. Reynolds, T. Seidel, Finite element simulation of material flow in friction stir welding, Science and Technology of Welding and Joining 6(3) (2001) 191-193.

[43] F. Ducobu, E. Riviere-Lorphevre, E. Filippi, Application of the Coupled Eulerian-Lagrangian (CEL) method to the modeling of orthogonal cutting, European Journal of Mechanics-A/Solids 59 (2016) 58-66.

[44] F. Al-Badour, N. Merah, A. Shuaib, A. Bazoune, Coupled Eulerian Lagrangian finite element modeling of friction stir welding processes, Journal of Materials Processing Technology 213(8) (2013) 1433-1439.

[45] K. Chen, X. Liu, J. Ni, Thermal-mechanical modeling on friction stir spot welding of dissimilar materials based on Coupled Eulerian-Lagrangian approach, The International Journal of Advanced Manufacturing Technology 91(5-8) (2017) 1697-1707.

[46] H. Atharifar, D. Lin, R. Kovacevic, Numerical and experimental investigations on the loads carried by the tool during friction stir welding, Journal of Materials Engineering and Performance 18(4) (2009) 339-350.
[47] R. Nandan, G. Roy, T. Lienert, T. Debroy, Three-dimensional heat and material flow during friction stir welding of mild steel, Acta materialia 55(3) (2007) 883-895.
[48] T. Sheppard, D. Wright, Determination of flow stress: Part 1 constitutive equation for aluminium alloys at elevated temperatures, Metals Technology 6(1) (1979) 215-223.
[49] K.E. Tello, A.P. Gerlich, P.F. Mendez, Constants for hot deformation constitutive models for recent experimental data, Science and technology of Welding and joining 15(3) (2010) 260-266.
[50] N. Mostaghel, T. Davis, Representations of Coulomb friction for dynamic analysis, Earthquake engineering & structural dynamics 26(5) (1997) 541-548.
[51] M. Dirikolu, T. Childs, K. Maekawa, Finite element simulation of chip flow in metal machining, International Journal of Mechanical Sciences 43(11) (2001) 2699-2713.
[52] G.R. Johnson, W.H. Cook, A constitutive model and data for metals subjected to large strains, high strain rates and high temperatures, Proceedings of the 7th International Symposium on Ballistics, The Netherlands, 1983, pp. 541-547.
[53] K.C. Mills, Recommended values of thermophysical properties for selected commercial alloys, Woodhead Publishing2002.
[54] V. Soundararajan, S. Zekovic, R. Kovacevic, Thermo-mechanical model with adaptive boundary conditions for friction stir welding of Al 6061, International Journal of Machine Tools and Manufacture 45(14) (2005) 1577-1587.
[55] G. Chen, Q. Ma, S. Zhang, J. Wu, G. Zhang, Q. Shi, Computational fluid dynamics simulation of friction stir welding: A comparative study on different frictional boundary conditions, Journal of Materials Science & Technology 34(1) (2018) 128-134.
[56] Y.J. Chao, S. Liu, C.H. Chien, Friction stir welding of al 6061-T6 thick plates: Part II-numerical modeling of the thermal and heat transfer phenomena, Journal of the Chinese Institute of Engineers 31(5) (2008) 769-779.
[57] R. Hill, Similarity analysis of creep indentation tests, Proceedings of the Royal Society of London. Series A: Mathematical and Physical Sciences 436(1898) (1992) 617-630.

[58] A. Bower, N.A. Fleck, A. Needleman, N. Ogbonna, Indentation of a power law creeping solid, Proceedings of the Royal Society of London. Series A: Mathematical and Physical Sciences 441(1911) (1993) 97-124.

[59] J.H. Lee, Y. Gao, A.F. Bower, H. Xu, G.M. Pharr, Stiffness of frictional contact of dissimilar elastic solids, Journal of the Mechanics and Physics of Solids 112 (2018) 318-333.

[60] K.L. Johnson, K.L. Johnson, Contact mechanics, Cambridge university press1987.

[61] K. Johnson, Adhesion and friction between a smooth elastic spherical asperity and a plane surface, Proceedings of the Royal Society of London. Series A: Mathematical, Physical and Engineering Sciences 453(1956) (1997) 163-179.

[62] Y. Gao, B.N. Lucas, J.C. Hay, W.C. Oliver, G.M. Pharr, Nanoscale incipient asperity sliding and interface micro-slip assessed by the measurement of tangential contact stiffness, Scripta materialia 55(7) (2006) 653-656.

[63] M. Peel, A. Steuwer, P. Withers, T. Dickerson, Q. Shi, H. Shercliff, Dissimilar friction stir welds in AA5083-AA6082. Part I: process parameter effects on thermal history and weld properties, Metallurgical and Materials Transactions A 37(7) (2006) 2183-2193.

[64] Y.S. Sato, M. Urata, H. Kokawa, Parameters controlling microstructure and hardness during friction-stir welding of precipitation-hardenable aluminum alloy 6063, Metallurgical and Materials Transactions A 33(3) (2002) 625-635.

[65] G. Roy, R. Nandan, T. DebRoy, Dimensionless correlation to estimate peak temperature during friction stir welding, Science and Technology of welding and Joining 11(5) (2006) 606-608.

[66] K.L. Nielsen, T. Pardoen, V. Tvergaard, B. de Meester, A. Simar, Modelling of plastic flow localisation and damage development in friction stir welded 6005A aluminium alloy using physics based strain hardening law, International Journal of Solids and Structures 47(18-19) (2010) 2359-2370.

[67] M. Reza-E-Rabby, K. Ross, N.R. Overman, M.J. Olszta, M. McDonnell, S.A. Whalen, Joining thick section aluminum to steel with suppressed FeAl intermetallic formation via friction stir dovetailing, Scripta Materialia 148 (2018) 63-67.

[68] J. Pilling, The kinetics of isostatic diffusion bonding in superplastic materials, Materials Science and Engineering 100 (1988) 137-144.
[69] M. Plata, J. Piwnik, Theoretical and experimental analysis of seam weld formation in hot extrusion of aluminum alloys, Proceedings of International Aluminum Extrusion Technology Seminar, 2000, pp. 205-212.
[70] M. Ashby, Mechanisms of deformation and fracture, Advances in applied mechanics, Elsevier1983, pp. 117-177.
[71] W. Zhang, X. Wang, Y. Wang, X. Yu, Y. Gao, Z. Feng, Type IV failure in weldment of creep resistant ferritic alloys: II. Creep fracture and lifetime prediction, Journal of the Mechanics and Physics of Solids 134 (2020) 103775.
[72] D. Hull, D. Rimmer, The growth of grain-boundary voids under stress, Philosophical Magazine 4(42) (1959) 673-687.
[73] A. Needleman, J. Rice, Plastic creep flow effects in the diffusive cavitation of grain boundaries, Perspectives in creep fracture, Elsevier1983, pp. 107-124.
[74] T.-L. Sham, A. Needleman, Effects of triaxial stressing on creep cavitation of grain boundaries, Acta Metallurgica 31(6) (1983) 919-926.
[75] A. Cocks, M. Ashby, On creep fracture by void growth, Progress in materials science 27(3-4) (1982) 189-244.
[76] V. Tvergaard, Material failure by void growth to coalescence, Advances in applied Mechanics, Elsevier1989, pp. 83-151.
[77] W. Zhang, Y. Gao, Z. Feng, X. Wang, S. Zhang, L. Huang, Z. Huang, L. Jiang, Ductility Limit Diagrams for Superplasticity and Forging of High Temperature Polycrystalline Materials, Acta Materialia (2020).
[78] W. Zhang, X. Wang, Y. Wang, X. Yu, Y. Gao, Z. Feng, Type IV failure in weldment of creep resistant ferritic alloys: I. Micromechanical origin of creep strain localization in the heat affected zone, Journal of the Mechanics and Physics of Solids 134 (2020) 103774.
[79] V. Balasubramanian, Relationship between base metal properties and friction stir welding process parameters, Materials Science and Engineering: A 480(1-2) (2008) 397-403.

[80] A. Esmaeili, H.Z. Rajani, M. Sharbati, M.B. Givi, M. Shamanian, The role of rotation speed on intermetallic compounds formation and mechanical behavior of friction stir welded brass/aluminum 1050 couple, Intermetallics 19(11) (2011) 1711-1719.

[81] N.R.J. Hynes, P.S. Velu, Effect of rotational speed on Ti-6Al-4V-AA 6061 friction welded joints, Journal of manufacturing processes 32 (2018) 288-297.

[82] Z. Shen, Y. Chen, M. Haghshenas, A. Gerlich, Role of welding parameters on interfacial bonding in dissimilar steel/aluminum friction stir welds, Engineering Science and Technology, an International Journal 18(2) (2015) 270-277.

[83] M. Boz, A. Kurt, The influence of stirrer geometry on bonding and mechanical properties in friction stir welding process, Materials & Design 25(4) (2004) 343-347.

[84] Y.-h. Zhao, S.-b. Lin, L. Wu, F.-x. Qu, The influence of pin geometry on bonding and mechanical properties in friction stir weld 2014 Al alloy, Materials letters 59(23) (2005) 2948-2952.

[85] T.-J. Chuang, J.R. Rice, The shape of intergranular creep cracks gro′ ing by surface diffusion, Acta Metallurgica 21(12) (1973) 1625-1628.

[86] T.-J. Chuang, K.I. Kagawa, J.R. Rice, L.B. Sills, Overview no. 2: Non-equilibrium models for diffusive cavitation of grain interfaces, Acta Metallurgica 27(3) (1979) 265-284.

[87] H.J. Frost, M.F. Ashby, Deformation mechanism maps: the plasticity and creep of metals and ceramics, Pergamon press1982.

[88] R. Crawford, G. Cook, A. Strauss, D. Hartman, M. Stremler, Experimental defect analysis and force prediction simulation of high weld pitch friction stir welding, Science and Technology of Welding and Joining 11(6) (2006) 657-665.

[89] T. Sheppard, A. Jackson, Constitutive equations for use in prediction of flow stress during extrusion of aluminium alloys, Materials science and technology 13(3) (1997) 203-209.

[90] D. Rosenthal, Mathematical theory of heat distribution during welding and cutting, Welding journal 20 (1941) 220-234.

[91] F. Spaepen, A microscopic mechanism for steady state inhomogeneous flow in metallic glasses, Acta metallurgica 25(4) (1977) 407-415.

[92] H. Jia, L. Zheng, W. Li, N. Li, J. Qiao, G. Wang, Y. Ren, P.K. Liaw, Y. Gao, Insights from the lattice-strain evolution on deformation mechanisms in metallic-glass-matrix composites, Metallurgical and Materials Transactions A 46(6) (2015) 2431-2442.

[93] D.C. Hofmann, J.-Y. Suh, A. Wiest, G. Duan, M.-L. Lind, M.D. Demetriou, W.L. Johnson, Designing metallic glass matrix composites with high toughness and tensile ductility, Nature 451(7182) (2008) 1085-1089.

[94] A. Donohue, F. Spaepen, R. Hoagland, A. Misra, Suppression of the shear band instability during plastic flow of nanometer-scale confined metallic glasses, Applied Physics Letters 91(24) (2007) 241905.

[95] D.C. Hofmann, J.-Y. Suh, A. Wiest, M.-L. Lind, M.D. Demetriou, W.L. Johnson, Development of tough, low-density titanium-based bulk metallic glass matrix composites with tensile ductility, Proceedings of the National Academy of Sciences 105(51) (2008) 20136-20140.

[96] Z. Zhu, H. Zhang, Z. Hu, W. Zhang, A. Inoue, Ta-particulate reinforced Zr-based bulk metallic glass matrix composite with tensile plasticity, Scripta Materialia 62(5) (2010) 278-281.

[97] M. Lee, Y. Li, C. Schuh, Effect of a controlled volume fraction of dendritic phases on tensile and compressive ductility in La-based metallic glass matrix composites, Acta Materialia 52(14) (2004) 4121-4131.

[98] H. Zhou, S. Qu, W. Yang, An atomistic investigation of structural evolution in metallic glass matrix composites, International Journal of Plasticity 44 (2013) 147-160.

[99] W. Rao, J. Zhang, G. Kang, P.K. Liaw, Numerical simulation on the deformation behaviors of bulk metallic glass composites under uniaxial tension and compression, Composite Structures 187 (2018) 411-428.

[100] Z. Liu, G. Liu, R. Qu, Z. Zhang, S. Wu, T. Zhang, Microstructural percolation assisted breakthrough of trade-off between strength and ductility in CuZr-based metallic glass composites, Scientific reports 4 (2014) 4167.

[101] Z. Liu, R. Li, G. Liu, W. Su, H. Wang, Y. Li, M. Shi, X. Luo, G. Wu, T. Zhang, Microstructural tailoring and improvement of mechanical properties in CuZr-based bulk metallic glass composites, Acta Materialia 60(6-7) (2012) 3128-3139.

[102] S. Pauly, G. Liu, G. Wang, U. Kühn, N. Mattern, J. Eckert, Microstructural heterogeneities governing the deformation of Cu47. 5Zr47. 5Al5 bulk metallic glass composites, Acta Materialia 57(18) (2009) 5445-5453.

[103] Y. Gao, An implicit finite element method for simulating inhomogeneous deformation and shear bands of amorphous alloys based on the free-volume model, Modelling and Simulation in Materials Science and Engineering 14(8) (2006) 1329.

[104] M.H. Sadd, Elasticity: theory, applications, and numerics, Academic Press2009.

[105] H. Xu, G. Pharr, An improved relation for the effective elastic compliance of a film/substrate system during indentation by a flat cylindrical punch, Scripta Materialia 55(4) (2006) 315-318.

Vita

Xue Wang was born in Huludao, Liaoning, China, on March 29, 1989. She received a Bachelor of Science degree from Engineering Mechanics Department at Dalian University of Technology (China) in 2011. From 2011 to 2014, she enrolled in the master program at the Department of Engineering Mechanics at Dalian University of Technology advised by Dr. Xicheng Wang and Dr. Changyu Shen, and earned her Master of Science degree in 2014. In August 2016, she joined Dr. Yanfei Gao's group in the Department of Materials Science and Engineering at the University of Tennessee, Knoxville.